A New Synthesis Route to $Pb(Mg_{1/3}Nb_{2/3})O_3$-Based Materials by the Controlled Agglomeration of Reagent Particles

Gregor Trefalt

Doctoral Dissertation
Jožef Stefan Interantional Postgraduate School
Ljubljana, Slovenia, March, 2012

Evaluation Board:

Prof. Dr. Barbara Malič, Jožef Stefan Institute, Ljubljana, Slovenia
Dr. Paul Bowen, Ecole Polytechnique Fédérale de Lausanne, Lausanne, Switzerland
Prof. Dr. Christos N. Likos, University of Vienna, Wien, Austria

MEDNARODNA PODIPLOMSKA ŠOLA JOŽEFA STEFANA
JOŽEF STEFAN INTERNATIONAL POSTGRADUATE SCHOOL

Gregor Trefalt

A New Synthesis Route to $Pb(Mg_{1/3}Nb_{2/3})O_3$-Based Materials by the Controlled Agglomeration of Reagent Particles

Doctoral Dissertation

Nova sintezna pot za pripravo materialov na osnovi $Pb(Mg_{1/3}Nb_{2/3})O_3$ s kontrolirano aglomeracijo delcev reagentov

Doktorska Disertacija

Supervisor: Prof. Dr. Marija Kosec

Co-supervisor: Prof. Dr. Bosiljka Tadić

Ljubljana, Slovenia, March 2012

Index

Abstract

In this thesis we demonstrate a new, simple, and efficient method for the solid-state synthesis of oxides with a complex chemical composition. We modify the traditional solid-state synthesis method, which is used in the majority of ceramics laboratories around the world, in order to prepare multi-metallic oxide powders from classic ferroelectrics to very popular multiferroic and other materials. Firm principles are established in the field of solid-state chemistry, *i.e.*, the particles of the starting compounds should be small and should be homogeneously distributed in the reactant mixture[1]. This is very true for the simple binary systems; however it is not necessarily true for more complex systems involving several starting compounds, which may show complex reaction pathways during heating. It can happen that some undesirable intermediate products form at lower temperatures, which at the end react to form the final product, however, the phase purity of such products and their chemical homogeneity is questionable. Therefore, in many cases a simple, solid-state synthesis does not give the desired results.

The problem described above is encountered in the synthesis of $Pb(Mg_{1/3}Nb_{2/3})O_3$ (PMN) based materials. In the mixture of PbO, Nb_2O_5, and MgO, the first two species preferentially react to form Pb-Nb pyrochlore phases, which are stable and hard to eliminate from the final product. The presence of these phases deteriorates the properties of the ceramics. First we have to address the question how to avoid or slow down the parasitic reactions and how to force the correct ones. In a solid-state synthesis there are not many options to tailor the chemical reactivity. Our idea is to simply avoid or limit the contacts between the reactant particles that lead to non-desirable products, *i.e.*, the PbO-Nb_2O_5 contacts. Our next challenge is to create the desired contacts in the reagent powder mixture. The solution to this problem is the formation of colloidal agglomerates of reagent particles with the desired structure.

First, we measure the electrokinetic properties of our starting components, *i.e.*, PbO, Nb_2O_5 and $(MgCO_3)_4{\cdot}Mg(OH)_2{\cdot}4H_2O$, (MHC). Using these data as the input parameters we employ Monte Carlo simulations to predict the formation of agglomerates in the suspensions of reagent particles in different pH conditions. Our simulations reveal a large population of clusters with close contacts between the PbO and Nb_2O_5 at pH = 11.4, which thus enable the pyroclore phase to form. Whereas, at pH = 12.5 the competition between the repulsive and the attractive interactions changes in favor of the assembly of the equilibrium clusters in which MHC particles effectively separate PbO and Nb_2O_5. We also explore how the varying size of MHC particles affects the

[1] With this the number of contacts between the particles of reactants is increased.

cluster assembly in both relevant pH conditions. A detailed analysis of the contacts between the particles in the system as a function of different conditions is presented.

Next we use the results from simulations to conduct the experiments. The aqueous suspensions of reagent particles are prepared at pH = 10.0, pH = 11.4, pH = 12.5, and in acetone. The suspensions are dried and heated at elevated temperatures. After heating at 900 °C a pure PMN perovskite phase is obtained only from the sample with the pH = 12.5. All the other samples contain, in addition to the perovskite, the detrimental pyrochlore phase. The results are in agreement with the structure of the agglomerates predicted by simulations. The properties of the ceramics prepared from the sample with pH = 12.5 are superior to those of the other samples. Furthermore, dense ceramics are obtained by sintering as low as 950 °C with the dielectric properties being comparable to the values obtained for ceramics sintered at about 200 K higher temperatures.

Finally, we adopt the same approach for the synthesis of the $0.65Pb(Mg_{1/3}Nb_{2/3})O_3$–$0.35PbTiO_3$. Here, one additional component, TiO_2, is added to the reactant mixture. The aqueous suspensions of the reactant particles are prepared at pH = 11.4 and pH = 12.5. The two powders are calcined at 850 °C, where only the pH12.5 powder yields a phase-pure perovskite. Similar to the PMN case, the pH11.4 powder is composed of a mixture of perovskite and pyrochlore. After sintering at 950 °C the density of the pH12.5 ceramic is equal to 96 %, while the pH11.4 sample reaches only 81 % of theoretical density. The pH12.5 ceramic exhibits electrical properties comparable to the ceramics prepared by the columbite method. On the other hand, the electrical properties of the pH11.4 ceramic are heavily deteriorated due to the presence of the pyrochlore phase and a high degree of porosity.

Povzetek

V pričujoči doktorski disertaciji poskušamo predstaviti novo, enostavno in učinkovito izpeljanko sinteze v trdnem stanju za pripravo oksidnih spojin s kompleksno kemijsko sestavo. Sintezo v trdnem stanju uporablja večina keramičnih laboratorijev v svetu za pripravo kompleksnih oksidnih spojin od klasičnih feroelektrčnih do multiferoičnih in ostalih materialov. Njeni principi so splošno znani: delci vhodnih spojin morajo biti majhni in kar se da homogeno pomešani med sabo, tako zagotovimo čim večje število kontaktov med delci, kjer se reakcija v trdnem ponavadi začne. V dvokomponentnem sistemu ti principi dobro veljajo, pri sistemih z več komponentami, kjer so reakcijski mehanizmi kompleksnejši, pa lahko ti odpovedo. Pri takšnih sistemih lahko nastanejo stabilni vmesni produkti, ki sicer pri povišanih temperaturah reagirajo do končnega produkta, vendar je fazna sestava in homogenost tako pripravljenih spojin vprašljiva. Klasična sinteza v trdnem stanju ne daje vedno zadovoljivih rezultatov.

S problemom, ki smo ga opisali zgoraj, se srečamo pri sintezi spojin na osnovi $Pb(Mg_{1/3}Nb_{2/3})O_3$ (PMN). V mešanici vhodnih prahov, PbO, Nb_2O_5 in MgO, prvi dve spojini pri nižji temperaturah reagirata do Pb-Nb piroklornih faz. Te faze so stabilne in tudi po končani reakciji ostajajo v končni mešanici in zmanjšujejo kakovost materiala. Na tem mestu se lahko vprašamo, kako preprečiti oziroma vsaj upočasniti neželene reakcije pri pripravi materialov na osnovi PMN. Pri sintezah v trdnem stanju je kemijsko reaktivnost težko kontrolirati. Naša ideja za rešitev tega problema je, da poskušamo zmanjšati število kontaktov med delci PbO in Nb_2O_5 ter tako omejiti reakcijo med tema dvema komponentama. To bi bilo možno doseči s kontrolirano tvorbo aglomeratov v suspenziji delcev reagentov.

Izmerili smo elektrokinetične lastnosti vhodnih prahov: PbO, Nb_2O_5 in $(MgCO_3)_4{\cdot}Mg(OH)_2{\cdot}4H_2O$, (MHC), in jih uporabili za vhodne parametre pri numeričnih simulacijah tvorbe agregatov v suspenzijah delcev reagentov. Z uporabo metode Monte Carlo smo študirali mehanizme aglomeracije pri različnih pH vrednostih suspenzije. Rezultati so pokazali, da pri pH = 11,4 nastajajo aglomerati z velikim številom PbO-Nb_2O_5 kontaktov, ki pospešujejo neželeno reakcijo do piroklornih faz. Nasprotno pri pH = 12,5 takšnih aglomeratov nismo zaznali, ker pozitivno nabiti MHC delci uspešno preprečujejo kontakte med negativno nabitimi delci PbO in Nb_2O_5. Raziskovali smo tudi vpliv velikosti delcev na tvorbo agregatov in analizirali kontakte med delci pri različnih pogojih.

Rezultate simulacij smo uporabili kot izhodišče za naše eksperimentalno delo. Pripravili smo vodne suspenzije delcev reagentov pri pH = 10,0, pH = 11,4 in pH = 12,5, poleg

tega smo pripravili suspenzijo tudi v acetonu. Suspenzije smo po sušenju segrevali pri povišani temperaturi, kjer je potekla reakcija v trdnem stanju. Po segrevanju pri 900 °C dobimo čisto perovskitno PMN fazo zgolj v primeru pH = 12,5, pri vseh ostalih vzorcih je poleg perovskitne prisotna še neželena piroklorna faza. Ti rezultati se ujemajo s strukturo aglomeratov predvideno s simulacijami. Lastnosti keramike pripravljene iz vzorca s pH = 12,5 so mnogo boljše v primerjavi z ostalimi vzorci. Prav tako so lastnosti keramike pH12,5 sintrane pri zgolj 950 °C primerljive s keramiko pripravljeno po drugih postopkih sintrano pri približno 200 K višjih temperaturah.

V nadaljevanju smo z isto metodo pripravili $0.65Pb(Mg_{1/3}Nb_{2/3})O_3$–$0.35PbTiO_3$. V tem primeru imamo v suspenziji dodatno še eno koponento, TiO_2. Suspenzije smo pripravili pri pH = 11,4 in pH = 12,5 in sušene mešanice kalcinirali pri 850 °C. Podobno kot v primeru PMN, tudi tukaj dobimo čisto perovskitno fazo zgolj v primeru pH = 12,5, medtem ko je v primeru pH = 11,4 rezultat mešanica perovskitne in piroklorne faze. Po sintranju pri 950 °C doseže keramika pH12,5 96 % teoretične gostote, vzorec pH11,4 pa zgolj 81 %. Lastnosti keramike pH12,5 so primerljive z lastnostmi keramike pripravljene po drugih metodah. Vzorec pripravljen pri pH = 11.4 pa izkazuje mnogo slabše lastnosti, ki so posledica prisotnosti piroklorne faze in relativno velike poroznosti.

Abbreviations

Acronyms

AFM	atomic force microscope
BD	Brownian dynamics
DLVO	Derjaguin-Landau-Verwey-Overbeek theory
FE-SEM	field-emission scanning electron microscopy
IEP	isoelectric point
MC	Monte Carlo
MD	molecular dynamics
MHC	$(MgCO_3)_4{\cdot}Mg(OH)_2{\cdot}4H_2O$
MPB	morphotropic phase boundary
PDF	powder diffraction file
PMN	$Pb(Mg_{1/3}Nb_{2/3})O_3$
PMN-PT	$Pb(Mg_{1/3}Nb_{2/3})O_3$ – $PbTiO_3$
PSD	particle size distribution
PZC	point of zero charge
RDF	radial distribution function
RT	room temperature
SEM	scanning electron microscopy
SFA	surface force apparatus
TD	theoretical density
TEM	transmission electron microscopy
TGA	thermogravimetric analysis
vdW	van der Waals
VMD	Visual Molecular Dynamics
XRD	X-ray diffraction

Symbols

A	Hamaker constant
a	particle radius
C	capacitance
d_{33}	piezoelectric coefficient
$d_{mean,\,A}$	mean particle diameter calculated from the area PSD
E	energy
E	electric field
E_c	coercive field
e_0	elementary charge
$g(r)$	radial distribution function
I	ionic strength
k_B	Boltzmann constant
M_{33}	electrostriction coefficient
N	number of particles
N_A	Avogadro number
P	polarization
P_r	remanent polarization
r_{ij}	distance between particles i and j
T	temperature
T_c	Curie temperature
U	interaction potential energy
ε_0	dielectric permittivity of vacuum
ε_r	relative dielectric permittivity
κ	Debye-Hückel screening length
ρ	density
ϕ	volume fraction
ψ	electrical potential
$\tan\delta$	dielectric loss

1 Introduction

In the Introduction some basics as well as the current status of the topics relevant to this thesis are presented. We begin with a description of ceramic materials, their synthesis and properties. We continue with electronic ceramics and emphasize the $Pb(Mg_{1/3}Nb_{2/3})O_3$–based materials – their synthesis is the main topic of this work. In the last sections of this chapter we address the topics of colloidal suspensions and their numerical modeling, which are strongly connected with our new synthesis route.

1.1 Ceramics & Ceramics Processing

Solid materials can be divided into four classes, *i.e.*, ceramics, metals, polymers, and composites. The last of these are made with the combinations of the first three. The first class, *i.e.*, ceramics, is composed of inorganic, non-metallic materials, which are usually prepared at elevated temperatures, *e.g.*, above 1000 °C. Typical properties of this class of materials are high-temperature stability, high compressive strength, high abrasion and corrosion resistivity. Their main weakness is brittleness and, consequently, low resistance to thermal shocks. These are general properties of the ceramics; however, they can be modified and tuned to meet the needs of applications [1]. Due to the diverse properties that can be achieved, ceramics are used in a wide range of applications. By function we can divide these materials into several groups: electronic, magnetic, nuclear, optical, mechanical, thermal, chemical, biological, and aesthetic ceramics [2].

The structure of a solid can be crystalline, polycrystalline or amorphous. However, amorphous inorganic materials, *i.e.*, glasses, can be by definition regarded as ceramics, we consider here ceramic to be a polycrystalline material, composed of single-crystalline grains. In Figure 1 a ceramic sample observed with an electron microscope is presented. The ceramic is an ensemble of grains connected to each other by grain boundaries and, usually, pores are also present, as it is clear from the microstructure. The gains are typically in the size range between a few tens of nanometers and several hundred micrometers. In addition to the chemical composition and crystal structure, the microstructure has a huge influence on the properties of the ceramic sample. For example the fracture strength, electrical, magnetic, and optical properties are all largely dependent on the microstructure of the ceramics.

The first step of ceramic processing is the powder synthesis. Powder with a precisely controlled composition, morphology and particle size is needed for the preparation of high-quality ceramic materials. A variety of methods, *e.g.*, solid-state synthesis, sol-gel method, hydrothermal synthesis, mechanochemical synthesis, molten-salt synthesis,

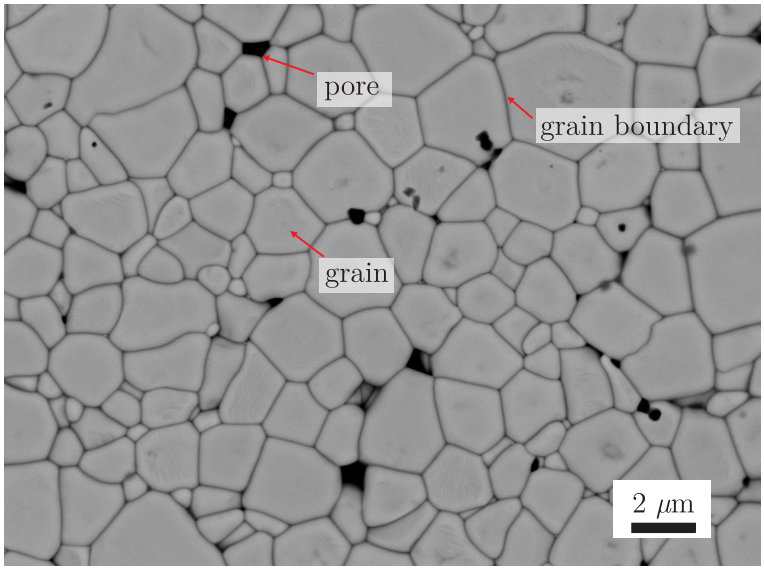

Figure 1: *Ceramic microstructure.* Ceramic is a polycrystalline material, composed of grains, pores, and grain boundaries.

spray-drying, and co-precipitation, are utilized for the ceramic powder preparation. Among these, a solid-state synthesis is the most widely used, especially in industry, due to its simplicity, low-cost, and environmental benefits. The next step is forming, where the powder is compacted to the desired shape. In the final step the ceramic sample is heated, the particles join together, the sample is densifying and the grains are growing. This step is called sintering.

1.1.1 Solid–State Synthesis

The solid-state synthesis and its modification are the main focus of this thesis, therefore here we will present the general concepts of this synthesis method.

Two solid substance can react entirely in the solid phase, yielding a solid product. Solid-state reactions are fundamentally different from reactions in the liquid or gaseous states. The latter depend mainly on the intrinsic chemical reactivity and concentration of the reacting species, whereas in the former case, usually the most important factor is the arrangement of the chemical constituents in the crystal lattice. The diffusion of atoms/ions in solids is orders of magnitude slower in comparison to the rate in the gaseous/liquid phase. Consequently, the reactivity in solid phases is often determined by the crystal and/or defect structure, rather than by the chemical reactivity of the reacting species [3]. Furthermore, high temperatures are usually needed for solid-state reactions, due to the slow diffusion in solids.

The general mechanism of solid-solid reactions starts with a reaction at the interface between two solid reactants that need to be in contact. One or more solid products can be formed, which spatially separate the reactants. For the reaction to proceed the atoms/ions from the reactants have to diffuse through the layer of product. The schematic presentation of the mechanism is shown in Figure 2. As diffusion is usually the rate-limiting factor in solid-state reactions, the strategy to enhance the reactions is to shorten the diffusion paths and create more contacts between the reactant particles. In a two-component system, like the one presented in Figure 2, only the reaction

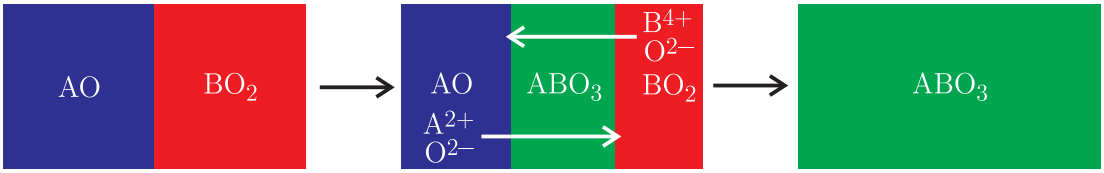

Figure 2: *Solid-state reaction scheme.* Example of the addition solid-state reaction. According to reaction $AO + BO_2 \longrightarrow ABO_3$ the ABO_3 phase is first formed between the two reacting layers. Next, reaction proceeds with diffusion of A^{2+}, $B^{4+}$and O^{2-} ions through the product layer to form the perovskite ABO_3 phase.

between the two components AO and BO_2 is possible[1]. We can increase the number of heterogeneous contacts between AO and BO_2 by decreasing the particle size and by homogeneously mixing the two phases. Looking at Figure 3 it is easy to understand the

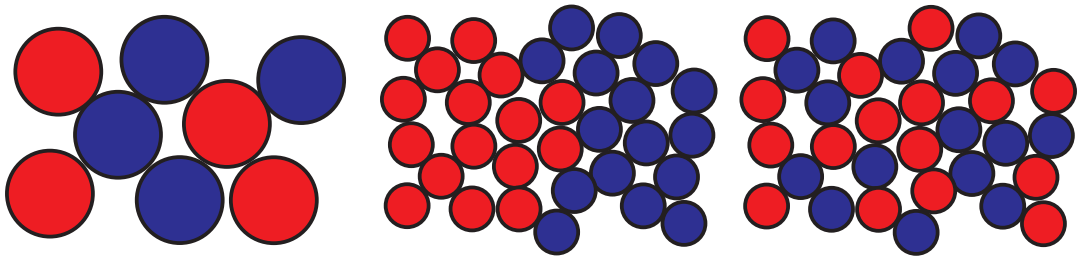

(a) Big particles (b) Heterogeneous arrangement (c) Homogeneous arrangement

Figure 3: *Different arrangements of particles for the* $AO+BO_2 \longrightarrow ABO_3$ *reaction.* Blue particles present the AO phase and red the BO_2 phase. In the case (a) big particles are present, therefore there is a small number of desired red-blue contacts. In the case (b) we have small particles; however, their distribution is heterogeneous, which allows only small number of desired contacts. In the case (c) small particles are distributed homogeneously, consequently a larger number of desired contacts occurs.

generally accepted concept in the field of solid-state synthesis: to get a fast reaction and a homogeneous product the starting powder mixture needs to consist of small particles that are mixed homogeneously. However, going to three or multi-component systems, homogenization is not always desired. Here, multiple reactions can occur, but not all of them are always desired. For example, if we have a reactant mixture containing three type of particles, *i.e.*, A, B, and C, reactions between A and B, A and C, and B and C are possible. Reaction between A and C could lead to a non-desired phase, which could prevent or slow down the formation of a targeted product. Such a problem is encountered in the synthesis of $Pb(Mg_{1/3}Nb_{2/3})O_3$ from a mixture of PbO, Nb_2O_5 and MgO, where PbO and Nb_2O_5 preferentially react to form the Pb-Nb pyrochlore phases. The pyrochlore phase is stable and it is difficult to eliminate it from the final product mixture. Furthermore this phase deteriorates the electrical properties of the material. Further details about this reaction are given in the following sections.

[1]The reactants could also decompose before the reactions, but this issue is not addressed here.

1.2 Electronic Ceramics

Electronic ceramics are widely used in electronics and electrotechnics, due to the variety of properties that can be designed for different ceramic materials. Traditionally, ceramics are known to have good insulation properties, and are used as electrical insulation, for example, for fuse housings [1]. However, with the development of new materials and with the design of their properties, many other interesting electrical properties can be achieved: high permittivity, superconduction, fast ion-conduction, piezoelectricity, and ferroelectricity. Today, ceramics are used in chip carriers, electronic packaging, capacitors, inductors, transducers, electrical insulation, electrodes, resistors, gas igniton, MEMS and many other applications [2].

1.2.1 Piezoelectric, Ferroelectric and Relaxor Materials

Piezoelectric materials are typical representatives of electronic ceramics. Under mechanical stress these materials develop charge, which is proportional to the applied force [4]:

$$D_i = d_{ijk} X_{jk} \,, \tag{1.1}$$

where D_i [As/m^2] is the charge density, d_{ijk} [As/N] is a tensor of piezoelectric coefficients, and X_{jk} [N/m^2] is the applied stress. This is the *direct* piezoelectric effect. In the *converse* piezoelectric effect, the applied field, E_k [V/m], induces a proportional strain, s_{ij}:

$$s_{ij} = d_{kij} E_k \,, \tag{1.2}$$

The direct piezoelectric effect is exploited in force, pressure, vibration, and acceleration sensors, while the converse effect is used for actuator and displacement devices. Probably the best known application of piezoelectric material is the use of quartz crystals in clocks. The quartz crystal is oscillating with a defined frequency, each oscillation produces charge on the crystal according to equation 1.1 and these changes of charge are used to measure time. Despite its widespread use, quartz has a relatively low piezoelectric constant $d_{33} = 2$ pC/N [5], for example, the highest values for piezoelectric ceramics are up to 700 pC/N [6, 7].

In contrast to the piezoelectric effect, which only occurs in materials with a non-centrosymmetric crystal structure, ***electrostriction*** is present in all dielectric materials, regardless of their crystal symmetry [8]. The effect is an example of quadratic coupling between the strain, s_{ij}, and the electric field, E_k:

$$s_{ij} = M_{ijkl} E_k E_l \,, \tag{1.3}$$

where M_{ijkl} [m^2/V^2] is the electrostriction coefficients tensor. The electrostriction can also be expressed with a more generally valid equation, where the strain is proportional to the square of the polarization, P_k [As/m^2], :

$$s_{ij} = Q_{ijkl} P_k P_l \,, \tag{1.4}$$

where Q_{ijkl} [m^4/(As)^2] and M_{ijkl} are related by $M_{ijmn} = \chi_{km}\chi_{ln}Q_{ijkl}$, and χ_{ij} [As/Vm] is the dielectric susceptibility. The electrostrictive effect is non-hysteretic and it is therefore used in devices where there is a requirement that hysteresis is absent in the response [8]. In Figure 4 the strain responses of piezoelectric ceramics (hard Pb(Zr,Ti)O_3, (PZT)) and relaxor ceramics (Pb($Mg_{1/3}Nb_{2/3}$)O_3, (PMN)) are compared. In the PZT

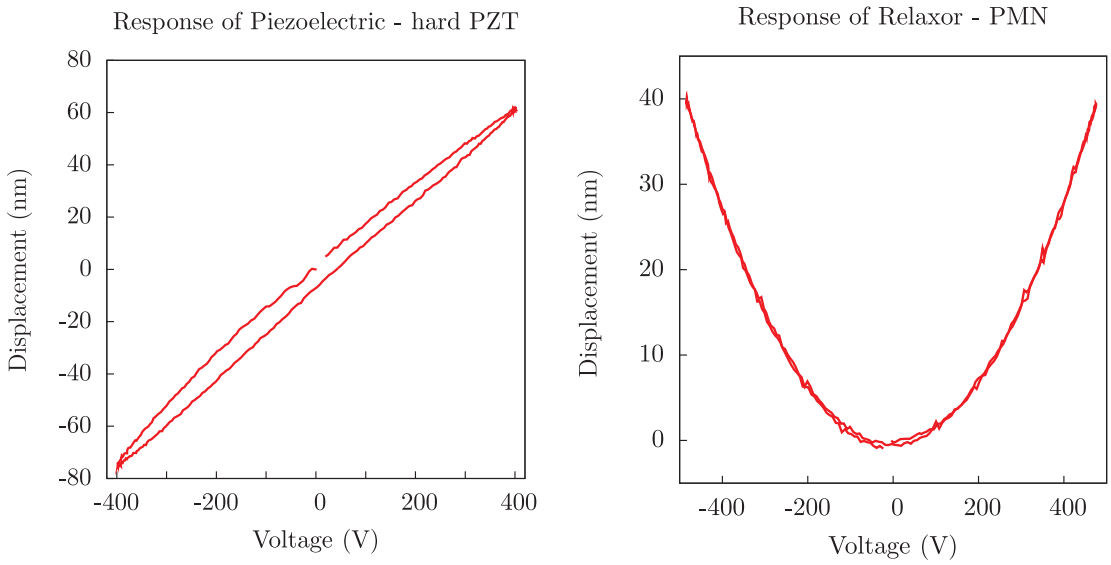

(a) Piezoelectric response

(b) Electrostrictive response

Figure 4: *Comparison of converse piezoelectric and electrostriction effect.* (a) Linear piezoelectric response of the hard PZT ceramics with pronounced hysteresis. (b) Quadratic electrostrictive response of the PMN ceramics with no hysteresis. In both cases the voltage was applied in the form of a bipolar single sinusoidal wave with a frequency of 100 Hz.

sample the displacement is a linear function of the voltage in accordance with equation 1.2; however, hysteresis is present. On the other hand, the typical non-hysteretic quadratic behavior of the displacement is observed in the case of PMN.

A subgroup of piezoelectrics are ***ferroelectric*** materials. For a material to be ferroelectric it must, in addition to being polar, possess a spontaneous polarization, *i.e.*, polarization, P_s, in the absence of an external electric field. Furthermore, the direction of P_s is switchable with an external electric field [4]. In most ferroelectric materials the transformation from a ferroelectric to a non-polar paraelectric phase is observed at higher temperatures. The temperature of the transformation is called the *Curie temperature*, T_c, and corresponds to the peak in the dielectric permittivity vs. temperature, see Figure 5. When measuring the polarization vs. electric field of a ferroelectric material a typical hysteretic $P-E$ loop is observed. During this process the polarization is switched by the electric field, see Figure 6. The formation of the $P-E$ loop starts at zero field where the polarization is also zero. When the field is increased to positive values the polarization is also positive. When decreasing the field back to zero, the polarization reaches the value of $+P_r$, called the remanent polarization (point 2 in Figure 6a). A negative field of $E=-E_c$ is needed to reach $P=0$ (point 3), E_c is the coercive field. With further decreasing of the field, the polarization goes to negative values. Next, at $E=0$, $P=-P_r$ (point 4). A positive field $E=+E_c$ is needed for the polarization to go back to zero. During the looping the positions of the ions in the unit cell change. When the polarization is zero the centers of the positive and negative charge coincide. At the point where the polarization is flipped "up", the cations A and B move up, while the anions O displace down, see Figure 6b. The most evident change is the displacement of the central B cation. The ions are displaced in the opposite direction when the polarization is pointing "down".

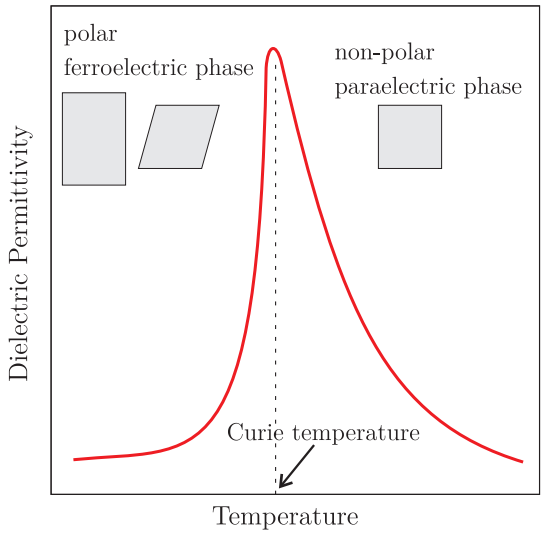

Figure 5: *Schematic presentation of the temperature dependence of dielectric permittivity during a ferroelectric-to-paraelectric transformation.* During the ferroelectric-to-paraelectric transformation a peak in the dielectric permittivity is observed. The temperature of the transformation is called the Curie temperature.

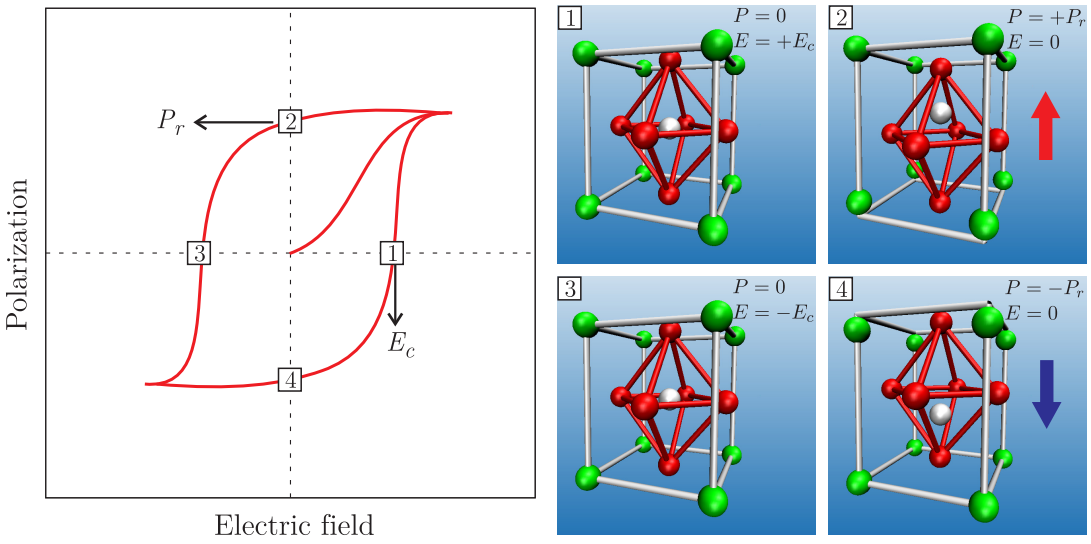

(a) Ferroelectric loop (b) Atom displacements

Figure 6: *Schematic presentation of the ferroelectric loop.* (a) Polarization – Electric field ($P-E$) dependence for a ferroelectric material. (b) Presentation of the movement of the atoms in the unit cell during loop formation. The example shows ABO_3 perovskite unit cell, with A atoms colored green, B atom white, and O atoms red. The images correspond to the marked states in the loop.

Relaxors are a group of materials similar to ferroelectrics; however, their behavior is different in some respects. The most obvious difference is an anomalously strong frequency dispersion of the dielectric permittivity at its maximum values, see Figure 7. Similar to normal ferroelectrics, at high temperatures they exist in a non-polar

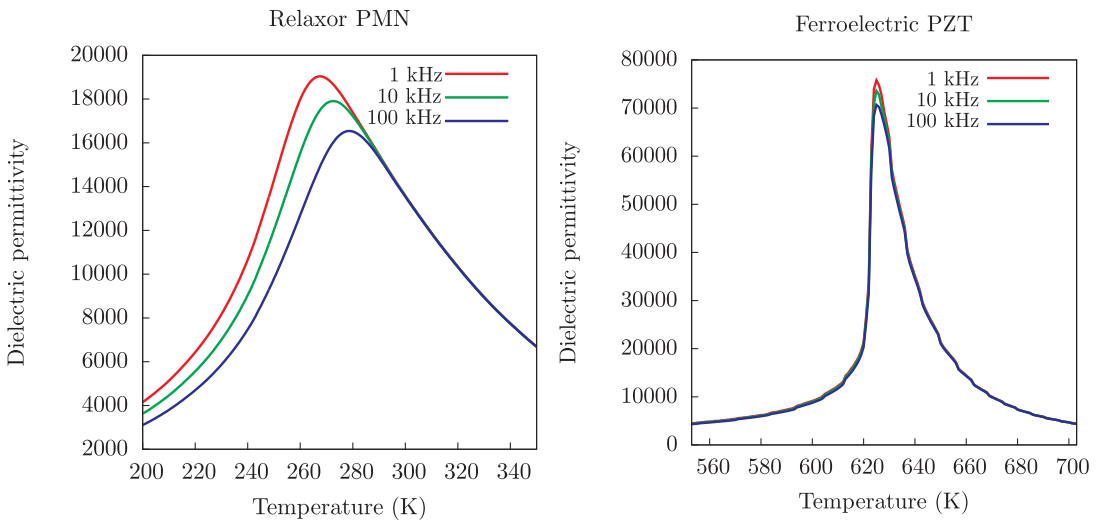

(a) Relaxor (b) Ferroelectric

Figure 7: *Dependence of dielectric permittivity on temperature for relaxor and ferroelectric materials.* The dielectric permittivity is measured at 1, 10, and 100 kHz in dependence of the temperature for (a) PMN ceramic and (b) PZT ceramic.

paraelectric phase, but during cooling they transform into the phase where polar regions of nanometer size with randomly distributed directions of the dipole moments appear [9]. The best known examples of these materials are $Pb(Mg_{1/3}Nb_{2/3})O_3$ and $Pb(Zn_{1/3}Nb_{2/3})O_3$. They exhibit a set of properties, that are useful in some applications: a) a high dielectric permittivity over a wide temperature range, b) large electrostrictive coefficients, c) a strong piezoelectric activity when the material is under a DC electric field, and d) a strong electrooptic activity [8].

Relaxor-ferroelectrics are solid solutions between relaxors and normal ferroelectrics [8]. The solid solutions of $Pb(Mg_{1/3}Nb_{2/3})O_3$ and $Pb(Zn_{1/3}Nb_{2/3})O_3$ with $PbTiO_3$ (PT), denoted as PZN-PT and PMN-PT, exhibit extremely good piezoelectric properties. In the single-crystal form these materials can reach d_{33} values of several 1000 pC/N, and an electromechanical coupling coefficient up to 0.94 [10]. In the form of ceramics the d_{33} is lower, but still reaches a very high value of $\sim$ 700 pC/N [6, 7]. Recently, a large electro-optic effect has also been measured in 0.75PMN-0.25PT, which makes this material a possible alternative to the conventionally used (Pb,La)(Zr,Ti)O_3 (9/65/35) for electro-optic applications [11].

1.2.2 PMN & PMN-PT

$Pb(Mg_{1/3}Nb_{2/3})O_3$ is a model relaxor system with the perovskite ABO_3 crystal structure, where the A sites are occupied with Pb^{2+} and the B sites with Nb^{5+} and Mg^{2+} ions. As already explained, this material exhibits some interesting properties, like a high dielectric permittivity, a large electrostrictive response, and a large piezoelectric activity when it is in a large enough DC field. Therefore, it is attractive for capacitor and actuator applications [8, 12, 13, 14].

$Pb(Mg_{1/3}Nb_{2/3})O_3$ forms a solid solution with $PbTiO_3$ (PT), yielding relaxor-ferroelectric $(1-x)Pb(Mg_{1/3}Nb_{2/3})O_3 - xPbTiO_3$ materials, as explained in the previous section. At room temperature the structure of PMN is cubic, with the

addition of PT it transforms through rhombohedral, monoclinic to a tetragonal phase, see Figure 8a. In this system the morphotropic phase boundary (MPB) is located near

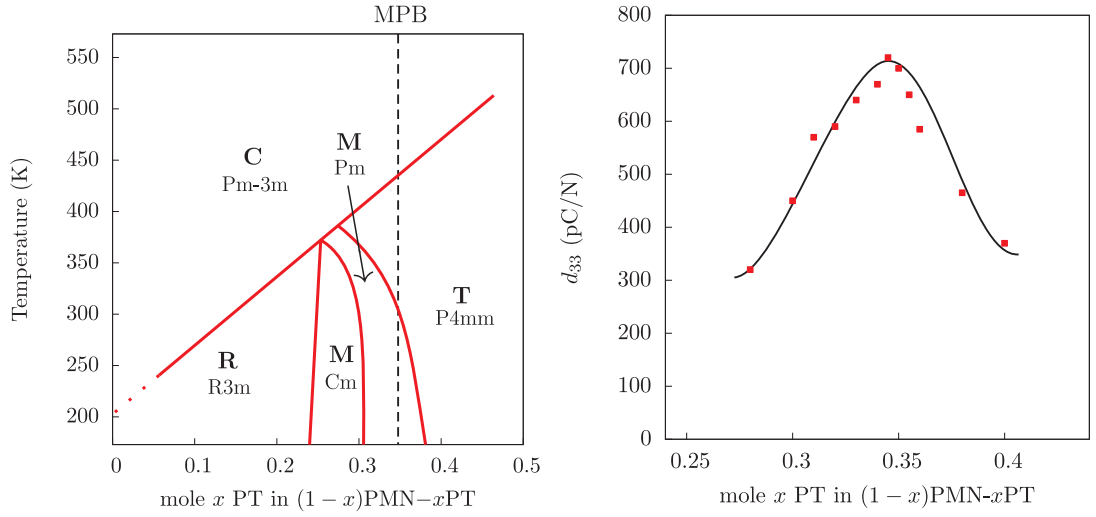

(a) Phase diagram

(b) d_{33} vs. composition

Figure 8: *Properties of* $(1-x)\mathrm{Pb}(\mathrm{Mg}_{1/3}\mathrm{Nb}_{2/3})\mathrm{O}_3 - x\mathrm{PbTiO}_3$ *in dependence of the composition.* (a) Phase diagram of the $(1-x)\mathrm{Pb}(\mathrm{Mg}_{1/3}\mathrm{Nb}_{2/3})\mathrm{O}_3 - x\mathrm{PbTiO}_3$, after Algueró [15]. C - cubic phase, M - monoclinic phase, R - rhombohedral phase, T - tetragonal phase, MPB - morphotropic phase boundary. (b) Dependence of the piezoelectric coefficient on the composition of $(1-x)\mathrm{Pb}(\mathrm{Mg}_{1/3}\mathrm{Nb}_{2/3})\mathrm{O}_3 - x\mathrm{PbTiO}_3$ ceramics, after Kelly et al. [6].

$x \approx 0.35$. A huge enhancement in the piezoelectric and other electrical properties is observed near the MPB, see Figure 8b [6].

One of the major problems concerning PMN-based materials is the difficulty in preparing them in a phase-pure condition [12]. The conventional solid-state synthesis using the simultaneous mixing of constituent oxides usually yields, in addition to the perovskite, the pyrochlore phases. The latter deteriorate the dielectric, electrostrictive, ferroelectric and piezoelectric properties of the perovskite PMN-based materials.

The synthesis of PMN from a mixture of PbO, MgO, and $\mathrm{Nb}_2\mathrm{O}_5$ is characterized by the complexity of the reactions described by the following reaction sequence [16]:

$$3\mathrm{PbO} + 2\mathrm{Nb}_2\mathrm{O}_5 \longrightarrow \mathrm{Pb}_3\mathrm{Nb}_4\mathrm{O}_{13}\ \text{(cubic pyrochlore)}\,, \tag{1.5}$$

$$\mathrm{Pb}_3\mathrm{Nb}_4\mathrm{O}_{13} + \mathrm{PbO} \longrightarrow 2\mathrm{Pb}_2\mathrm{Nb}_2\mathrm{O}_7\ \text{(rhombohedral pyrochlore)}\,, \tag{1.6}$$

$$\begin{aligned} 3\mathrm{Pb}_2\mathrm{Nb}_2\mathrm{O}_7 + \mathrm{MgO} \longrightarrow\ & 3\mathrm{Pb}(\mathrm{Mg}_{1/3}\mathrm{Nb}_{2/3})\mathrm{O}_3\ \text{(perovskite)} \\ & + \mathrm{Pb}_3\mathrm{Nb}_4\mathrm{O}_{13}\ \text{(cubic pyrochlore)}\,. \end{aligned} \tag{1.7}$$

In a homogeneous mixture of PbO, $\mathrm{Nb}_2\mathrm{O}_5$, and MgO, at an elevated temperature lead oxide and niobium oxide preferentially react at a relatively low temperature to form pyrochlores, see Equations 1.5, 1.6. The pyrochlore phase subsequently reacts with MgO to form the perovskite PMN, but due to its high stability the pyrochlore phase remains in the mixture, see Equation 1.7. Similar reaction pathways, with slightly different

compositions of pyrochlore phases, were also found by other authors [17, 18]. In multi-component systems all reactions are not necessarily desirable, as noted in Section 1.1.1. In this case the reaction between PbO and Nb_2O_5 is undesired and should be avoided, or at least suppressed. This was first achieved by Swartz and Shrout, who proposed a new synthesis approach - the "columbite "method [18], which is a two-step, solid-state synthesis method. First, the columbite, $MgNb_2O_6$, is synthesized:

$$MgO + Nb_2O_5 \xrightarrow{1000-1200^\circ C} MgNb_2O_6 \text{ (columbite precursor)} \tag{1.8}$$

and in the second step, the reaction of columbite and lead oxide yields the perovskite PMN:

$$MgNb_2O_6 + 3PbO \xrightarrow{900^\circ C} 3Pb(Mg_{1/3}Nb_{2/3})O_3\,. \tag{1.9}$$

With the synthesis of the columbite in the first step, the reaction between lead oxide and niobium oxide is prevented, and consequently the formation of the pyrochlore phase is avoided. This method is widely used for PMN solid-state synthesis and yields a material with none or only a small amount of the pyrochlore phases. However, in comparison to the conventional solid-state synthesis it requires at least two calcination steps. The columbite method has also been successfully modified for the $(1-x)$PMN-xPT synthesis [6, 19, 20]. Here, in the second step, both PbO and TiO_2 are added to $MgNb_2O_6$ to form the reaction mixture. In another modification of this method, columbite is first synthesized, which in the next step reacts with PbO and $PbTiO_3$ [21].

Although the columbite method is the most widely used for the synthesis of PMN-based materials, some other approaches have been developed, usually with the aim of avoiding the additional calcination step. Methods such as molten-salts synthesis [22], auto-combustion synthesis [23], the hydrothermal method [24], sol-gel synthesis [25, 26, 27, 28], and other wet chemistry methods [29, 30, 31, 32, 33] are usually expensive and difficult to scale up. Pyrochlore-free PMN and PMN-PT were also synthesized with the mechanochemical method [34, 35, 36, 37], which uses high-energy milling to support the reaction. During the milling chemical reactions between the reactant powders occur. Usually heating is needed to finish the reactions and get a total conversion to perovskite. Yu et al. introduced polyethylene glycol in the solid-state synthesis of PMN-PT and produced pure perovskite ceramics [38]. Gu et al. coated the Nb_2O_5 particles with $Mg(OH)_2$ to prevent physical contacts between the niobium and lead oxide particles and thereby hindered the formation of pyrochlore phases [39, 40]. A similar, double-coating method was presented by Xu et al. [41], where they first coated Nb_2O_5 particles with a layer of Mg-citric acid polymeric complex, and on top of this layer a Pb-citric acid polymeric complex was coated. Pure perovskite PMN powder was then synthesized from these double-coated particles in a single-calcination step. PMN ceramics were also synthesized from an aqueous suspension; however, no details about the synthesis conditions are given [42].

1.3 Colloidal Suspensions

The term *colloidal* refers to molecules or particles dispersed in a medium that have, at least in one direction, a dimension roughly between 1 nm and 1 μm, or that in a system discontinuities are found at distances of that order [43]. The above definition of colloidal says that it is not necessary for all three dimensions of a colloidal particle to be small. That means that the term colloidal can be used for a large variety of systems: systems with a colloidal size in all three dimensions, like printing ink, systems with a colloidal

size in two dimensions, like cellulose fibers, or systems with colloidal size in just one dimension, like foam, where the thickness of the lamella between the two gas bubbles is in the colloidal range [43, 44]. This broad definition of colloidal systems includes many familiar substances that we run across in everyday life, *e.g.*, paint, nail polish, ink, milk, ice cream, mayonnaise, fog, etc. The dispersed phase and dispersion medium can be in the solid, liquid or gaseous state, for examples see Table 1. As can be seen from Table 1

Table 1: *Types of colloidal dispersions.* Dispersed phase and dispersion medium can be in solid, liquid or gaseous state, the combinations of them gives us different types of colloidal dispersions. Adopted from [44].

Dispersed phase	Dispersion medium	Notation	Technical name	Examples
Solid	Gas	S/G	Aerosol	Smoke
Solid	Liquid	S/L	Sol, suspension	Paint, printing ink
Solid	Solid	S/S	Solid suspension	Ruby glass (Au in glass)
Liquid	Gas	L/G	Aerosol	Fog, spray
Liquid	Liquid	L/L	Emulsion	Milk, mayonnaise
Liquid	Solid	L/S	Solid emulsion	Opal
Gas	Liquid	G/L	Foam	Foams
Gas	Solid	G/S	Solid foam	Expanded polystyrene

a suspension is a dispersion of solid colloidal particles in a liquid medium.

In *normal* solutions (*e.g.*, an aqueous solution of sodium chloride NaCl(aq)) the solute and solvent molecules (ions, particles) are of comparable size, whereas in colloidal dispersions the dispersed particles are order(s) of magnitude larger than the particles of the dispersion medium [44]. Another important feature of colloidal systems is a large contact area between the particles and the dispersion medium, which is due to their colloidal size. This results in large inter-particle forces, which have a strong influence on macroscopic properties of the dispersions [44, 45].

Colloidal suspensions and their properties are of great importance in ceramics processing. We come across suspensions in several steps of ceramics production. For example, in the case of the precipitation method for ceramics synthesis the final product is a suspension of ceramic particles. Furthermore, practically every ceramic production cycle is composed of several milling/homogenization steps, during these processes the ceramic particles are usually suspended in a liquid phase. Ceramic suspensions are also used in shaping processes, *e.g.*, slip casting, tape casting, and extrusion methods.

1.3.1 Inter-particle Forces

The forces that act between the particles have a great influence on many macroscopic properties of colloidal systems. For example, the viscous behavior of a colloidal suspension is governed by the inter-particle forces. The balance between attractive and repulsive forces determines the stability of a suspension. Understanding and manipulating the amplitude of these forces is of great importance in many technological processes.

The forces between the colloidal particles are important in connection to this work. Controlling the inter-particle forces enables us to control the agglomeration behavior of the suspensions of reagent particles used in the synthesis of PMN-based materials. Our idea of using inter-particle forces to control the structure of the agglomerates and

consequently influence the solid-state reactions is explained in the Aims and Hypothesis of this thesis.

The inter-particle potential can be divided into several contributions [45]:

$$U^{\text{total}} = U^{\text{vdW}} + U^{\text{elect}} + U^{\text{steric}} + U^{\text{structural}}, \tag{1.10}$$

where U^{vdW} is the *van der Waals* potential, U^{elect} is the *electrostatic* potential, U^{steric} is the contribution of the *steric* forces, and $U^{\text{structural}}$ is the potential arising from *structural* forces. The first two contributions are dominant in the case of charged colloidal particles without added polymers and are explained in detail below. By adsorption of polymeric species on the surface of colloidal particles, a repulsive steric interaction between the particles is usually achieved. If the polymeric chains are charged, as for example in the case of polyacrylic acid, the contribution of the steric and the electrostatic part is present and is summed up into the *electrosteric* interaction [46, 47, 48]. For a comparison of the steric and electrosteric stabilization, see Figure 9. Non-adsorbing particles and/or

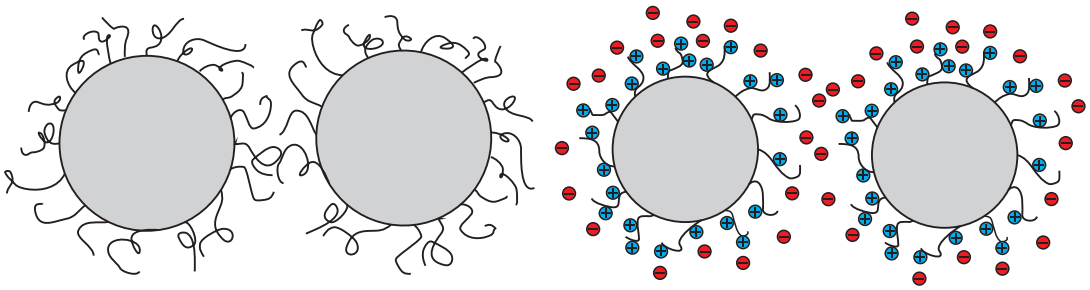

(a) Steric stabilization (b) Electrosteric stabilization

Figure 9: *Schematic presentation of polymeric stabilization of colloidal particles.* (a) Polymers adsorbed on particle surfaces are preventing the colloids from coming into contact and thus provide steric stabilization. (b) Electrosteric stabilization is achieved by adsorption of polyelectrolyte chains to the particle surface. Here both electrostatic and steric stabilizations are present.

molecules, which are smaller in comparison to the colloidal particles, or even solvent molecules, can cause structural forces. These are the so-called *entropic depletion forces* or *solvation* forces in the case of a solvent [49, 50, 51, 52, 53]. These forces can either promote stabilization or destabilization of the colloidal system [45]. In Figure 10 the mechanism of depletion flocculation is shown.

Van der Waals Forces

The *van der Waals* forces, also named *London-van der Waals* or *dispersion* forces, have their origin in the electric dipole interactions between atoms and/or molecules. In the case of bigger particles, *e.g.*, colloidal particles, the dispersion interactions between all the atoms/molecules that compose a particulate particle contribute to the combined interaction between two colloidal particles. In general there are two approaches to calculating the van der Waals interaction between colloidal particles [54]. One is the *macroscopic* approach proposed by Lifshitz [55]. Here, the interactions are entirely derived from macroscopic electromagnetic properties of the medium and the particles. It has two drawbacks: *i*) it is difficult to obtain all experimental data of the particles and the medium needed for the calculation, and *ii*) it is hard to derive the interaction for

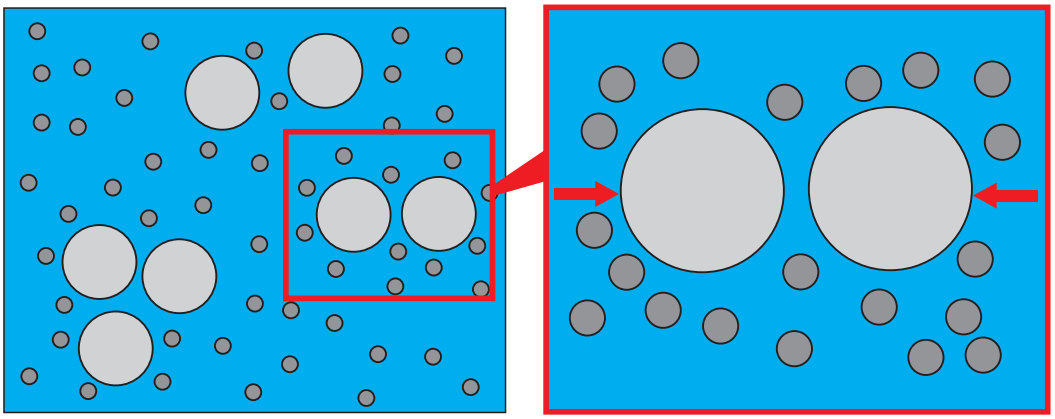

Figure 10: *Schematic presentation of the depletion interaction between two colloidal particles.* It is not entropically favorable for the small particles to be caught in between the colloidal particles. Due to the deficiency of the small particles in between, the pressure caused by the collisions of the particles outside pushes the colloids together.

geometries other than a plate-plate arrangement [54]. The other, *microscopic*, approach was introduced by Hamaker [56] in 1937. This is also the one used in this work. Here, the interaction between two colloidal particles is calculated with a pairwise summation of all the interactions between the atoms/molecules that build a particle,

$$U^{\mathrm{vdW}} = \frac{1}{2}\sum_{i=1}^{N}\sum_{\substack{j=1\\ j\neq i}}^{N} U_{ij}^{\mathrm{int}}(r_{ij})\,, \tag{1.11}$$

where U_{ij}^{int} is the interaction energy of atoms/molecules i and j separated by the distance r_{ij}. In his article Hamaker replaced the summation with a double integration over the volume of both particles and used the London-van der Waals interaction between atoms for the calculation [56],

$$U^{\mathrm{vdW}} = \int_{V_1}\int_{V_2} -\frac{q^2\lambda}{r^6}\, dV_1 dV_2\,, \tag{1.12}$$

where q is the density of atoms in the material, r is the distance between the volume elements dV_1 and dV_2, and λ is the London-van der Waals constant. The London-van der Waals interaction, $-\frac{\lambda}{r^6}$, is actually the attractive part of the Lennard-Jones potential. The result obtained from this integration can be split into a purely geometrical part and a constant,

$$U^{\mathrm{vdW}} = -A_{ij}G(h)\,. \tag{1.13}$$

$A = \pi^2 q_i q_j \lambda_{ij}$ is known as the *Hamaker constant* and is a function of a material from which the particles i and j are composed and the medium through which they interact. If the particles i and j are from different material A_{ij} is calculated as the geometrical mean of A_i and A_j,

$$A_{ij} = \sqrt{A_i A_j}\,. \tag{1.14}$$

$G(h)$ is the geometrical part, dependent on the distance between the particle surfaces, h, and the size and shape of the particles. The van der Waals interaction between two spherical colloidal particles, which is used in this work, is written in the chapter Materials and Methods, see Equation 3.2.

The major deficiency of the Hamaker approach is the assumption of complete additivity of intermolecular forces, this summation is neglecting the influence of other atoms/molecules on the interaction between the atom/molecule i and j. This simplification usually results in overestimating the interaction [54]. However, the Hamaker interaction is, due to its simplicity, widely used [57, 58, 59, 60, 61, 62, 63].

The dispersion forces between two colloidal particles are usually attractive, promoting the agglomeration of colloidal particles in suspensions and consequently the separation of a liquid and solid phase. To prevent the agglomeration and stabilize the suspensions, opposing repulsive forces between colloids, *e.g.*, electrostatic, should be present.

Electrostatic Forces

Most colloidal particles develop an electrostatic charge on their surface when they are immersed in water. This surface charge causes the electrostatic interactions between the particles, the forces can be either attractive or repulsive. The origin of the charge on the surface of the particles can be explained by several mechanisms.

In the case of AgI, the *specific dissolution* of ions from the crystal lattice causes the surface charge on the AgI particle. The Ag^+ ions have in comparison to the I^-, a greater tendency to dissolve in water and escape from the crystal lattice, yielding the negative charge on the surface. The surface charge can be, in this case, controlled by the concentration of silver or iodide ions in the water [54].

Another possibility to create a surface charge is the *ionization of the surface groups*, for example, $-$COOH, $-SO_3H$ in the case of functionalized polymeric particles. In contact with water these groups ionize,

$$\text{Particle–COOH} + H_2O \rightleftharpoons \text{Particle–COO}^- + H_3O^+ , \tag{1.15}$$

yielding a negative charge on the surface. Here, the surface charge can be mediated by pH [64].

In the case of the metal oxides, *e.g.*, TiO_2, Al_2O_3, SiO_2, their surfaces react with water and become hydroxylated, as shown by scanning tunneling microscopy and density-functional theory studies [65, 66]. Hydroxylated surface sites can then react with H_3O^+ or OH^-, yielding either a positive or negative charge:

$$\text{M–OH} + OH^- \rightleftharpoons \text{M–O}^- + H_2O , \tag{1.16}$$

$$\text{M–OH} + H_3O^+ \rightleftharpoons \text{M–OH}_2^+ + H_2O . \tag{1.17}$$

At low pH values the surfaces are usually positively charged, whereas at high pH values they acquire a negative charge. At certain characteristic pH value the net charge of the surface is zero, this is called the point of zero charge (PZC). There is another characteristic pH value, called the isoelectric point (IEP), which is the point where the zeta-potential is zero. PZC and IEP are not always equal, which can be the consequence of the ions specifically adsorbed to the surface.

The changes in the surface charge can also be caused by *specific adsorption of ions* to the solid surface. The adsorption can increase or decrease the surface charge, and in some cases it may also lead to a charge reversal [67].

Whatever the origin of the charge on the surface of the particle, when the surface is in contact with a dispersion medium this charge is exactly balanced by the opposite charge in the medium. Adjacent to the surface, the layer with a higher concentration

of *counter-ions* and a lower concentration of *co-ions*, as compared to the bulk concentrations, is present. The charged surface with the adjacent counter-ions layer is called the electrical double-layer. The theoretical description of the double-layer was independently given by Gouy and Chapman (see, for example [44]). Their model is based on several assumptions: (*i*) the solid surface is infinite, flat and impenetrable, (*ii*) the surface charge is uniformly smeared out over the surface, (*iii*) ions in the solution are point charges, (*iv*) the solvent is continuum with a constant electric permittivity. The function of the electrical potential change with distance from the surface is calculated by solving the *Poisson-Boltzmann* equation [68],

$$\nabla^2\psi = -\frac{1}{\varepsilon_0\varepsilon_r}\sum_i n_i^0 z_i e_0 e^{-\frac{z_i e_0 \psi}{k_b T}}\,, \tag{1.18}$$

where ψ is the electrical potential, n_i^0 is the number density of ions of valency z_i, k_b is the Boltzmann constant, T is the temperature, $\varepsilon_0\varepsilon_r$ the permittivity of the medium, and e_0 the elementary charge. The approximate solution of Equation 1.18 gives the exponential fall of the electric potential from a charged surface (for the exact solution see, for example, [44, 54]):

$$\psi(x) = \psi_0 e^{-\kappa x}\,, \tag{1.19}$$

where ψ_0 is the electrostatic potential at the surface, κ is the Debye-Hückel screening length, and x is the distance from the surface. ψ falls to $1/e$ of the surface potential at the distance κ^{-1}, which is known as the thickness of the double layer.

The extension of the Gouy-Chapman model was devised by Stern. His model takes into account the finite size of the ions and their specific adsorption to the surface. The ions cannot touch the interface, but are limited to an approach equal to their radius. In the region inside the *Stern plane* the fall of the potential is linear and further on it falls exponentially, see Figure 11. For a description of the double layer another plane is important - the *slip plane*. The slip plane separates the diffuse layer from the hydrodynamically stagnant layer of fluid, where no hydrodynamic flow can develop, see Figure 12. When the particle is moving this layer of fluid is traveling with the particle. At the position of the slip plane, the electrostatic potential can be measured, and it is defined as the *zeta-potential*. It can be measured by electrophoresis. Due to the surface charge the particle is moving in the electric field, and its velocity is dependent upon the electric field and the zeta-potential. By knowing the electric field and measuring the velocity, the zeta-potential can be calculated.

When two charged colloidal particles approach each other in the solution, their diffuse double layers overlap, giving rise to the force between them. This force is, in the case of like-charged particles, repulsive and in the case of oppositely charged particles attractive. There are several models for calculating the double-layer interaction using different approximations [54]. In the case of an interaction of two spherical particles the screened Coulomb potential in the form of *Yukawa* [70] or *Hogg-Healy-Fürstenau* (HHF) [71] approximations are usually employed, the latter is widely used in chemistry literature [57, 58, 63, 72]. The equation describing the HHF interaction between two spherical particles is given in Materials and Methods, see Equation 3.3. Due to the approximations, *i.e.*, linearization of Poisson-Boltzmann equation and Derjagun approximation, its validity is limited to not-too-large potentials ($\psi_0 < 60$ mV) and a thin double layer in comparison to the particle radius, a, ($\kappa a > 5$). Most parameters used for the calculation of this interaction can be exactly taken from the experiments. The HHF model is considered to be suitable for use in this work.

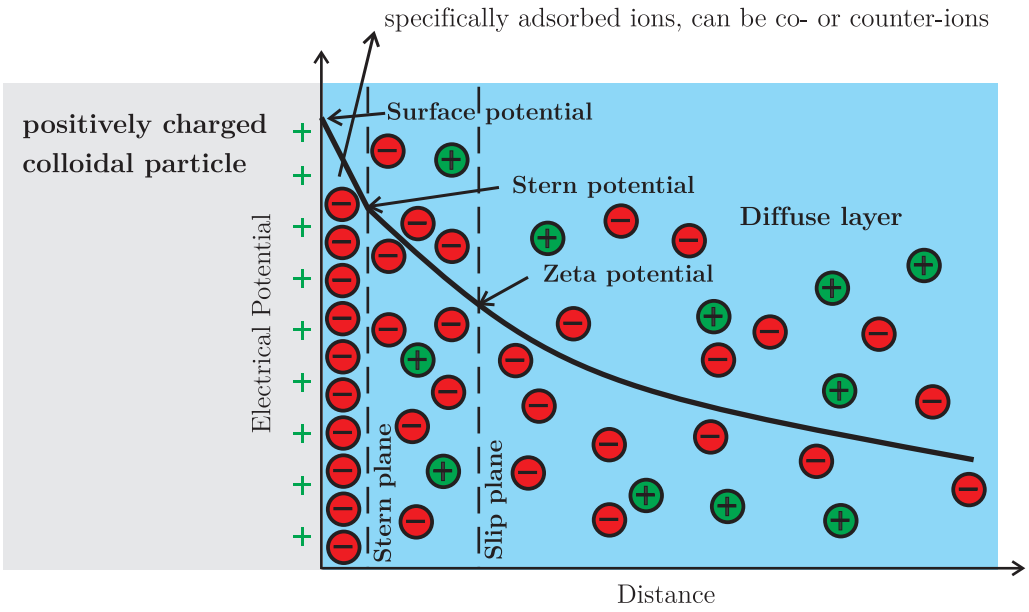

Figure 11: *Schematic presentation the electrical double layer.* The first layer adjacent to the charged surface is the Stern layer of specifically adsorbed ions, here the electrical potential falls linearly with distance. Next to the Stern layer is the diffuse layer, where the potential falls exponentially. The value of the electrical potential at the slip plane is the zeta-potential. After [54, 69].

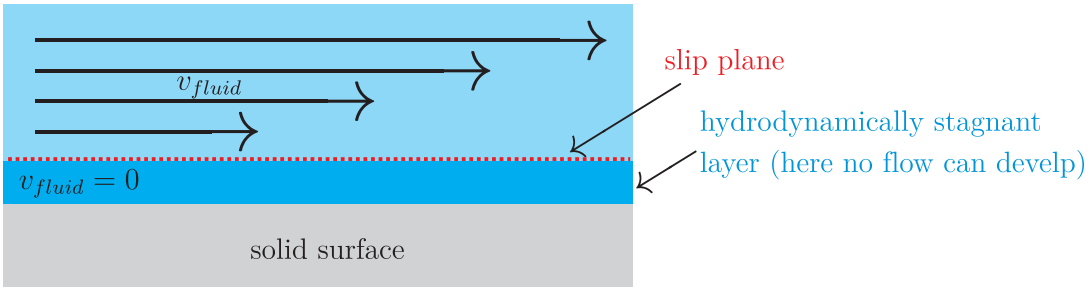

Figure 12: *Schematic presentation the slip plane.* When the particle is moving in the liquid, thin layer of fluid at its surface is moving with the particle. The stagnant layer, which ends with the slip plane, is usually ∼0.5 nm thick [63].

DLVO theory

In 1940s **D**erjaguin and **L**andau [73], and **V**erwey and **O**verbeek [74] developed a theory for estimating the stability of charged colloidal particles dispersed in a medium. The *DLVO* theory is the best known theory in the field of colloidal science, its name is composed from the authors' initials. The central concept in this theory is the assumption that the total interaction potential is the sum of the van der Waals potential and the electrical double-layer potential,

$$U^{\text{total}} = U^{\text{vdW}} + U^{\text{elect}} . \tag{1.20}$$

In the case of two particles composed of the same material the van der Waals forces are attractive, while electrical double layer interaction is repulsive. The sum of these two interactions can therefore be positive or negative and can lead to either the destabilization or stabilization of colloidal dispersions. With control of the total potential between

the particles we can control the stability of the dispersed system, see Figure 13.

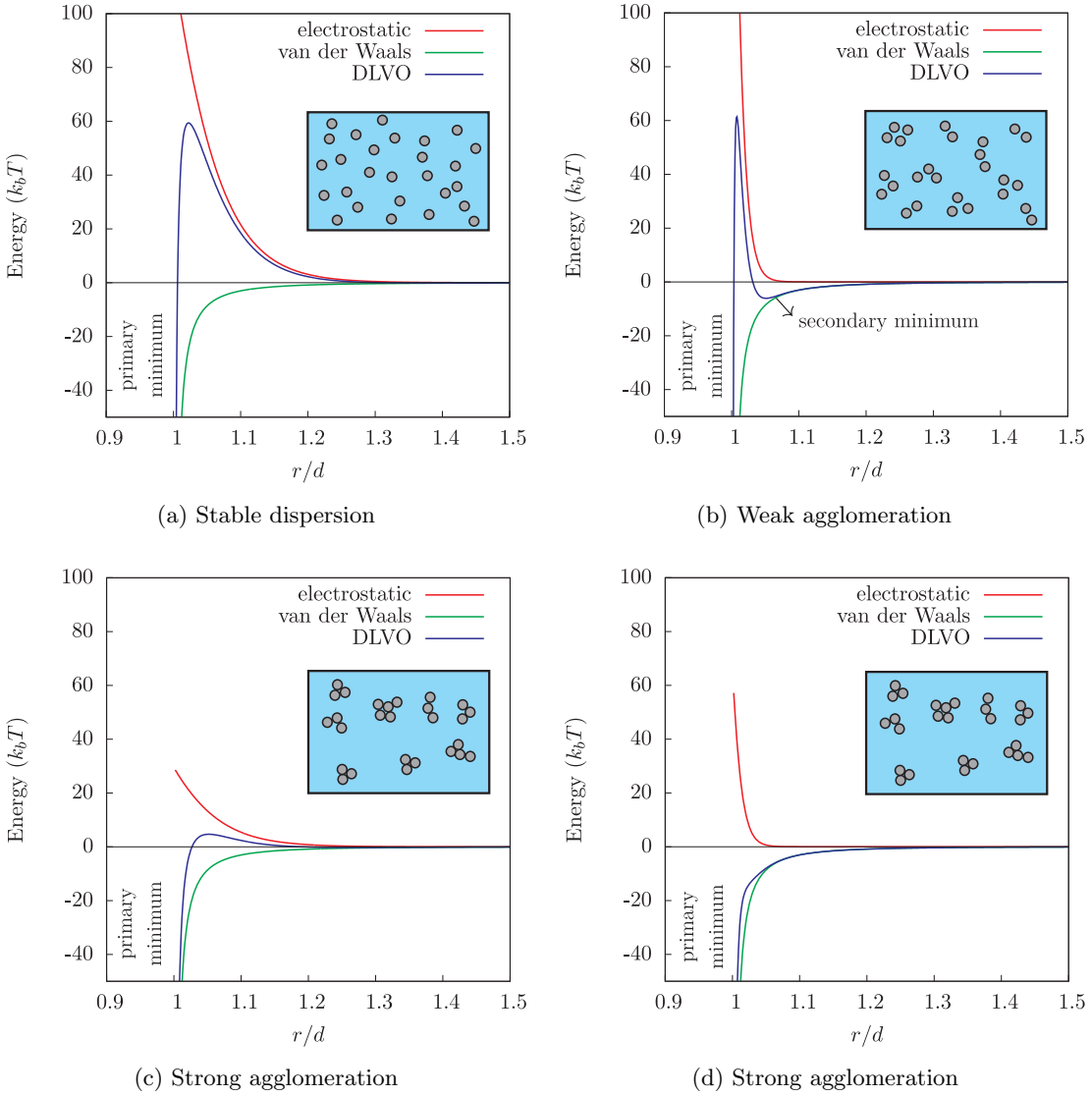

(a) Stable dispersion

(b) Weak agglomeration

(c) Strong agglomeration

(d) Strong agglomeration

Figure 13: *Influence of the DLVO interaction on the colloidal stability*. The DLVO potential with the electrostatic and van der Waals contributions is presented for four different situations. In every figure we present the inset with the scheme of the system corresponding to the shown potential. (a) Repulsive forces are predominant. The potential maximum reaches a value of $\sim$60 k_bT and prevents the particles from agglomerating in the primary minimum. (b) Repulsive forces are still dominant, but a shallow secondary minimum is present. The particles are trapped in this minimum and are weakly agglomerated. (c) The potential maximum is relatively low $\sim$5 k_bT. Due to thermal energy the particles overcome the maximum and are strongly agglomerated in the primary minimum. (d) Here, the repulsion forces are too low and the particles strongly agglomerate.

The DLVO theory is widely used in the field of colloidal science. Although several simplifications and assumptions are made in the models for the calculation of the electrical double layer and also van der Waals forces, good agreement with experimental results is achieved. The first comparison with experimental results was already realized

by the founders of the theory. They theoretically confirmed the experimental *Schulze-Hardy* rule, which states that the valence of the electrolyte counter-ions has a decisive influence on the stability of the suspension. Furthermore, they showed that the critical agglomeration concentration of the electrolyte is inversely proportional to the valence of the electrolyte ions [73, 74]:

$$c_{critical} \propto \frac{1}{z^6}\,, \tag{1.21}$$

where $c_{critical}$ is the critical agglomeration concentration and z is the valence of the electrolyte ions. This relation agrees with the experimental findings. The agreement of the theory with respect to the experimentally measured inter-particle forces was presented later. It is hard to directly measure the interaction between colloidal particles. In the past researchers tackled the problem with surface force apparatus (SFA), which had a big deficiency in that it was practically useful only for an interaction with molecularly flat *mica* surfaces [68]. With the invention of the atomic force microscope (AFM) the forces between various materials in various geometries could be measured. One of the most useful is the colloidal probe technique, where the colloidal particle is glued to the cantilever and then the force between the particle and the surface or an other particle on the surface can be measured by the deflection of the cantilever [75], see Figure 14a. The agreement between the measured forces with the DLVO theory is good, see for

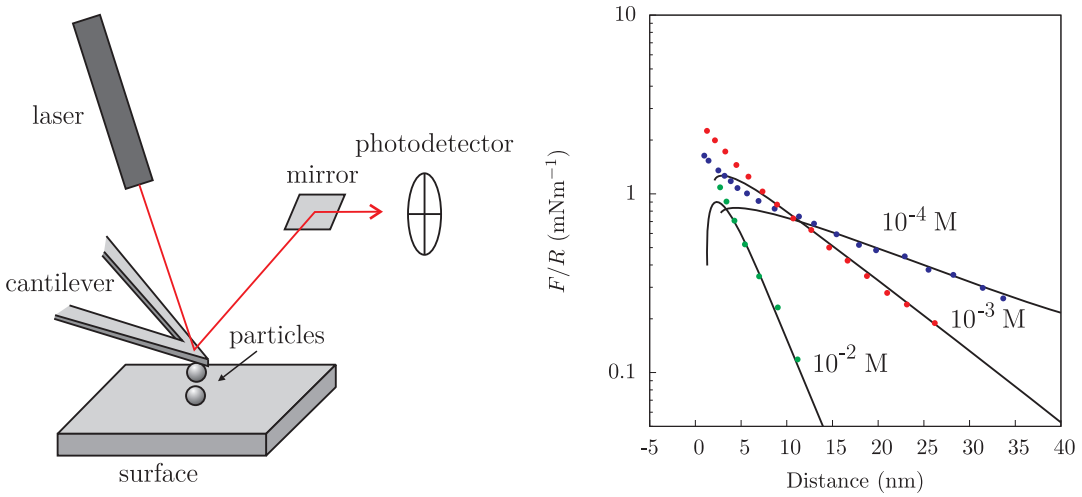

(a) Colloidal probe AFM technique (b) Force between a silica particle and a flat surface

Figure 14: *Direct force measurement with colloidal probe AFM technique.* (a) Schematic presentation of direct force measurement with a colloidal probe AFM setup. We can measure the sphere-sphere or sphere-plate interactions. After [68]. (b) Force as a function of separation for the interaction between a spherical silica particle and a flat silica substrate. The points represent the experimental measurements with the AFM. The curves are the fits using DLVO theory with an attractive van der Waals interaction and a repulsive double layer interaction. After [75].

example [68, 75, 76]. Usually, researchers are fitting the experimental data with DLVO equations and the results are the parameters of the interaction. For example, the values of κ and ψ extracted from these fits are consistent with values obtained by other

experimental techniques [68, 75, 76]. The example of such a comparison measured by Ducker et al. [75] is shown in Figure 14b.

1.4 Computer Simulations of Colloidal Suspensions

The invention of the computer gave researchers a new tool for investigating a wide range of scientific problems. Besides experimental investigations or pure theoretical approaches a new branch of research emerged. Computer simulations are somehow in the middle between theory and experiment. In a purely theoretical work, a model is proposed and then the theoretician tries to solve it with only "paper and pencil" and of course a lot of knowledge of mathematics. In the case of computer simulations the same model can be used, but the problem is solved numerically. The solution of a theory is an analytical relation, *i.e.*, equation, which gives you the explanation how certain properties are connected. In contrast, the result of a simulation is only a numerical value, which has a statistical error like an experimental result. In this respect the simulations resemble experiments [77]. Simulations are used as computer experiments to test the quality of theories. Furthermore, they are used to investigate processes that are hard or impossible to measure experimentally or to predict experimental results.

Computer simulations are also widely used in the field of colloidal science, see the reviews [78, 79, 80]. The *Monte Carlo*, *Molecular Dynamics*, and *Brownian Dynamics* methods are typically used for simulations of colloidal systems [78, 79, 80].

In Molecular Dynamics (MD) the motion of the molecules in the system is simulated by solving *Newton's* equation of motion [77, 81]:

$$F(\vec{r}) = -\nabla U = m \cdot \frac{d^2\vec{r}}{dt^2}, \tag{1.22}$$

where $F(\vec{r})$ is the mean force exerted on the molecule produced by all other molecules, ∇U is the gradient of the potential, m is the mass of the molecule, and $\frac{d^2\vec{r}}{dt^2}$ is the acceleration. Using this method we can see the time evolution of the system and at every moment we can calculate its properties. Like in an experiment we measure a property of interest during certain time and calculate the time average. Every molecule is modeled explicitly and therefore it is hard to simulate systems with a large number of colloidal particles, because the number of molecules in the system would be too large to handle. MD is normally used in interface problems [82] or systems containing one colloidal particle immersed in a molecular medium [83].

A Brownian Dynamics (BD) simulation is a method related to a molecular dynamics simulation, where Newton's equation of motion is replaced with the *Langevin-type* equation [81, 84]:

$$m\frac{d^2\vec{r}}{dt^2} = F(t) - 6\pi\eta d \cdot \frac{d\vec{r}}{dt} + F^{int}(\vec{r}), \tag{1.23}$$

where $F(t)$ is the random Brownian force, η is the viscosity of the medium, d is the diameter of a spherical particle, and $F^{int}(\vec{r})$ is the particle-particle interaction force. The stochastic Brownian force has to fulfill two conditions, first the average of the force has to be zero, $\langle F(t)\rangle = 0$, and second the mean-square displacement of the particle due to this force is proportional to the diffusion coefficient. In BD the solvent is not modeled explicitly, its effect is accounted in random Brownian and viscous forces. In contrast to MD, BD makes it possible to simulate systems with large number of colloidal particles [58, 60].

The Monte Carlo (MC) method, which is used in this work, is presented in a separate section.

1.4.1 Monte Carlo Method

A property of a system that is dependent upon its microscopic state oscillates in time around a certain average value, see Figure 15. Let us consider the example of a gas in

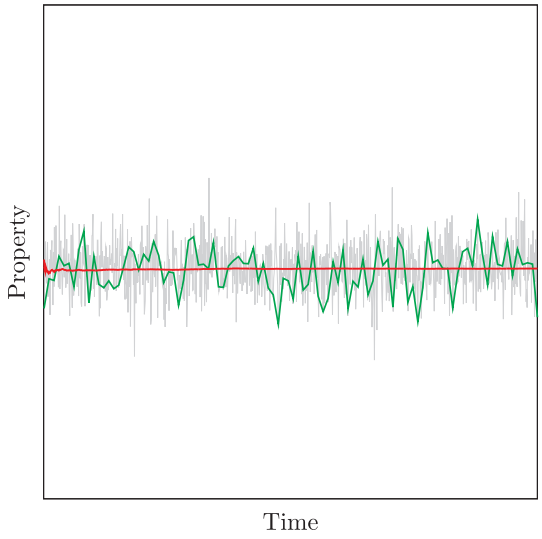

Figure 15: *The measured property is oscillating around the average value.* Every physical quantity of a system is oscillating in time. With the experimental technique the time average of the quantity is measured. The oscillations of the quantity are usually extremely small in comparison to the average value.

a closed container. If we take a microscopic snapshot of our system, we observe that at time t_1, N_1 molecules hit the wall of the container, exerting pressure on the walls. At the next moment, t_2, a slightly different number of molecules, N_2, hits the wall and the value of the pressure changes. Experimentally, we measure the average value of the pressure in the container, which is a consequence of the hits of the average number of molecules. Usually, the oscillation of pressure is extremely small and it is immeasurable. However, what we actually measure is the time-averaged value. If the system is ergodic the time average is equal to the *ensemble* average [77, 85]. This is the average of all states that are accessible to the system and the average is weighted with the probability of finding the system in a certain state, see Equation 1.24.

$$\langle O \rangle = \lim_{\tau \to \infty} \frac{1}{\tau} \int_0^\tau O(t)\, dt = \sum_j P(j) O(j)\,, \tag{1.24}$$

where $\langle O \rangle$ is the average value of a quantity O. The integral in the equation above gives us the time average of O in the time from 0 to τ and it is used for calculating the averages in the MD and BD simulations. The same average is calculated by a summation of the product $P(j)O(j)$ through all the possible microscopic states of the system, where $P(j)$ is the probability of finding a system in the state j and $O(j)$ is the value of the quantity O in this state. What we actually want to do is to calculate the macroscopic properties of the system by knowing the properties of the molecules/particles that build this system and the interactions between them.

The summation part of Equation 1.24 is the basis of the Monte Carlo simulation method. In the *canonical* ensemble, *i.e.*, a system with a constant number of particles,

N, constant volume, V, and constant temperature, T, the probability of finding the system in a certain state is a function of the energy of this state:

$$\langle O \rangle = \sum_j P(j)O(j) = \sum_j \frac{e^{-\frac{E(j)}{k_B T}}}{\sum_j e^{-\frac{E(j)}{k_B T}}} \cdot O(j)\,, \tag{1.25}$$

where $E(j)$ is the energy of the state j and $k_B T$ is the thermal energy. Using the Equation 1.25 we can calculate the canonical average of the properties of the system. In a simulation we start by randomly choosing the coordinates of all the particles in the system and build an initial state. We continue by calculating the energy of this state using the model to determine the particle-particle interaction energy. And then new state is formed and we repeat the procedure, see Figure 16. During this procedure

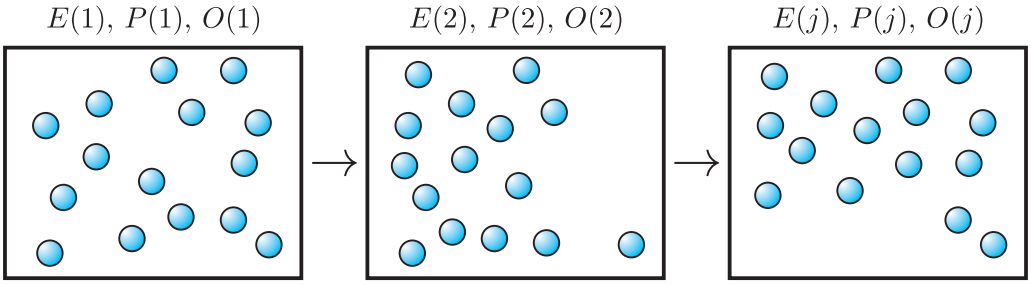

Figure 16: *Random formation of states for calculation of average properties.* Every state is formed randomly and energy and its properties are calculated. The average is calculated using equation 1.25.

we calculate the properties using Equation 1.25. However, typically most states of the system have a low probability and the product $P(j)O(j)$ is close to zero. Therefore in practical cases we would have to construct an immense number of states to get the true average of the quantity and such calculations are not feasible. The practical use of MC simulations was enabled by Metropolis and co-workers. They proposed the *Metropolis* method for the calculation of averages [86]. Their idea was based on the fact that states having a much higher energy than the average energy are not probable and therefore their contribution to the average properties can be neglected. They devised a procedure that explores only the states that have an energy close to the average energy. First we start with a random state, i. Then we choose a particle and randomly move it to get a new state, n, see Figure 17. Next, we calculate the energy change going from the initial

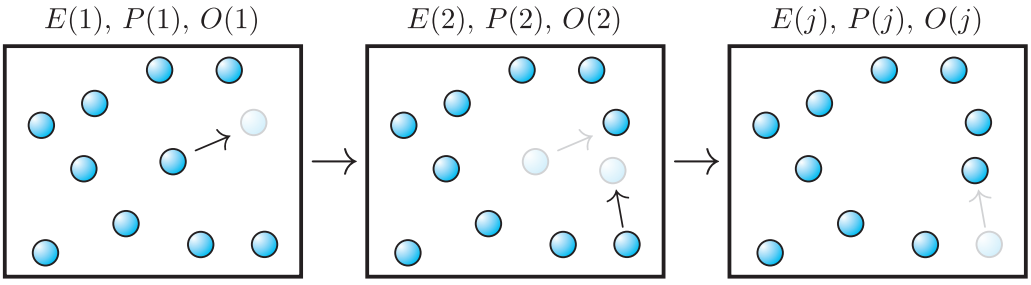

Figure 17: *Metropolis scheme for sampling configurational space.* By moving one particle at the time, we form a Markov chain of states. The properties are calculated as the average through these states, see Equation 1.28.

state to a new state:

$$\Delta E(i \to n) = E(n) - E(i)\,. \tag{1.26}$$

If the new state has a lower energy ($\Delta E < 0$), we accept the move. Otherwise, if the energy difference is positive ($\Delta E > 0$), we calculate the transition probability, $P(i \to n)$:

$$P(i \to n) = e^{-\frac{\Delta E(i \to n)}{k_B T}}\,, \tag{1.27}$$

and we chose a random number, ξ, from an interval $[0, 1]$. In the case when $P(i \to n) > \xi$ we accept the move, otherwise the move is rejected and the system is reverted to a state i. We form a *Markov* chain of states using the rules described above, where the acceptance/rejectance of a new state is chosen according to the previous state. With such a formation of a chain of states the average is calculated differently:

$$\langle O \rangle = \frac{1}{M} \sum_{j=1}^{M} O_j\,. \tag{1.28}$$

Here, we just sum up the values of O, when moving through the chain of states, and at the end the sum is divided by the number of steps in the chain, M. The authors described the method: "*Instead of choosing the configurations randomly, then weighing them with* $e^{-\frac{E}{k_B T}}$*, we choose configurations with a probability* $e^{-\frac{E}{k_B T}}$ *and weigh them evenly.*" By using the Metropolis scheme we force the system to be near the average and thus we are able to calculate the properties in a small enough number of steps that can be handled on a computer.

The pseudo-code for the main parts of the Metropolis MC method is given in Algorithm 1.

In practice we normally use a relatively small part of the whole system to simulate its behavior. Typically, we use from 100 to several 1000 particles. In small ensembles the choice of boundary conditions is important, because large part of the system is in contact with a boundary. For the simulation of a bulk suspension, we have to use a trick to create the appropriate boundaries. Using a cubic simulation box we can create periodic boundary conditions by multiplying the simulation cell, and create a situation where the system is in contact with itself. Typically, a minimum image convention is used in such case, see Figure 18. If a particle moves across the cell boundary out of the box, at the same time it comes back inside the box through a movement of its image from the adjacent box. Furthermore, by using the minimum image approximation, the particle is interacting with the closest image of the other particles in the box. The part of the pseudo-code implementing the periodic boundary conditions with minimum image convention is shown in Algorithm 2.

1.4.2 Analysis of the Results

Computer simulations offer detailed information about the system, some of which may not be easily accessible by experiment or theory. For example, in the simulation we know the coordinates of all of the particles at each simulation step. Therefore, we can track how the system evolves during the simulation run and we can calculate the total interaction energy of the configuration, *i.e.*, the configurational energy. The evolution of the energy shows when the system relaxes and the equilibrium is reached; therefore, this is one of the most important quantities to track.

Sometimes it is practical to visualize the microstructural evolution of the system. In the case of an unstable suspension, we can observe how the agglomerates form and what

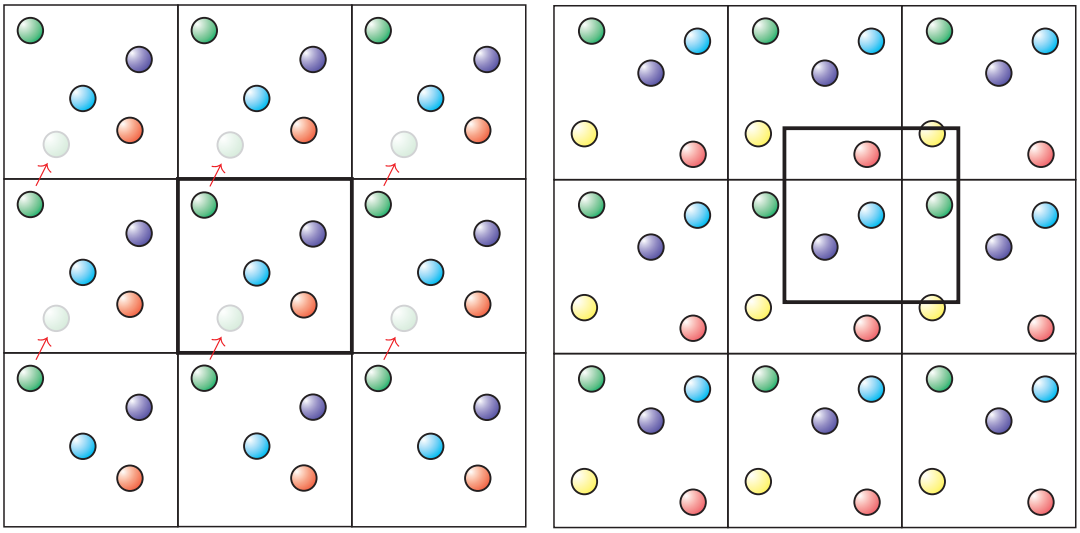

(a) Periodic boundary conditions (b) Minimum image convention

Figure 18: *Schematic presentation of the periodic boundary conditions with a minimum image convention.* (a) For the application of the periodic boundary conditions, the simulation box is multiplied around the central box. If a particle gets out of the central box at one side, at the same time its image enters the box from the other side. The images serve as boundaries for the particles in the central box. (b) If the minimum image convention is used, the particle interacts with other particles in the box or its nearest images. In both cases the scheme is presented for a 2D square cell. After [81].

their final structure is. Normally we use software that takes the particle coordinates as an input and creates 3D snapshots of the particles in the simulation box. These microstructural snapshots can be compared to the experimental microscopic images, see for example [57, 87, 88].

A quantitative description of the microstructure of the system can be given by the pair distribution functions. The definition of the pair distribution function is given by Equation [89]:

$$g(\mathbf{r}_1, \mathbf{r}_2) = \frac{N(N-1)}{\rho(\mathbf{r}_1)\rho(\mathbf{r}_1)Z_N} \int e^{-\frac{U(\mathbf{r}_1,\mathbf{r}_2,\ldots,\mathbf{r}_N)}{k_B T}} d\mathbf{r}_3 d\mathbf{r}_4 \cdots \mathbf{r}_N \,, \tag{1.29}$$

where N is the number of particles in the system, ρ is the density of the particles, Z_N is the *configurational* integral, U is the particle interaction energy, and $\mathbf{r}_i$ are coordinates of the particle i. This function gives the probability of finding the first particle at $\mathbf{r}_1$ and the second at $\mathbf{r}_2$, irrespective of the position of the remaining $N-2$ particles. If the system is homogeneous and isotropic the pair distribution function simplifies to the radial distribution function (RDF), $g_{ij}(r)$, which is connected with the probability of finding particles j at a distance r from the center the particle i. For the calculation of the radial distribution functions using ensemble averaging, the following equation is used [81]:

$$g_{ij}(r) = \frac{1}{\rho_j N_i} \sum_i \sum_{j \neq i} \langle \delta(r - r_{ij}) \rangle \,, \tag{1.30}$$

where ρ_j is the density of particles j, N_i is the number of particles i, r is the distance from the center of the particle i, r_{ij} is the distance between particle i and j, and

$\langle \delta(r - r_{ij}) \rangle$ is the averaged delta function. What the RDF is actually measuring is the density of the particles j at the distance r from the center of the particle i normalized by the average density of the particles j:

$$g_{ij}(r) = \frac{\rho_{ij}(r)}{\rho_j}\,, \tag{1.31}$$

where $\rho_{ij}(r)$ is the local concentration of particles j at the distance r from particle i. The scheme of the RDF calculation is presented in Figure 19, while the pseudo-code is shown in Algorithm 3. During simulations an RDF histogram is constructed. The values of

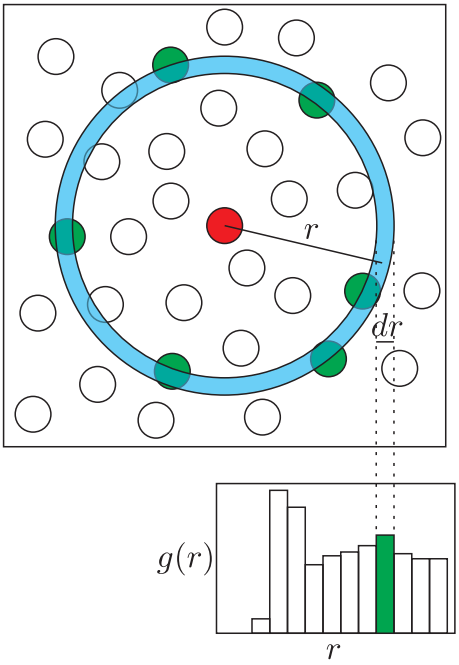

Figure 19: *Radial distribution function calculation scheme.* The density of the particles at distance r from the red particle in the area with the thickness dr is divided by the average density of the particles in the simulation cell. The result is the $g(r)$ histogram, which is usually averaged through simulation steps. The scheme is presented for the 2D simulation and it is easily extended to the 3D case. After [90].

the density of the particles at distance $r + dr$ from the central particle is divided by the average density of the particles in the box and assigned to the $g(r)$ histogram. The RDFs give us a quantitative description of the structure of the system. Furthermore, it can be used for the calculation of the radiation scattering patterns, which are measurable by experiment, see for example [91]. Thermodynamic properties like pressure, chemical potential, compressibility can be also calculated from RDFs [81, 89].

Algorithm 1: *Main part of the Monte Carlo method using the Metropolis scheme.* First we create a random initial state and calculate its energy. We continue with the main loop, where we move a random particle and calculate its interaction with all the others. Using the interaction energy we accept or reject the new state. During the loop we calculate the average properties of the system.

```
Loop i=1 to Npart                          //loop through all particles
   rx(i)=random()                          //create random coordinates
   ry(i)=random()
   rz(i)=random()
End Loop

Loop i=1 to Npart                          //loop for calculation of
   Loop j=i+1 to Npart                     // initial configuration energy
      Ei = interaction_energy(r(i),r(j))
   End Loop
End Loop

//MAIN LOOP
Loop n=1 to Nstep                          //loop through simulation steps
   r(i) = choose_particle(all)             //randomly choosing a particle
   rold(i) = r(i)

   Eold = interaction_energy(rold(i),all) //interaction energy of
                                            // particle i with all others

   rnew(i) = r(i) + drmax*random()         //random displacement of
                                           // particle i

   Enew = interaction_energy(rnew(i),all) //interaction energy of
                                            // particle i with all others
   dE = Enew - Eold

   if(exp(-dE/kT) > random())              //check the transition
      r(i) = rnew(i)                       // probability to accept/reject
      E = Ei + dE                          // current state
   else
      r(i) = rold(i)
   end if

   average_properties(i)                   //add state for average
                                           // properties calculation
End Loop
//END OF MAIN LOOP

// Npart - number of particles
// Nstep - number of the simulation steps
// rx, ry, rz - particle coordinates
// random() - function for choosing random numbers from [0,1]
// drmax - maximal displacement vector
// Eold, Enew - energy of the old/new state
```

Algorithm 2: *Implementation of periodic boundary conditions with minimum image convention.* Using the `anint()` function a particle that escapes out of the bounds of the cell is replaced by its image, which enters the cell on the other side. The same function is used for the implementation of a minimum image algorithm.

```
r(i) = r(i) + drmax*random()            //randomly move particle

r(i) = r(i) - lbox*anint(r(i)/lbox)     //pull it back into the box
                                        // if necessary

rij = r(i)-r(j)                         //vector between particles
                                        // i and j

rij = rij-lbox*anint(rij/lbox) // minimum image convention

// drmax - vector of maximal displacement
// random() - function for choosing random numbers from [0,1]
// r(i) - coordinates of particle i
// lbox - box length
// anint - function which rounds its element to the nearest whole number
```

Algorithm 3: *Pseudo-code for the $g(r)$ calculation.* During the simulation runs the inter-particle distances are calculated and they are distributed into RDF bins. A histogram `g(bin)` is constructed and then normalized.

```
Loop n=1 to Nstep                       //loop through simulation steps
   Loop i=1 to Ni                       //loop through i particles
      Loop j=1 to Nj                    //loop through j particles
         calculate rij                  //distance between i and j
         bin=Integer(rij/binLength)
         g(bin)=g(bin)+1                //make a rdf histogram
      End Loop
   End Loop
End Loop

Loop n=1 to maximal bin                 //loop for g(r) normalization
   g(n)=g(n)/(Nstep*Ni*Nj*Vbin(n)/Vcell)
End Loop

// Nstep - number of the simulation steps
// bin - bin number for the g(r) histogram
// binLength - length of the bin
// Vbin - volume of the spherical shell which corresponds to bin n
// Vcell - volume of the simulation cell
```

2

Aims and Hypothesis

PMN-based materials posssess interesting properties that are attractive for applications as well as for basic research, see Introduction. However, the synthesis of phase-pure PMN-based materials remains a challenge. Therefore, the main aim of this work is to develop a single-calcination synthesis method that would yield phase-pure perovskite PMN-based materials with good electrical properties.

As explained in the Introduction a homogeneous distribution of reagent powder particles in a mixture of PbO, Nb_2O_5 and MgO is not beneficial for the PMN synthesis, due to the preferential reaction between lead and magnesium oxide. According to the reactions 1.5-1.9 it is clear that the reaction between PbO and Nb_2O_5 must be avoided to prepare phase-pure PMN powder in a single-step, solid-state reaction.

Solid-state reactions are usually diffusion controlled (Figure 3); therefore, a contact surface, *i.e.*, the number of contacts between the species, controls the rates of the reactions. We have to avoid the contacts between the PbO and Nb_2O_5, to prevent or slow down the reaction between the two species. All three components PbO, Nb_2O_5, and $(MgCO_3)_4{\cdot}Mg(OH)_2{\cdot}4H_2O$, (MHC)[1], are present in the reaction mixture for a single-calcination synthesis of PMN. Two possible arrangements of the reagent particles for the PMN synthesis are schematically presented in Figure 20. In Figure 20a we can observe the arrangement where an unwanted reaction between PbO and Nb_2O_5 particles is enhanced due to the large number of PbO-Nb_2O_5 contacts. If we want to slow down or avoid this reaction, we have to prevent the contacts between the two species. Such an arrangement is presented in Figure 20b. The question is how to achieve the desired arrangement of the particles in the reactant mixture. Somehow, we need to find a way to manipulate the spatial distribution of the particles of the different reactant compounds. The proposed way is to use aqueous colloidal suspensions of reactant particles, as explained below.

By manipulating particle-particle interactions in suspensions, we can devise the formation of agglomerates with the desired structure. In two-component systems such an approach was used, for example, to control the sintering process [58, 92], to prevent the segregation of the two components during centrifugal consolidation [93], or to better control the synthesis of the mullite ceramics [63]. In these cases the designed hetero-agglomeration was used to achieve the formation of the desired structure of agglomerates.

[1]Note that $(MgCO_3)_4{\cdot}Mg(OH)_2{\cdot}4H_2O$ is used for the reaction instead of MgO. There are two reasons for usage of the MHC, first it exhibits appropriate electrokinetic properties and second MHC is more reactive in comparison to MgO.

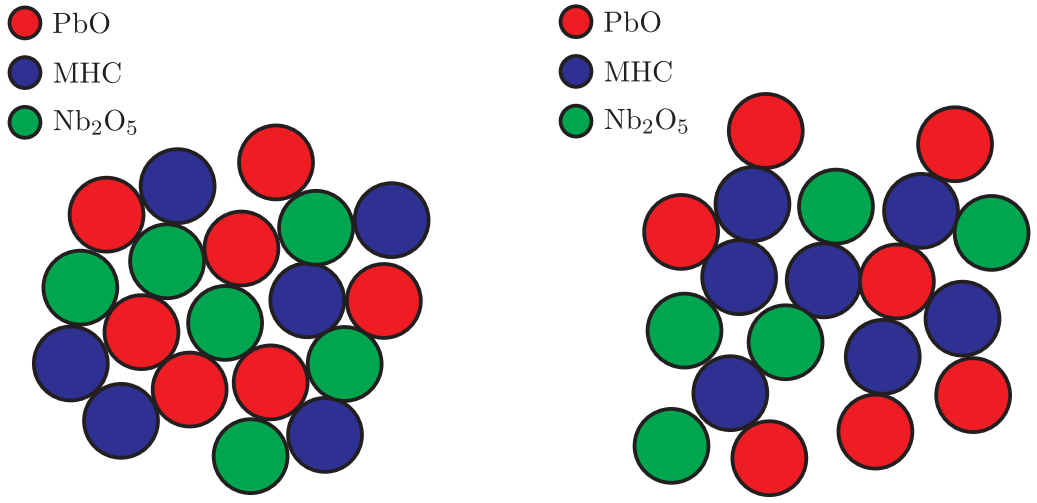

(a) A lot of red-green contacts

(b) No red-green contacts

Figure 20: *Schematic presentations of two possible arrangements of the reagent particles for the PMN synthesis.* (a) Arrangement with a lot of PbO-Nb_2O_5 contacts. Unwanted reaction between PbO and Nb_2O_5 is enhanced. (b) Magnesium compound separates PbO and Nb_2O_5, thus preventing them to be in contact. We slow down the unwanted reaction between PbO and Nb_2O_5. In both cases PbO is red, MHC blue and Nb_2O_5 green.

We want to apply a similar concept and prepare the designed structure of agglomerates of the reactant particles that will be used as a reactant mixture for the solid-state synthesis. In contrast to the examples presented above, we use a three component system. One way of controlling the interactions between particles is through electrostatic forces by controlling the surface charge of the particles. In the case of oxide systems the surface charge can be regulated by pH - see Equations 1.16 and 1.17. This is observed experimentally with the dependence of zeta-potential on the pH. By manipulating the inter-particle forces with controlling the surface charge of the particles we can devise the formation of agglomerates and possibly create such an agglomeration process that would result in the desired type of contacts, like the ones shown in Figure 20b. We assume that the same spatial distributions of the particles will remain in the dried reactant powder mixtures.

By choosing the appropriate pH conditions self-assembled agglomerates with the desired arrangement of particles should form. Our preliminary results from zeta-potential measurements show that at pH values below 11.8 PbO and MHC are positively charged, while Nb_2O_5 is negatively charged. Above pH = 11.8 the situation is different, now only the MHC is positively charged, while the PbO and Nb_2O_5 are negatively charged. Therefore, we expect different electrostatic interactions between the particles in two situations and hence the structures of the formed agglomerates should be different. In the first case an electrostatic attraction between the PbO and Nb_2O_5 is expected, while in the second case the two components should repel each other.

According to DLVO theory, the pair potentials consist of electrostatic and van der Waals interactions. Hence, the agglomerates are formed in a competition between the attractive and the repulsive interactions. Moreover, in the multicomponent systems a

combination of the direct and indirect interactions, stemming from other particles in the suspension, affects the process, making the prediction of the assembly even more complicated. In a study of agglomeration processes with colloidal-cluster formation, Monte Carlo simulations are efficient in terms of performance. The results reported in recent studies by MC simulations are shown to be in agreement with experimental findings and theoretical predictions [61, 88, 94, 95, 96]. In this work we use the MC simulations to study the mechanism of agglomeration in our three-component system of charged colloidal particles, which are used for the PMN synthesis. Our main focus is on the structure of the various types of precursor clusters that may form at different pH conditions. The parameters of the interaction potentials and the particle sizes are taken to closely correspond to the different experimental situations.

In the second part of the work we try to prepare a phase-pure PMN powder in a single-calcination step. The choice of the experimental conditions is based on the results from the simulations. Furthermore, we study the properties of the powders with respect to the different experimental conditions applied. The powders are used for the preparation of the ceramics and their dielectric and electrostrictive properties are analyzed.

In the last part we apply the same concept to the synthesis of 0.65PMN-0.35PT. Like in the previous case, the properties of the powders and ceramics prepared at different pH conditions are compared.

3

Materials and Methods

This Chapter describes the materials and methods used in this work. We begin with a presentation of the method and the model used in the computational description of our system. Next, we discuss the analysis of the simulation results. The second part deals with the experimental system, its preparation, and a characterization of the properties of the suspensions, powders and ceramics.

3.1 Computational Model & Method

3.1.1 Model & Parameters

We consider the model of the interacting charged colloidal particles within a suitable potential and the parameters selected such that they match closely the experimental system. A three-component system is used in the simulations, representing three types of charged particles in the experiment, PbO, $(MgCO_3)_4{\cdot}Mg(OH)_2{\cdot}4H_2O$, (MHC), and Nb_2O_5. As explained in detail below, the model parameters are either extracted from the experiment or otherwise taken from the literature to closely mimic the experimental conditions.

The coarse-grained model is employed. The particles in the suspensions are assumed to be charged, hard spheres in a continuous medium. The water molecules and the ion species in the suspension are not modeled explicitly, only their average contribution to the colloid-colloid interactions is taken into account. As mentioned in the introduction, the DLVO [73, 74] potential is suitable for modeling the interactions in these systems. According to the theory, the pair potential U_{ij}^{DLVO} between the colloidal particles i and j is composed of the electrostatic contribution, U_{ij}^{el}, and the van der Waals contribution, U_{ij}^{vdW}. In our case the hard-core interaction, U_{ij}^{hc}, is added to prevent the overlapping of the particles. For each pair (ij) of reagent particles we have:

$$U_{ij}^{\mathrm{DLVO}} = U_{ij}^{\mathrm{vdW}} + U_{ij}^{el} + U_{ij}^{hc}\,. \tag{3.1}$$

For the van der Waals interaction the following expression for spherical particles is used [56]:

$$U(r_{ij}) = -\frac{A_{ij}}{6}\cdot\left[\frac{2a_ia_j}{r_{ij}^2-(a_i+a_j)^2}+\frac{2a_ia_j}{r_{ij}^2-(a_i-a_j)^2}\cdot\ln\left(\frac{r_{ij}^2-(a_i+a_j)^2}{r_{ij}^2-(a_i-a_j)^2}\right)\right], \tag{3.2}$$

where A_{ij} is the Hamaker constant, r_{ij} is the center-to-center distance, and a_i and a_j are the radii of the interacting particles. The typical values of the Hamaker constants in

the case of particles of inorganic materials interacting through water are in the range of $1 \cdot 10^{-21}$ J to $1 \cdot 10^{-19}$ J [97]. However, we did not find in the literature the exact values of A_{ij} for the materials used in our experiments, *i.e.*, PbO, Nb_2O_5, MHC; therefore, all the Hamaker constants in our simulations are chosen to be equal to $A = 3 \cdot 10^{-20}$ J.

The Hogg-Healy-Furstenau (HHF) equation is used to calculate of the electrostatic interactions [71]:

$$U_{ij}^{el} = \pi \varepsilon_r \varepsilon_0 \cdot \frac{a_i a_j}{a_i + a_j} \left[(\psi_i + \psi_j)^2 \ln\left(1 + e^{-\kappa h}\right) + (\psi_i - \psi_j)^2 \ln\left(1 - e^{-\kappa h}\right) \right], \quad (3.3)$$

where $h = r_{ij} - (a_i + a_j)$ is the surface-to-surface distance between the particles, $\varepsilon_r \varepsilon_0$ is the dielectric permittivity of the medium, ψ_i is the electrostatic surface potential of the particle i, and κ is the inverse Debye screening length. For the dielectric constant, the value for water $\varepsilon_r = 78.5$ is used. The electrostatic surface potential values are taken to be equal to the measured zeta-potentials. The values for the Debye screening length are calculated from the estimated ion concentrations. Because relatively high pH = 11.4 and 12.5 values are used in our experiment, assuming that the major contribution to the ion concentration comes from the OH^- ions and their counter-ions is reasonable. Therefore the ion concentration can be estimated from the pH. The ionic strength $I = \sum_i c_i z_i$ is calculated from the ion concentration c_i, and z_i is the charge number of the ion. The Debye length, which is used in the simulations, is then calculated as:

$$\kappa = \sqrt{\frac{2 N_A e^2 I}{\varepsilon_0 \varepsilon_r k T}} = 1.6 \cdot 10^8 \mathrm{m}^{-1}, \quad (3.4)$$

where N_A is the Avogadro number, e the elementary charge, and I is the ionic strength.

The third term in the equation (3.1) describes the hard-core interaction. In this case the interaction energy is zero for non-overlapping particles and infinite for distances where the particles would overlap:

$$U_{ij}^{hc} = \begin{cases} \infty; & r_{ij} \leq \frac{a_i + a_j}{2} \\ 0; & r_{ij} > \frac{a_i + a_j}{2} \end{cases}. \quad (3.5)$$

The cutoff distance for all the potentials is equal to $r_{\mathrm{cutoff}} = 2.2(a_i + a_j)$. At this distance the interaction energy is practically zero.

3.1.2 Monte Carlo Simulation method

To simulate the aggregation processes with these three types of charged particles in the aqueous suspension we use the three-dimensional off-lattice Monte Carlo technique at finite temperature [77, 81, 98]. The canonical ensemble with the fixed number of particles N, volume V, and temperature T is used. The temperature is fixed to $T = 293$ K and the total number of particles in the simulation cell is 100 in all cases, except in the case of the larger MHC particles, where 200 particles are used. The cubic simulation cell with the periodic boundary conditions and the minimum image convention are employed [81]. The volume of the simulation cell is calculated from the volume concentrations (ϕ) of the particles and the number of the particles in the simulation cell. In all the simulations we keep the concentrations of the particles the same as in the experiments, *i.e.*, $\phi_{\mathrm{PbO}} = 1.6$ vol.%, $\phi_{\mathrm{Nb_2O_5}} = 1.2$ vol.%, and $\phi_{\mathrm{MHC}} = 1.0$ vol.% , respectively.

Within the MC technique, the aggregation process, in which the interacting particles diffuse towards energetically stable positions, is considered in the configurational space.

The starting configuration of the particles is chosen randomly with the condition that their mutual distances are larger than $r_{ij} = 1.2(a_i + a_j)$, where the interaction energy is almost zero. Then at each MC step a random particle is chosen and moved to a new position by a small random displacement Δr, which is chosen from the $[0, \Delta r_{max}]$ interval using uniform random numbers. The difference in the energy of the system on-going from one state to another state, ΔE, is calculated via the expressions in Equations (3.1, 3.2, 3.3, 3.5) summed over all the pairs of particles. The attempted move is accepted if the transition probability

$$P = e^{\frac{-\Delta E}{kT}} \geq \eta \ , \tag{3.6}$$

exceeds a random number $\eta \in [0, 1]$, otherwise the new configuration is rejected. Then another particle is selected randomly and attempted to move, and so on. These steps are cycled until the system reaches equilibrium. The pseudo-code is shown in Algorithm 1.

To validate the results, test simulations with a larger number of particles are carried out. To check the reproducibility of the equilibrium states, the simulations with the same parameters but a different initial configuration of the particles are carried out. Reproducible results are obtained. In each case the actual number of the Monte Carlo steps is $N_{step} = 2 \cdot 10^9$. Note that such a large number of steps is needed to reach equilibrium because small displacements $\Delta r_{max} = 1$ nm need to be applied, in view of the small range of DLVO potentials. Large steps Δr can lead to jumps over the potential maximum and hence to physically meaningless results. The maximum displacements used in the simulations are below 0.04 % of a cell length, $\Delta r < 0.0004 \cdot \ell_{\text{cell}}$. To mimic the experimental situation we also keep the room temperature throughout the simulations. In this way we allow a particle, which is already bound to a cluster, to drift away due to favorable thermal fluctuations. The attractive interaction potentials are very steep when the particles are close to each other, resulting in large negative energies in comparison to k_bT. Therefore, in most cases the cluster fragmentation is not energetically favorable. On the other hand, the clusters themselves are not fixed in space. They evolve through the individual particle dynamics, *i.e.*, addition or detachment of the particles, and their centers of mass move. For the objectives of this work explained in Aims and Hypothesis, we are mainly focused to the inner structure of these clusters.

3.1.3 Analysis of the Computational Results

Simulation-Cell Snapshots

The coordinates of the particles are tracked during the simulation runs. For the generation of the perspective 3D views of the particles in the simulation box the Visual Molecuar Dynamics (VMD) program [99] is used. It is available at `http://www.ks.uiuc.edu/Research/vmd/`.

Radial Distribution Functions

For the calculation of the radial distribution functions (RDFs), $g_{ij}(r)$, Equation 1.30 is used. In practice the RDF histogram is constructed, see Figure 19. For each bin the value of RDF is calculated from the inter-particle distances. The RDFs are calculated during the simulation runs, as presented in Algorithm 3.

Analysis of the Contacts

In addition to the RDFs, the contacts the between different types of particles and their evolution during the simulations are analyzed. We count how many j particles are, on

average, in contact with one particle i. We consider that two particles are in contact when:

$$r_{ij} \leq \frac{d_i + d_j}{2} \cdot 1.05\,, \tag{3.7}$$

where r_{ij} is the inter-particle distance, and d_i is the diameter of particle i. In simulations we use three types of particles; therefore, a total of six types of contacts are possible. For example, a-a, b-b, c-c, a-b, a-c, and b-c contacts are possible in the ensemble of particles a, b, and c. For a representation of the contacts we are utilizing a 3×3 matrix of contacts, as presented in Figure 21.

c	$\frac{c_{ac}}{N_a}$	$\frac{c_{bc}}{N_b}$	$\frac{c_{cc}}{N_c}$
b	$\frac{c_{ab}}{N_a}$	$\frac{c_{bb}}{N_b}$	$\frac{c_{cb}}{N_c}$
a	$\frac{c_{aa}}{N_a}$	$\frac{c_{ba}}{N_b}$	$\frac{c_{ca}}{N_c}$
	a	b	c

Figure 21: *Matrix of contacts.* In the matrix all possible contacts between three types of particles, *i.e.*, a, b, and c are presented. Each cell gives the number of contacts, c_{ij}, normalized per number of particles in the columns, N_i.

3.2 Experimental

3.2.1 Sample Preparation

PMN

Aqueous suspensions of PbO (99.9 %), $(MgCO_3)_4{\cdot}Mg(OH)_2{\cdot}4H_2O$ (41.91 % of MgO, determined by a thermogravimetric analysis), and Nb_2O_5 (99.9 %) powders are prepared containing 20 wt.% of solids load in total. All the powders were purchased from Sigma Aldrich, St. Louis, USA. The powders were mixed in a molar ratio corresponding to the stoichiometry of PMN. Three sets of experiments are performed: (*i*) suspensions with starting pH = 11.4, the inherent pH of the suspension, and (*ii*) suspensions with starting pH = 12.5, adjusted by the aqueous ammonia solution (25 wt.%, Merck KGaA, Darmstadt, Germany), and (*iii*) suspension with starting pH = 10.0, adjusted by the formic acid (pro analysis, 98-100 %, Kemika, Zagreb, Croatia). The suspension with 20 wt.% of solids is also prepared in acetone (99.8 % , Carlo Erba Reagenti, Rodano, Italy). All the suspensions are milled in an attrition mill for 3 h with 800 rpm, using 3 mm yttria-stabilized zirconia balls (YSZ), and subsequently dried at 100 °C (aqueous suspensions) or at 50 °C (acetone suspension). The dried powders are heated in a chamber furnace with a heating rate of 2 K/min to the preset temperature and held at this temperature for 5 h. During this step the solid-state reaction takes place.

The powders calcined at 900 °C for 5 h are isostatically pressed into compacts at 300 MPa and sintered for 2 h at 950 °C, 1000 °C, and 1050 °C in a closed alumina crucible on a platinum foil. Powder with the same composition is placed around the samples to minimize the lead loss.

Separately the aqueous suspensions of the as-received PbO, Nb_2O_5, and $(MgCO_3)_4{\cdot}Mg(OH)_2{\cdot}4H_2O$ powders (20 wt.%) are prepared. The pH values of the suspensions were preset to 10.0 and 12.5. The suspensions are milled in an attrition mill for three hours, and dried at 100 °C .

PMN-PT

The procedure for the preparation of PMN-PT is analogous to the one used for PMN, except that in addition to PbO, $(MgCO_3)_4{\cdot}Mg(OH)_2{\cdot}4H_2O$, and Nb_2O_5, TiO_2 (rutile, 99.8 %, Alfa Aesar, Karlsruhe, Germany) is added to the powder mixture in a molar ratio corresponding to the stoichiometry of 0.65PMN-0.35PT. The mixture is suspended in water yielding a suspension with 20 wt.% of solid load in total. Here only two sets of experiments are prepared, the first one with the inherent pH, which corresponds to pH = 11.4, and the second one with the starting pH = 12.5 adjusted with the ammonia solution (25 wt.% of NH_3, Merck KGaA, Darmstadt, Germany). Both suspensions are homogenized in an attrition mill under the same conditions as used for PMN, and dried at 100 °C. The dried mixtures are heated in a chamber furnace with a heating rate of 2 K/min to the preset temperature and held at this temperature for 5 h.

The samples calcined at 850 °C for 5 h are isostatically pressed into pellets at 300 MPa. The pellets are sintered on a platinum foil in a closed alumina crucible at 950, 1000, and 1150 °C for 2 h. Powder with the same composition is placed around the samples to minimize the lead loss.

The characteristics of the starting powders used for the PMN and PMN-PT synthesis are collected in Table 2, including the data on their average particle size.

Table 2: *Characteristics of the starting powders.*

Chemical	Purity[A] [%]	Particle Size ($d_{mean,\,A}$) [μm]
PbO	99.9	3.0
$(MgCO_3)_4{\cdot}Mg(OH)_2 \cdot x H_2O$	41.91[B]	12.0
Nb_2O_5	99.9	0.5
TiO_2	99.8	0.4

[A] Producer's specification.

[B] Content of MgO in $Mg(OH)_2{\cdot}\ 4MgCO_3{\cdot}$ x H_2O powder determined by thermogravimetric-analysis was 41.91 %, thus, x is equal to 4.70

3.2.2 Characterization

Zeta-Potential Measurements

The zeta-potentials of the reagent powders are measured as a function of the suspension pH with a zeta-potential analyzer (BI Zeta PALS MAS Instrument, Brookhaven Instruments Corp.). This instrument measures the zeta-potential using an electrophoretic light-scattering technique. The samples are prepared in deionized water and the concentration of the powders is kept at 0.05 wt.%. The pH adjustment is achieved by adding either HCl or NaOH dilute solutions. We observed that the pH adjustment with ammonia yielded the same results. The pH of the suspensions was measured with an

Inlab 410 instrument (Mettler Toledo), calibrated with buffer solutions of pH 4.7 and 9.2.

Particle Size

The sizes of the particles in the powders are determined by a light-scattering method using the Microtrac S3500 Series Particle Size Analyzer instrument. All the powders are suspended in isopropanol. The results are derived from the area particle size distributions (PSD). In this case the mean particle diameter is defined as:

$$d_{mean,\,A} = \frac{\sum_i d_i^3 N_i}{\sum_i d_i^2 N_i}\,, \tag{3.8}$$

where d_i is the particle diameter of the $i-th$ size range and N_i is the number of particles in this size range. Additionally $d_{90,\,A}$, $d_{50,\,A}$, and $d_{10,\,A}$ values are used to describe the sample. The sum of the area of all the particles smaller than $d_{90,\,A}$ accounts for 90 % of the area of all the particles in the distribution. In analogous way, the sum of the area of all the particles smaller than $d_{50,\,A}$ and $d_{10,\,A}$ accounts for 50 % and 10 % of the area of all the particles in the distribution, respectively.

X–ray Diffraction Analysis

X-ray powder-diffraction (XRD) data of the as-dried and calcined powders, and the sintered samples, are collected at room temperature by a PANalytical X'Pert PRO MPD diffractometer using Cu–Kα_1 radiation in the 2θ range from 10 to 70 degrees in steps of 0.034 °, with an integration time of 6 seconds per step. The ceramics are crushed to powder in an agate mortar before measuring. The peak positions and their relative intensities are determined from the experimental patterns. The phases present are identified using the JCPDS database [100]. The Powder Diffraction File (PDF) numbers are given to define the matching patterns. The cell parameters of the pyrochlore and perovskite phases are calculated. Jana2006 software[101], which performs a full-pattern matching using the Rietveld method, is used.

Thermal Analysis

The thermogravimetric analysis (TGA) of dried powder mixtures is performed using a NETZSCH STA 409 analyzer. The samples of about 50 mg of dried powders are heated to 750 °C with a heating rate of 2 K/min in air and in argon.

Electron Microscopy

The microstructures of the powders and the ceramics are examined using two scanning electron microscopes, *i.e.*, FE-SEM SUPRA 35 VP (Carl Zeiss) for the powders and a SEM JSM-5800 (JEOL) for the ceramics. The powders are dispersed in isopropanol using an ultrasonic bath, then a few drops of suspension are spread and dried on highly oriented pyrolytic graphite substrates (SPI Supplies). The ceramics are cut and polished using standard metallographic techniques. In the case of the PMN-PT the samples are also thermally etched at 900 °C. Before any analysis in the microscope the samples are coated with a thin layer of carbon to achieve electrical conductivity and to avoid charging.

The structure of the powder is further examined with a transmission electron microscope JEM – 2100 (JEOL). The powders are ultrasonically dispersed in isopropanol and placed on a lacy, carbon-coated, nickel grid.

Density Measurements

The density of the ceramics is determined from the dimensions and masses of the pellets. The densities are usually expressed as a percentage of the theoretical density (TD). In the case of $Pb(Mg_{1/3}Nb_{2/3})O_3$ the TD equals 8.13 g/cm^3, as reported in [100]. For $0.65Pb(Mg_{1/3}Nb_{2/3})O_3$–$0.35PbTiO_3$ the theoretical density is calculated from the volume of the unit-cell, obtained from XRD, using the stoichiometric composition. The same value as for the PMN is obtained, *i.e.*, 8.13 g/cm^3.

Electrical Measurements (ε_r, P–E, S–E)

For the electrical measurements the ceramic samples are sliced to a thickness of $\sim$ 0.5 mm. The chromium-gold electrodes with a diameter of 5 mm are deposited with magnetron sputtering.

The capacitance, C, and dielectric losses, $\tan\delta$, are measured with a HP 4192A LCR meter (Yokogawa Hewlett-Packard) in the frequency range of 1–100 kHz. The relative dielectric permittivity, ε_r, calculated from the capacitance, is determined as a function of temperature in the range from -100°C to 300 °C. The lower part of the temperature dependence, *i.e.*, -100 °C to 70 °C, is measured on a low-temperature microprobe system (MMR Technologies), whereas the higher part, 25 °C to 300 °C, is measured in a tube furnace. The data are collected during cooling.

The polarization, P, as a function of electric field, E, is measured using an aixPES setup (aixACCT Systems). On the same system the interferometer method is applied for measuring the strain, S. A bipolar, single-sine, input wave is used for measuring P and S vs. E.

In the case of PMN-PT samples the piezoelectric coefficient, d_{33}, is also measured. The samples are poled in silicon oil with a DC electric field of 3 kV/mm at 160 °C for 5 min and then cooled in the same bias field (field cooling). After poling the samples are aged for 24 h. Then piezoelectric coefficient is measured using a Berlincourt piezometer (Take Control PM10).

4

Mechanism of Agglomeration in Suspensions for PMN Synthesis

A Computer Simulations Study

In this Chapter we use Monte Carlo simulations to get an insight into the microscopical structure of our suspensions. We investigate how agglomerates are formed in the suspensions for PMN synthesis under different experimental conditions. Two pH conditions, where we expect markedly different structure of agglomerates, are considered in the numerical simulations. First we simulate the system with particles of equal sizes, while in the second part the particle size effects are studied. In the last part we analyze the contacts between the reagent particles in the agglomerates. This result is important in the view of our experimental work, because it influences the solid-state reactions.

4.1 Experimental Framework

Our idea of using particle-particle interactions to control the spatial distribution of reagent particles is presented in the Aims and Hypothesis. Here we try to explore the formation of agglomerates in the suspension using realistic potentials by means of the Monte Carlo simulation method. By changing the suspension pH, the surface charge of the colloidal particles is altered and consequently the electrostatic interactions between the particles are changed. Experimentally, we measure the zeta-potential of the reagent particles in aqueous suspensions, see Figure 22. The zeta-potential is measured for three types of particles, *i.e.*, PbO, Nb_2O_5, and MHC. Detailed information about the electrokinetic properties of the considered powders will be given in a Chapter 5. Two pH conditions, where we expect markedly different structure of agglomerates, are considered: (*i*) pH = 11.4[1], and (*ii*) pH = 12.5. The two cases are subsequently denoted as the pH11.4 and pH12.5 samples. In the first case the zeta-potentials of PbO and Nb_2O_5 have opposite signs, while in the latter case they are both negative. At pH = 11.4, $\zeta_{PbO} = +40$ mV and $\zeta_{Nb_2O_5} = -80$ mV, thus due to the opposite sign of the ζ potentials, the electrostatic attraction between PbO and Nb_2O_5 is expected, while $\zeta_{MHC} = +10$ mV. At pH = 12.5, on the other hand, $\zeta_{PbO} = -50$ mV, $\zeta_{Nb_2O_5} = -100$ mV and $\zeta_{MHC} = +20$ mV, now a repulsive electrostatic interaction is expected between the PbO and Nb_2O_5, and an attractive interaction between the PbO and MHC, and

[1] pH 11.4 is the inherent pH of the suspension of the reagent powder mixture used in experiments

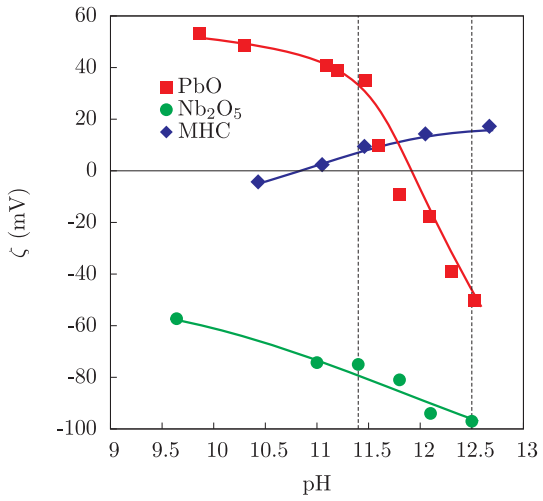

Figure 22: *Dependence of the zeta-potential on the pH.* Measured zeta–potentials of PbO, Nb_2O_5 and MHC particles as a function of the suspension pH. The two pH conditions considered in simulations are denoted by dashed lines.

Nb_2O_5 and MHC, respectively. Based on the zeta-potential measurements we propose the following hypothesis. The electrostatic interactions in the suspension with pH = 11.4 should promote the formation of clusters with contacts between the PbO and Nb_2O_5 particles, as schematically presented in Figure 20a. In contrast, at pH = 12.5 colloid-colloid interactions may lead to clusters in which the contacts between the PbO and Nb_2O_5 particles do not occur, while the MHC particles are interacting with both PbO and Nb_2O_5 particles, shown in Figure 20b. We propose that the structure of the as-formed colloidal assemblies, that occur at different pH suspensions, has a key influence on the solid-state reactions. We assume that the same spatial distributions of the particles remain in the dried powders.

We use DLVO theory for the calculation of the particle-particle interactions, which is explained in detail in Materials and Methods. The sizes of the particles used in the simulations are taken to be equal to the average diameter, $d_{mean,\,A}$, measured in the mixture of the reagent particles. The particle size distributions in both samples are narrow with similar $d_{mean,\,A}$ equal to 0.42 μm and 0.40 μm for pH11.4 and pH12.5 samples, respectively. The measured sizes are in good agreement with the FE-SEM results, see Figure 23. The particle sizes are used as input parameters for the simulations. Notice that the particle sizes are measured in the suspension mixture of the PbO, Nb_2O_5, and MHC particles; therefore, within the experimental procedure we cannot distinguish between the sizes of different types of particles. In principle, the sizes of each type of particles can be measured by separate milling of their powders. However, this may lead to different results, due to the changed conditions to which the particles are exposed, compared to the conditions when the mixture is milled, as in the experiment. However, in the simulations we consider both situations, first we choose the sizes of all particles to be equal to 400 nm, and in the second part we address the particle size effects, where we vary the size of MHC particles, which may affect the assembly processes the most.

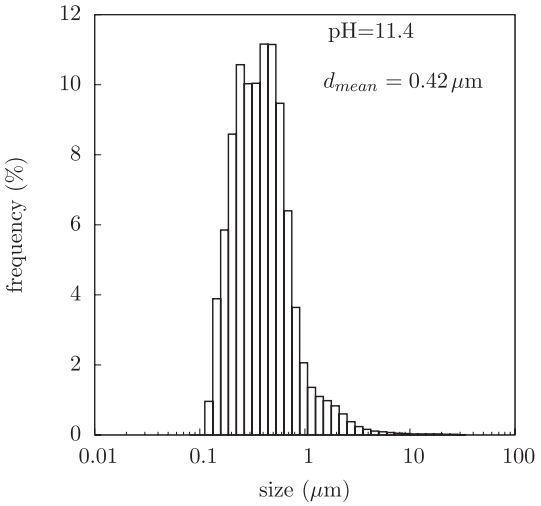

(a) PSD pH = 11.4

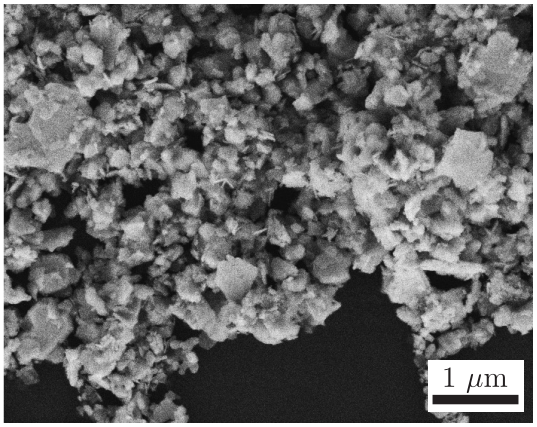

(b) FE-SEM pH = 11.4

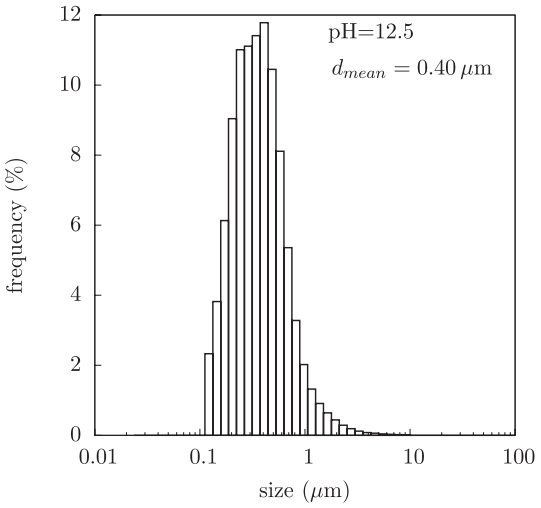

(c) PSD pH = 12.5

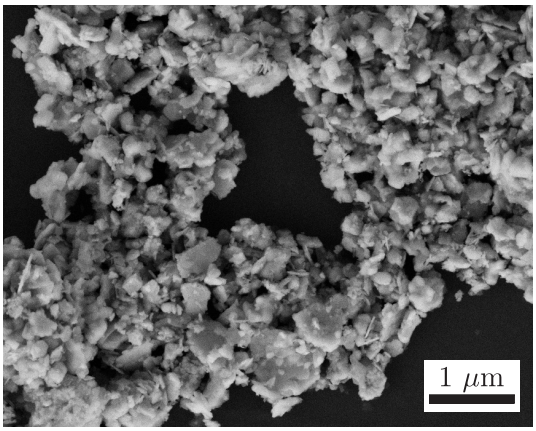

(d) FE-SEM pH = 12.5

Figure 23: *PSDs and FE-SEMs of the PbO, Nb_2O_5, MHC powder mixtures after milling.* (a) and (b) Particle size distribution and FE-SEM micrograph for the reagent powder mixture prepared at pH = 11.4. (c) and (d) Particle size distribution and FE-SEM micrograph for the reagent powder mixture prepared at pH = 12.5.

4.2 Test Simulation Runs

We use a total of 100 particles in our computational experiments. First, we test whether the size of the system is large enough to obtain representative results. We make simulations with 76 and 152 particles in total, the volume fractions of the particles is constant in all cases. The results of the two runs are compared in Figure 24. The total interaction energy of the two systems relaxes to the same value. The relaxation is faster in the smaller system, because the amount of attempted moves per particle is lower in the bigger system, and hence in the latter more steps are needed to reach equilibrium.

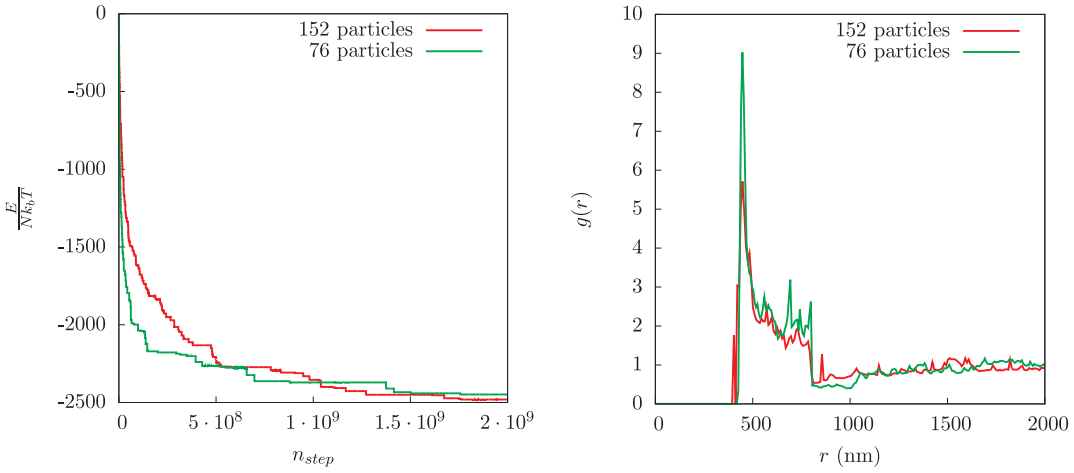

(a) Energy vs MC step (b) Radial distribution functions

Figure 24: *System size check.* (a) Dependance of the energy on the MC simulation steps for systems with 76 and 152 particles. (b) PbO-PbO radial distribution fuctions for these two systems.

The radial distribution functions confirm that the two simulation runs yield basically the same results.

To test the repeatability of the runs, several simulations are carried out with the same parameters, but with different initial configurations of the particles. In Figure 25 we compare the total interaction energies and radial distribution functions for the three

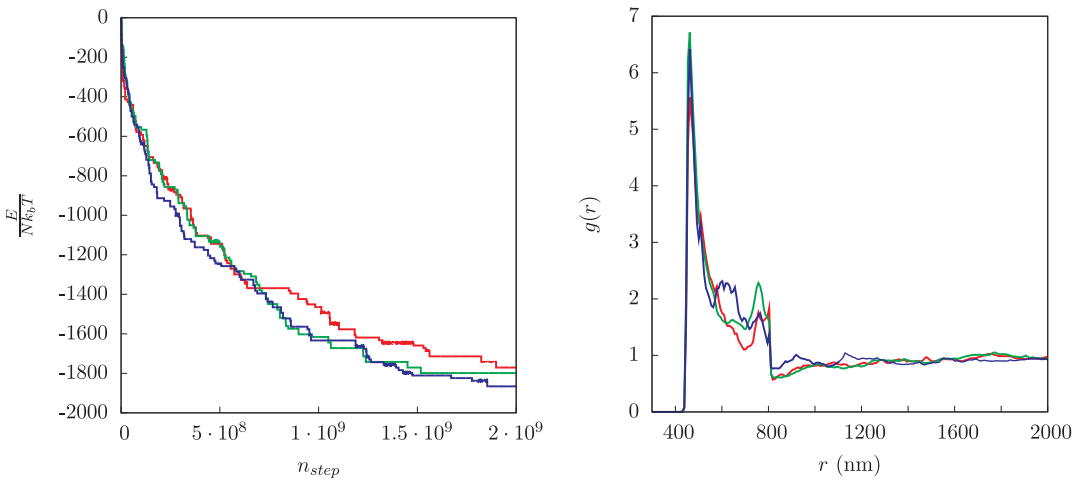

(a) Energy vs MC step (b) Radial distribution functions

Figure 25: *Repeatability check.* (a) Dependance of the energy on the MC simulation steps for three systems with the same parameters but different initial configurations. (b) PbO-Nb_2O_5 radial distribution fuctions for these three systems.

runs. The results show that the three different initial configurations relax towards the same equilibrium.

4.3 Emergent Clusters in the Suspensions for PMN Synthesis

In this section we present the results of the cluster formation in our three-component system. For a comparison of the two samples, representing the pH = 11.4 and pH = 12.5 suspensions, the simulation results are systematically plotted side by side. Here, we are mainly focused on the radial distribution functions and equilibrium distributions of the particles in the simulation box. These results show the microscopic structure of the system under different conditions.

4.3.1 Reagent particles of equal size

We first perform simulations assuming that all three types of particles have equal sizes. The diameter of the reagent particles is taken as 400 nm, which corresponds to the average size of the particle mixture in the suspension, measured with the static light scattering in both pH11.4 and pH12.5 samples. The set of all the parameters used for the calculations is given in Table 3. The effects of different sizes of the reacting particles

Table 3: *Parameters of the interaction potential for reagent particles of equal size.* All the parameters used for the calculation of the particle-particle interaction potentials in the case of equal-sized particles are given in this table.

pH	a_{PbO}, $a_{\mathrm{Nb_2O_5}}$, a_{MHC} [nm]	ψ_{PbO} [mV]	$\psi_{\mathrm{Nb_2O_5}}$ [mV]	ψ_{MHC} [mV]	A_{ij} [J]	κ [m^{-1}]
11.4	200	40	−80	10	$3 \cdot 10^{-20}$	$1.6 \cdot 10^{8}$
12.5	200	−50	−100	20	$3 \cdot 10^{-20}$	$1.6 \cdot 10^{8}$

are considered in the following section.

In Figures 26a and 26b the computed interaction potentials, using equations 3.2 and 3.3, for the pH11.4 and pH12.5 samples are shown, respectively. Six different pair interactions are present in the three-component system. All the interactions are short-ranged as they decay to zero already at around 450 nm, while the contact distance of the particles is 400 nm. In the case of pH = 11.4, the interactions between PbO-PbO, Nb_2O_5-Nb_2O_5, and PbO-MHC are repulsive, with the PbO-MHC interaction reaching a maximum of only 5 k_bT. These pairs of particles possess a zeta-potential of the same sign; therefore, in all cases the electrostatic interaction is repulsive and stronger in comparison to the attractive van der Waals interaction, leading to a positive sum of both contributions. The other three interactions, *i.e.*, PbO-Nb_2O_5, Nb_2O_5-MHC, and MHC-MHC, are attractive. The last pair has the same sign of the charge on the surface of both particles; therefore, the electrostatic interaction is repulsive, but due to the small value of $\zeta = 10$ mV the van der Waals attraction prevails, and thus the sum is negative. The PbO-Nb_2O_5 and Nb_2O_5-MHC pairs possess the opposite sign of ζ; therefore, both electrostatic and van der Waals interactions are negative, leading to the attractive potential. For the pH = 12.5 case, however, the PbO-Nb_2O_5, PbO-MHC, and MHC-MHC interactions change due to the change in the zeta-potentials (cf. Table 3 and Figure 22). In this case, the PbO-Nb_2O_5 and MHC-MHC interactions become

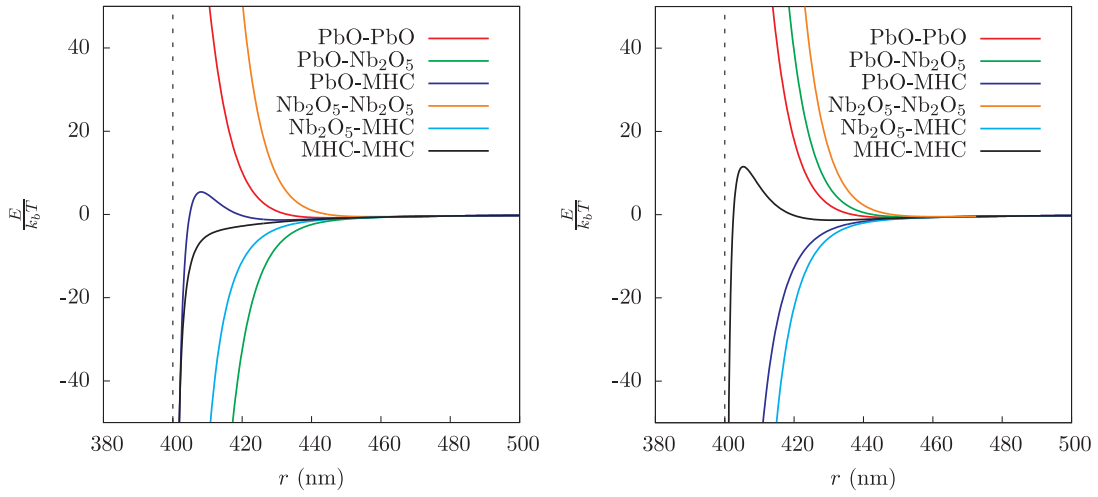

(a) Potentials pH = 11.4

(b) Potentials pH = 12.5

Figure 26: *Interaction potentials for the reagent particles of equal size.* Interaction potentials between six pairs of particles in the suspension. (a) pH11.4 sample and (b) pH12.5 sample.

repulsive, whereas the PbO-MHC interaction is attractive. Hence, comparing the two pH conditions, apart from the numerical values, the main difference appears in the PbO-Nb_2O_5 interaction, which is attractive at pH = 11.4, and repulsive at pH = 12.5.

The calculated interactions are then used in the simulations. As discussed above, our main focus here is on the spatial distribution of the reagent particles and the formation of their clusters in the suspensions. Therefore, the main simulation results concern the radial distribution functions (RDFs), which are computed for all the pairs of particles, as well as the snapshots of the equilibrium distributions of the particles emerging after a long simulation time. The results are presented in Figures 27a to 27d for both pH11.4 and pH12.5 samples. In Figures 27a and 27b the radial distribution functions $g(r)$ for the pairs of particles are presented. For clarity, the curves are systematically shifted upwards by 10 units. As both Figures 27a and 27b show, the length at which the perturbations in the RDFs are observed, is at least twice the range of the interaction potentials, which can be attributed to indirect interactions between these particles.

In the pH11.4 case, the RDFs can be divided in two groups: (*i*) the functions for PbO-Nb_2O_5, PbO-MHC, Nb_2O_5-MHC, and MHC-MHC radial distributions have a large sharp peak at 400 nm, which means that these pairs of particles are in contact (note that the closest approach is equal to the particle diameter 400 nm); (*ii*) in the RDFs of PbO-PbO and Nb_2O_5-Nb_2O_5 pairs, the first peak is observed at 450 nm. Moreover, the Nb_2O_5-Nb_2O_5 RDF includes three larger peaks observed at 450, 600, and 800 nm, whereas the PbO-PbO function has one diffusive peak ranging from 450 to 800 nm. From the RDF shapes we conclude that the PbO adsorbs to the surface of the Nb_2O_5 particles, thus the distances between two PbO particles adsorbed to Nb_2O_5 can be from 450 to 800 nm (an illustration is shown in Figure 28). This explains the occurrence of the diffusive peak from 450 to 800 nm in the RDF of the PbO-PbO pair. These shapes of the RDFs are in agreement with the equilibrium configuration of the particles presented in Figure 27c, where the PbO particles are colored red, the Nb_2O_5 particles

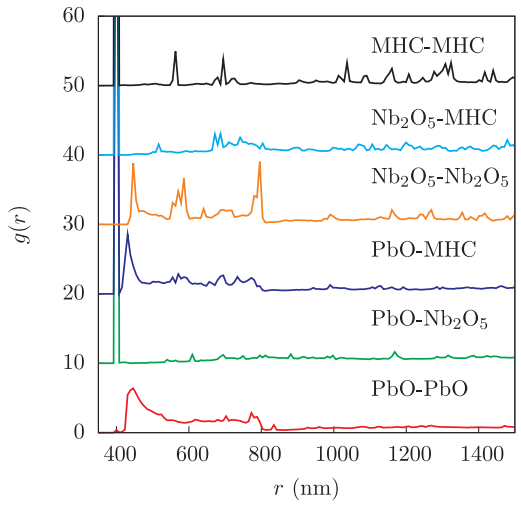

(a) RDFs pH = 11.4

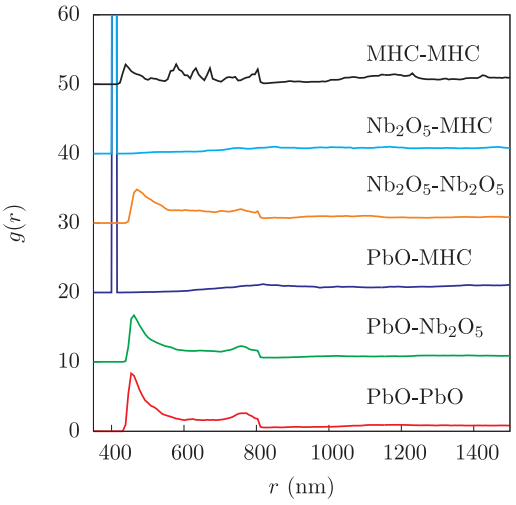

(b) RDFs pH = 12.5

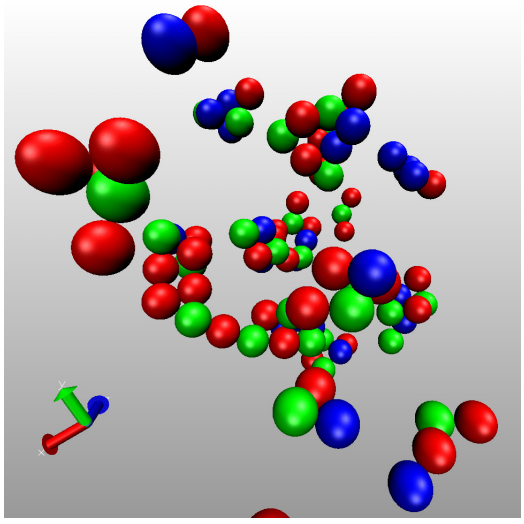

(c) Snapshot pH = 11.4

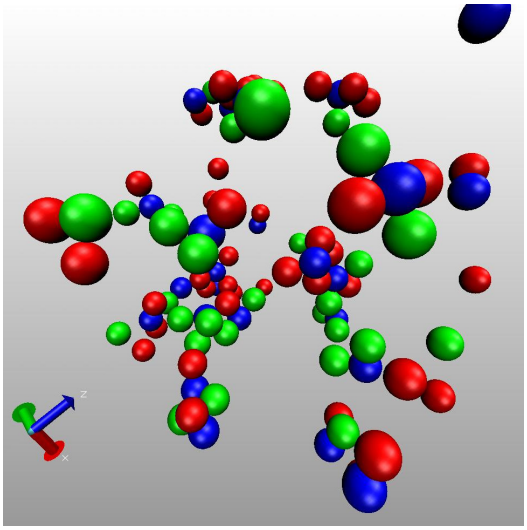

(d) Snapshot pH = 12.5

Figure 27: *Spatial distributions of the reagent particles of equal size.* (a) and (b) Simulated radial distribution functions for the pairs of particles, as indicated. (c) and (d) Snapshots of the equilibrated spatial distribution of particles in the suspensions, PbO is colored red, Nb_2O_5 green, and MHC blue. Perspective 3D views are generated with VMD program [99]. The results for the pH11.4 sample are presented on the left and for the pH12.5 sample on the right.

green, and the MHC particles blue. Clusters with contacts between PbO and Nb_2O_5 particles are visible, while the spatial distribution of MHC particles is inhomogeneous.

In the pH12.5 case, again two types of the RDFs can be distinguished, Figure 27b: The RDFs with a large sharp peak at 400 nm, for the PbO-MHC and Nb_2O_5-MHC functions, and the RDFs with a diffusive peak ranging from 450 to 800 nm, for the PbO-PbO, PbO-Nb_2O_5, Nb_2O_5-Nb_2O_5, and MHC-MHC functions. The contacts between the PbO-MHC and Nb_2O_5-MHC pairs, together with the diffusive shape of PbO-PbO, PbO-

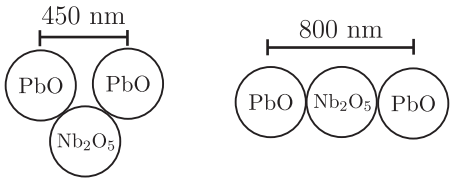

Figure 28: *Schematic presentation of two PbO particles adsorbed on the Nb_2O_5 particle.* The closest distance between two PbO particles is at 450 nm (repulsive potential), left configuration, and the largest at 800 nm, right configuration.

Nb_2O_5, and Nb_2O_5-Nb_2O_5 RDFs, could be explained with the adsorption of the PbO and Nb_2O_5 particles on the MHC particles. The adsorption of PbO and Nb_2O_5 on MHC particles is also seen in Figure 27d. Again, PbO is colored red, Nb_2O_5 green, and MHC blue. In agreement with the RDFs, the spatial distribution of the particles reveals the clusters where the PbO and Nb_2O_5 particles are separated by the MHC particles, and the distribution of MHC particles is more homogeneous.

Our simulation results reveal that the formation of colloidal clusters in the two samples is different. In particular, in contrast to the pH11.4 suspension, the contacts between the PbO and Nb_2O_5 are not seen in the pH12.5 sample. These findings are confirmed both by the absence of a sharp peak in the PbO-Nb_2O_5 RDF at the contact distance 400 nm, and by a visual inspection of the equilibrium cluster structures. While the clusters with contacts between the PbO and Nb_2O_5 particles are observed in the pH11.4 suspension, such clusters are absent in the pH12.5 sample, where the contacts between the PbO and Nb_2O_5 are prevented by the MHC particles. Consequently, the distribution of the MHC particles is more homogeneous in the pH12.5 suspension than in to the pH11.4 suspension.

In the pH11.4 sample the simulations reveal the formation of the clusters with contacts between the PbO and Nb_2O_5 particles and an uneven distribution of the MHC particles. This situation is favorable for the formation of the Pb-Nb pyrochlore phase, which is not desirable in the final product. In contrast to the pH11.4 case, such a type of clusters is not present in the pH12.5 sample, where the MHC particles prevent contacts between the PbO and Nb_2O_5 particles in the equilibrium clusters. Thus, after heating the sample, the formation of the pure perovskite phase should be more favorable.

Close inspection of the simulated structure of the agglomerates for the pH11.4 and pH12.5 samples, with example snapshots shown in Figures 27c and 27d, confirms two different types of clusters of the reagent particles, as anticipated on the basis of the experimental results, see Figure 22.

4.3.2 Particle size effects

In this section we further study the influence of the size of the particles on the cluster formation for both pH = 11.4 and pH = 12.5 conditions. The particle sizes affect the interaction potentials in Equations 3.2, 3.3 and 3.5. Hence, the geometry of the emergent clusters may change and consequently the physical properties of the agglomerates could be different. Examples of such agglomeration processes with two neutral colloidal particles of different sizes are studied in connection with the assembled nanoparticle films [102]. In the present case, the situation is more complex: apart from the geometric effects, we have three types of charged colloidal particles, whose zeta-potentials are different. The MHC particles should play a crucial role in the prevention of the pyrochlore phase by blocking the contacts between the PbO and Nb_2O_5 particles, as

shown in the previous section. Here, we examine how the size of the MHC particle can affect the process of cluster formation. In the simulations we assume that the size of the MHC particles is reduced to 200 nm in one case (smaller MHC particles) and in the other we reduce the sizes of both the PbO and Nb_2O_5 particles to 200 nm (bigger MHC particles). All the other parameters remain the same as in the case with equal-sized reagent particles. The summaries of all parameters are given in Tables 4 and 5.

Table 4: *Parameters of the interaction potential for different reagent particle sizes: Smaller MHC particles* (a_{PbO}, $a_{Nb_2O_5}$: $a_{MHC} = 2 : 1$). All the parameters used for the calculation of the particle-particle interaction potentials in the case of smaller MHC particles are given in this table.

pH	a_{PbO}, $a_{Nb_2O_5}$ [nm]	a_{MHC} [nm]	ψ_{PbO} [mV]	$\psi_{Nb_2O_5}$ [mV]	ψ_{MHC} [mV]	A_{ij} [J]	κ [m^{-1}]
11.4	200	100	40	−80	10	$3 \cdot 10^{-20}$	$1.6 \cdot 10^8$
12.5	200	100	−50	−100	20	$3 \cdot 10^{-20}$	$1.6 \cdot 10^8$

Table 5: *Parameters of the interaction potential for different reagent particle sizes: Bigger MHC particles* (a_{PbO}, $a_{Nb_2O_5}$: $a_{MHC} = 1 : 2$). All the parameters used for the calculation of the particle-particle interaction potentials in the case of bigger MHC particles are given in this table.

pH	a_{PbO}, $a_{Nb_2O_5}$ [nm]	a_{MHC} [nm]	ψ_{PbO} [mV]	$\psi_{Nb_2O_5}$ [mV]	ψ_{MHC} [mV]	A_{ij} [J]	κ [m^{-1}]
11.4	100	200	40	−80	10	$3 \cdot 10^{-20}$	$1.6 \cdot 10^8$
12.5	100	200	−50	−100	20	$3 \cdot 10^{-20}$	$1.6 \cdot 10^8$

The results of the simulations for the pH11.4 and pH12.5 samples with smaller MHC particles are presented in parallel in Figures 29 and 30. Due to the smaller size of the MHC particles the closest approaches of the particle pairs are now found at three different distances, beyond which the interaction range extends. These are the following distances: 200 nm (MHC-MHC pair), 300 nm (PbO-MHC and Nb_2O_5-MHC pairs), and 400 nm (PbO-PbO, PbO-Nb_2O_5, Nb_2O_5-Nb_2O_5 pairs). The computed interaction potentials for the pH11.4 sample are shown in Figure 29a. Three repulsive interactions, *i.e.*, between the PbO-PbO, Nb_2O_5-Nb_2O_5, PbO-MHC pairs, are found, while three attractive interactions are for the PbO-Nb_2O_5, Nb_2O_5-MHC, and MHC-MHC pairs of particles.

Likewise, as in the case of the equal-sized particles studied above, for the pH12.5 sample, shown in Figure 29b, the nature of the three interactions is altered in comparison with the pH11.4 sample, due to the changes in the zeta-potentials. Namely, the interactions PbO-Nb_2O_5 and MHC-MHC change from attractive to the repulsive, while the PbO-MHC interaction changes from repulsive to attractive. As shown below, the altered nature of the PbO-Nb_2O_5 interaction is crucial in this case for the cluster formation.

The simulated RDFs for the pairs of particles in the pH11.4 suspension are presented in Figure 30a. Again, two groups of functions are readily distinguished. One group comprises the RDFs with sharp peaks at a distance corresponding to the closest approach of two particles, as found for the PbO-Nb_2O_5, PbO-MHC, Nb_2O_5-MHC,

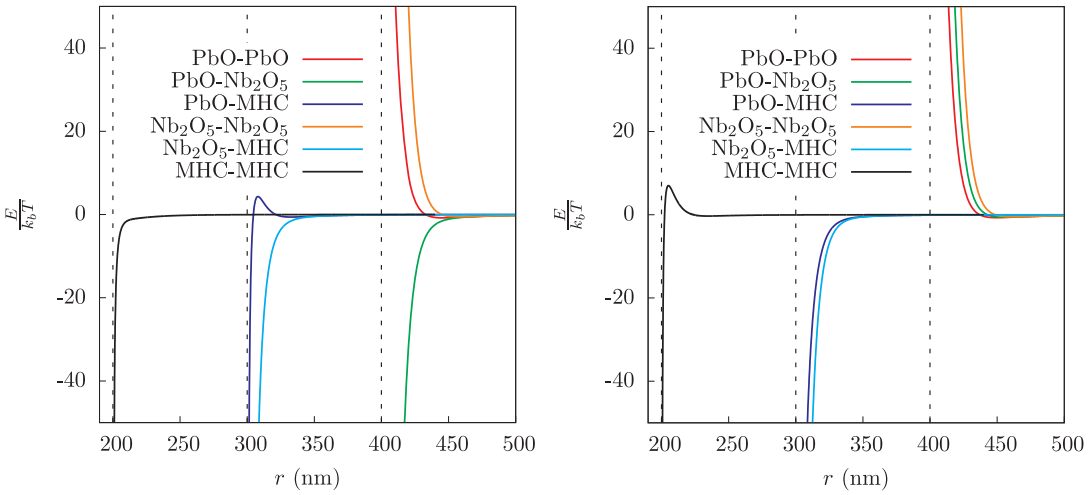

(a) Potentials pH = 11.4

(b) Potentials pH = 12.5

Figure 29: *Interaction potentials between the reagent particles - smaller MHC particles.* Interaction potentials between six pairs of particles in the suspension. (a) pH11.4 sample and (b) pH12.5 sample.

MHC-MHC pairs. The other group consists of the functions where the peaks at the distance of closest approach are absent, as found for the PbO-PbO and Nb_2O_5-Nb_2O_5 pairs. From the RDFs and the equilibrium distribution of the particles in suspension, which is shown in Figure 30c, it can be seen that not only the clusters of PbO and Nb_2O_5 are formed, but also the clusters of MHC particles are present. When the MHC particles form clusters by themselves, they do not adsorb to the surfaces of the PbO and Nb_2O_5, and consequently cannot prevent their contacts. Such a situation leads to a non-homogeneous distribution of MHC particles and clusters with close contacts between the PbO and Nb_2O_5 particles.

The situation is different in the pH12.5 sample; the respective RDFs and equilibrium distributions of particles are presented in Figures 30b and 30d. Three types of RDFs are found in the pH12.5 suspension. PbO-PbO, PbO-Nb_2O_5, and Nb_2O_5-Nb_2O_5 functions contain several peaks at distances larger than the distance of their closest approach. This implies that there are no contacts between these pairs of particles. The RDFs for the PbO-MHC and Nb_2O_5-MHC pairs exhibit just one large, sharp peak at the distance of the closest approach, indicating that practically all the MHC particles are adsorbed to the PbO and Nb_2O_5 surfaces. This is further confirmed with the shape of the MHC-MHC RDF, where in addition to the peak at their closest approach at 200 nm, also a diffusive peak from 200 nm to 600 nm is observed, which indicates the adsorption of MHC particles to the other two components. The snapshot of the equilibrium distribution of the particles, shown in Figure 30d, reveals that practically all the MHC particles are adsorbed to either PbO or Nb_2O_5. Although the clusters containing all three components form, the contact between PbO and Nb_2O_5 is always prevented by the MHC particles. Therefore, by increasing the pH to 12.5 we are able to achieve a homogeneous distribution of the MHC particles, which at the same time prevents contacts between the PbO and Nb_2O_5 particles.

Like in the case with equal-sized reagent particles, we can conclude that colloidal

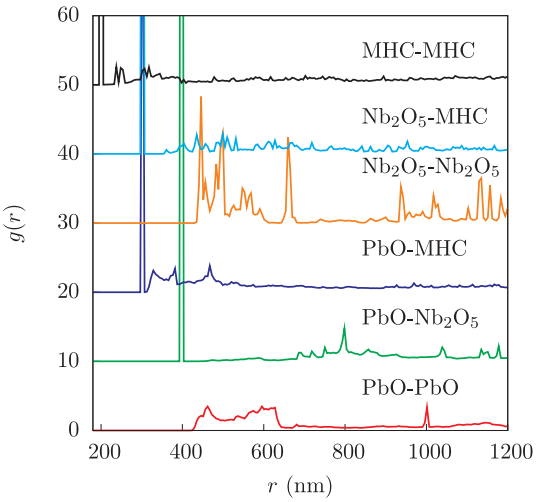

(a) RDFs pH = 11.4

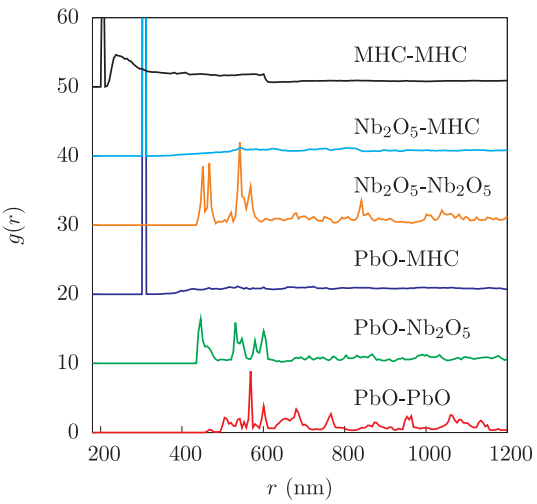

(b) RDFs pH = 12.5

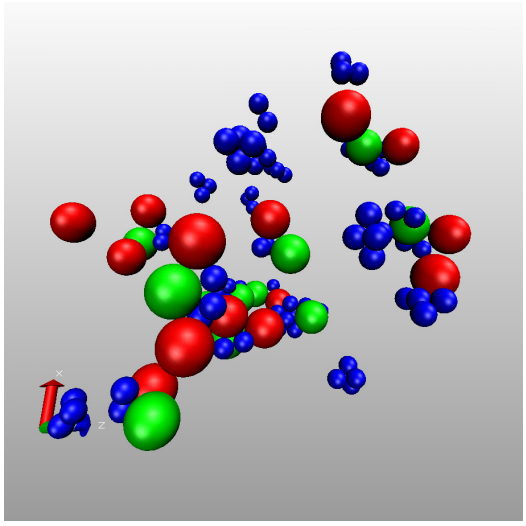

(c) Snapshot pH = 11.4

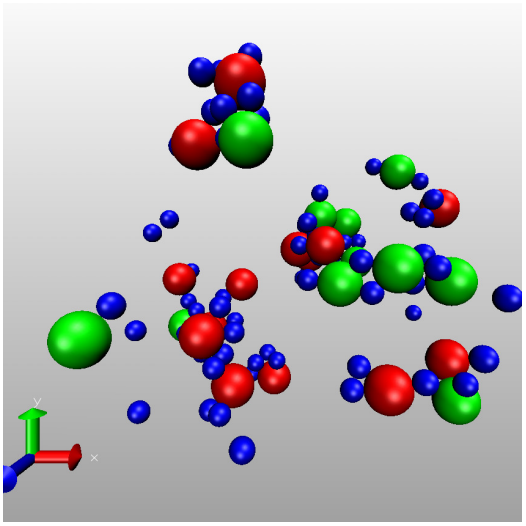

(d) Snapshot pH = 12.5

Figure 30: *Spatial distribution of the reagent particles - smaller MHC particles.* (a) and (b) Simulated radial distribution functions for the pairs of particles, as indicated. (c) and (d) Snapshots of the equilibrated spatial distribution of particles in the suspensions, PbO is colored red, Nb_2O_5 green, and MHC blue. Perspective 3D views are generated with VMD program [99]. The results for the pH11.4 sample are presented on the left and for the pH12.5 sample on the right.

assemblies formed at pH = 12.5 are more favorable for the synthesis of the single-phase perovskite PMN in comparison to the pH = 11.4 conditions.

The results for the system with bigger MHC particles are presented in Figures 31 and 32. Due to the differences in the actual sizes of the particles, the distances of their close contacts are changed as follows: for PbO-PbO, PbO-Nb_2O_5, and Nb_2O_5-Nb_2O_5 the interactions start at 200 nm, for PbO-MHC and Nb_2O_5-MHC at 300 nm, and for MHC-MHC at 400 nm. Apart from the different distances, the nature of the potentials remains the same as in the case of smaller MHC particles. At pH = 11.4,

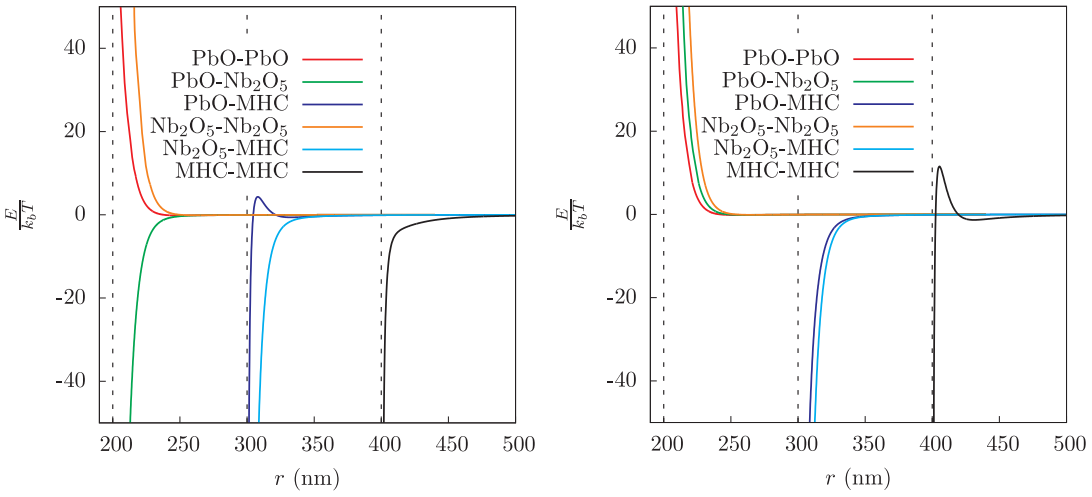

(a) Potentials pH = 11.4

(b) Potentials pH = 12.5

Figure 31: *Interaction potentials between the reagent particles - bigger MHC particles.* Interaction potentials between six pairs of particles in the suspension. (a) pH11.4 sample and (b) pH12.5 sample.

the potentials between the PbO–PbO, Nb_2O_5-Nb_2O_5, PbO–MHC pairs are attractive, whereas repulsive potentials exist between the PbO-Nb_2O_5, Nb_2O_5-MHC, and MHC-MHC pairs. At pH = 12.5, on the other hand, the interactions between PbO-Nb_2O_5 and MHC-MHC are repulsive, and the PbO-MHC interaction is attractive, for the reasons already explained above.

In Figures 32a and 32c the computed RDFs for different pairs and a snapshot of equilibrium distributions of the particles at pH = 11.4 are presented. We can observe the formation of worm-like clusters of PbO and Nb_2O_5 particles, and the presence of clusters is confirmed with the peak in the PbO-Nb_2O_5 RDF at the distance of closest approach.The PbO and Nb_2O_5 particles are also partly adsorbed on the MHC particles, which is also seen from the peaks of the PbO-MHC and Nb_2O_5-MHC RDFs. Similar to both previous cases, at pH = 11.4, here we also observe a large number of contacts between the PbO and Nb_2O_5 particles, which are undesirable for the synthesis.

In Figures 32b and 32df the results for the pH = 12.5 conditions and the larger MHC particles are presented. Like in the case with equal-sized reagent particles, the diffusive peaks in the PbO-PbO, PbO-Nb_2O_5, and Nb_2O_5-Nb_2O_5 RDFs are observed, while the sharp peaks at the distance of the closest approach in the Pb-MHC and Nb_2O_5-MHC RDFs are seen. From these results and also from the spatial distribution of the particles, we can conclude that the PbO and Nb_2O_5 particles are adsorbed on the MHC particles and that the contacts between the PbO and Nb_2O_5 particles are effectively prevented. However, from Figure 32d it can be observed, that not all the PbO and Nb_2O_5 particles are adsorbed on the MHC particles. To quantify the adsorption, the amount of isolated PbO and Nb_2O_5 particles is calculated. About 43 % of the PbO and Nb_2O_5 particles are adsorbed to the MHC particles, which leaves 57 % of them isolated. From the point of view of a solid-state reaction, only partial adsorption of the PbO and Nb_2O_5 particles is not beneficial. Although we do not have contacts between PbO and Nb_2O_5 particles in the suspension, the situation can change during the drying process. Firstly, during

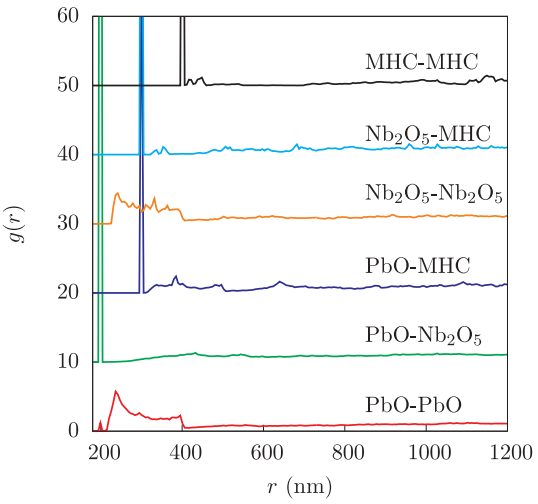

(a) RDFs pH = 11.4

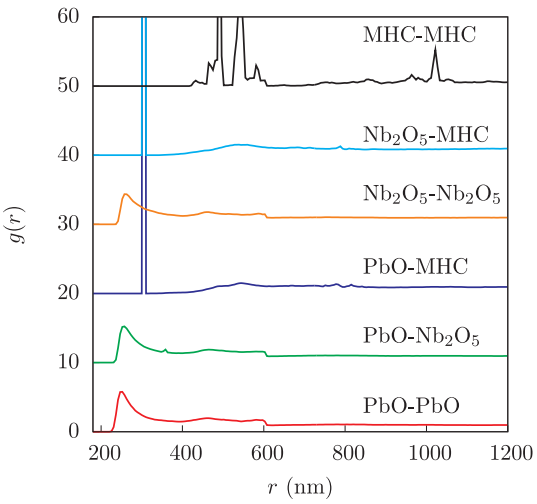

(b) RDFs pH = 12.5

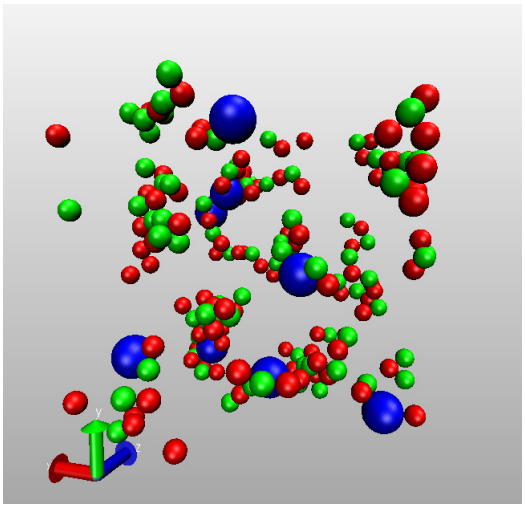

(c) Snapshot pH = 11.4

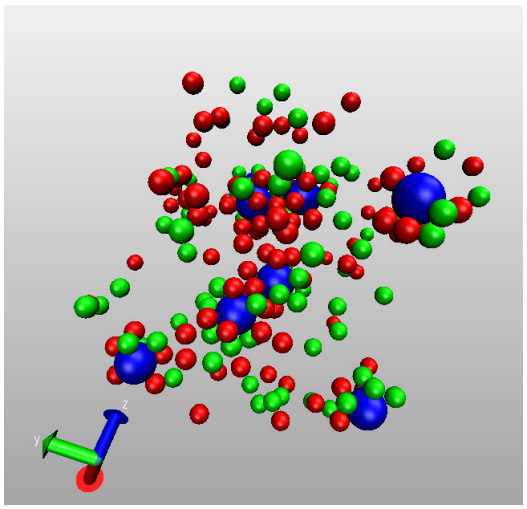

(d) Snapshot pH = 12.5

Figure 32: *Spatial distribution of the reagent particles - bigger MHC particles.* (a) and (b) Simulated radial distribution functions for the pairs of particles, as indicated. (c) and (d) Snapshots of the equilibrated spatial distribution of particles in the suspensions, PbO is colored red, Nb_2O_5 green, and MHC blue. Perspective 3D views are generated with VMD program [99]. The results for the pH11.4 sample are presented on the left and for the pH12.5 sample on the right.

drying the screening length κ is increasing, due to the increase of the ion concentration, and consequently the van der Waals forces become dominant. This could lead to an attractive potential between the PbO and Nb_2O_5. Secondly, an additional attraction between these particles may also be caused by capillary forces. Having more than 50 % of the PbO and Nb_2O_5 particles unadsorbed, we can expect that a number of them may get in close contact during the drying process of the perovskite synthesis.

To further judge the effects of the size of the MHC particles, the results of the

pH12.5 sample are compared for the three cases (*i.e.*, MHC of equal size to the other two types, smaller MHC, and bigger MHC), corresponding to the Figures 27, 30, and 32. There is no change in the type of pair interactions. In all the cases four repulsive and two attractive interactions are present, see Figures 26b, 29b, 31b. However, the distance at which these interactions are active is changed when the size of the MHC particles is changed. The difference is in the steric effect, which influences the equilibrium distribution of the particles in the suspension. Due to the smaller size, the number of MHC particles is higher in the case of smaller MHC particles, and thus several MHC particles are adsorbed to one PbO or Nb_2O_5 particle, thus sterically preventing the contacts between PbO and Nb_2O_5. In the case of equal-sized particles, the situation is that several PbO and Nb_2O_5 particles adsorb to one MHC particle. In the case of the bigger size of MHC particles, even more PbO and Nb_2O_5 particles are adsorbed on one MHC particle, while more than 50 % of them are not adsorbed. The effect of sterically preventing the contacts between the PbO and Nb_2O_5 is thus more pronounced when the MHC particles are of smaller size and their number is larger (to keep the same volume fraction). The simulation results imply that in the case where the MHC particles are smaller, the structure of the clusters can be even more favorable for the perovskite formation. This further suggests that smaller MHC particles should be preferentialy used in the experiments or need to be pre-milled to reduce their size.

4.3.3 Contacts between reagent particles in the suspension

For efficient solid-state reactions the contacts between the reacting particles are crucial. As is explained in the Introduction, for a multicomponent system not all such contacts are beneficial. In our three-component system the six possible contacts are PbO-PbO, Nb_2O_5-Nb_2O_5, MHC-MHC, PbO-Nb_2O_5, PbO-MHC, and Nb_2O_5-MHC contacts. Here we calculate the number of contacts in the agglomerates of the reagent particles. We present the results in the form of a matrix of contacts, its description is given in Materials and Methods, see Figure 21. Contacts between PbO-MHC and Nb_2O_5-MHC are desired for the solid-state reaction in the perovskite synthesis. However, the PbO-Nb_2O_5 contacts need to be avoided, because they promote the formation of undesirable pyrochlore phases. The contacts between the same type of particles, *i.e.*, PbO-PbO, Nb_2O_5-Nb_2O_5, and MHC-MHC, are also not desired. For the case of our simulations the legend of *desired* and *not desired contacts* is presented in Figure 33.

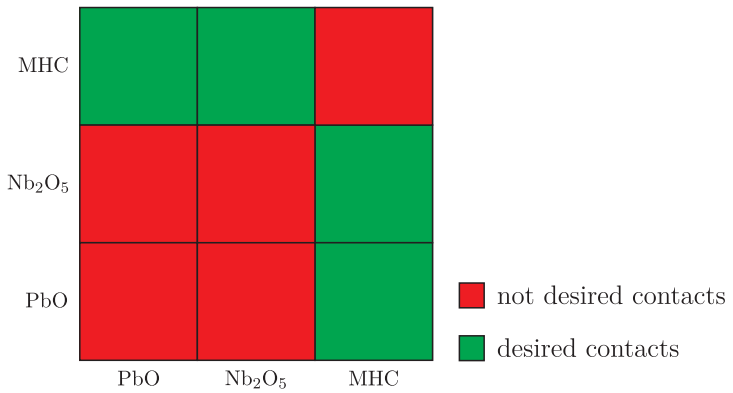

Figure 33: *Matrix of desired and not desired contacts.* Cell ij represents the contact between the particle in the row i and column j. Desired contacts are colored green and not desired contacts red.

The number of contacts per particle is calculated for the equilibrium distributions of particles. The results are presented in the matrices in Figures 34, 35, 36. Each matrix cell represents the number of contacts between two corresponding types of particles in the agglomerate. The contacts are normalized per number of particles presented in the columns. For example in Figure 34a the color of the matrix cell Nb_2O_5-PbO

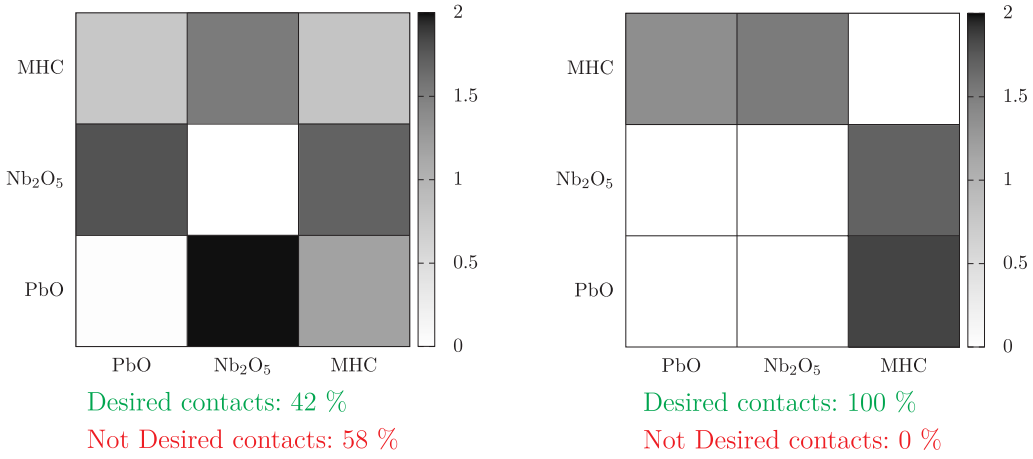

(a) Contacts pH = 11.4

(b) Contacts pH = 12.5

Figure 34: *Matrices of contacts between reagent particles of equal size.* Number of contacts per particle between the reagent particles is in our system calculated from the equilibrated distributions of particles. The color of the matrix cell represents the number of contacts between the particles in rows and columns normalized per number of particles in the columns. The results for the pH11.4 sample are presented on the left and for the pH12.5 sample on the right.

corresponds to the number of contacts between the PbO and Nb_2O_5 normalized per number of PbO particles in the simulation box. The result is 1.4, which shows that there are on average 1.4 Nb_2O_5 particles in contact with one PbO particle in the case of equal-sized particles at pH = 11.4. The PbO particles are also in contact with the MHC, but less then 0.5 MHC are on average connected with one PbO. The Nb_2O_5 particles are in contact with 1.8 PbO and 1 MHC particles on average. The MHC particles are in contact with all three species, *i.e.*, PbO, Nb_2O_5, and MHC. The ratio between the desired, *i.e.*, PbO-MHC, Nb_2O_5-MHC, and not desired, *i.e.*, PbO-PbO, Nb_2O_5-Nb_2O_5, MHC-MHC, PbO-Nb_2O_5, contacts is also presented in the figure. For the pH11.4 case, with equal-sized particles, the 42 % of contacts are desired and 58 % are not desired. On the contrary, the pH12.5 sample, with equal-sized particles (Figure 34b), contains only desired contacts. Both PbO and Nb_2O_5 are in contact with approximately one MHC particle. One MHC particle is on average in contact with 1.5 PbO particles and 1.2 Nb_2O_5 particles.

Figure 35 presents the results for the systems with smaller MHC particles. At pH = 11.4 almost one Nb_2O_5 particle is in contact with one PbO particle, more than one PbO particle is in contact with one Nb_2O_5, and also one MHC particle is in contact with one MHC. These are not desired contacts, which account for more than 70 % of all the contacts in the system. But desired PbO-MHC, and Nb_2O_5-MHC contacts are also

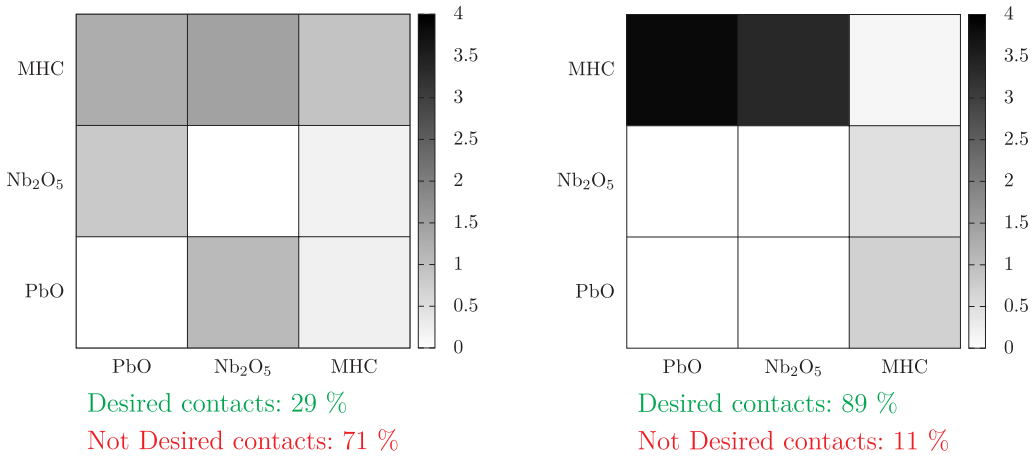

(a) Contacts pH = 11.4

(b) Contacts pH = 12.5

Figure 35: *Matrices of contacts for reagent particles - smaller MHC particles.* Number of contacts per particle between the reagent particles is in our system calculated from the equilibrated distributions of particles. The color of the matrix cell represents the number of contacts between the particles in rows and columns normalized per number of particles in the columns. The results for the pH11.4 sample are presented on the left and for the pH12.5 sample on the right.

present in the suspension. The opposite result is again observed at pH = 12.5, where almost 90 % of the contacts are the desired ones. Almost 4 MHC particles are in contact with one PbO at pH = 12.5, whereas at pH = 11.4 this value is only 1.3. Similarly, there are 3.4 MHC particles in contact with one Nb_2O_5 at pH = 12.5, and only 1.4 at pH = 11.4. Furthermore, a smaller amount of not desired MHC-MHC contacts is observed at pH = 12.5 in comparison to pH = 11.4.

The case with bigger MHC particles is presented in Figure 36. Again there are almost 90 % of all the contacts at pH = 11.4 that are not desired, whereas at pH = 12.5 only the desired contacts are present. At the lower pH the majority of contacts are of the PbO-Nb_2O_5 type and there are some PbO-MHC and Nb_2O_5-MHC contacts present. In contrast at the higher pH only PbO-MHC and Nb_2O_5-MHC contacts are present. In this case one MHC particle is in contact with 6.5 PbO particles and 4.5 Nb_2O_5 particles, on average.

If we compare only the pH12.5 samples with different sizes of MHC particles (see Figures 34b, 35b, and 36b), we can observe that the size and consequently the number of MHC particles, have a major influence on the number of a certain type of contacts. For example, one PbO particle is in contact with a different number of MHC particles under different conditions. The smaller size of MHC particles enables a higher number of MHC particles in contact with either one PbO or one Nb_2O_5. This enables an effective steric hindrance for the formation of PbO-Nb_2O_5 contacts, which is beneficial for the solid-state reaction.

In summary, for the statistics of the particle contacts, we can conclude that the higher pH and the smaller size of the MHC particles make the conditions that are preferable for the desired solid-state reactions.

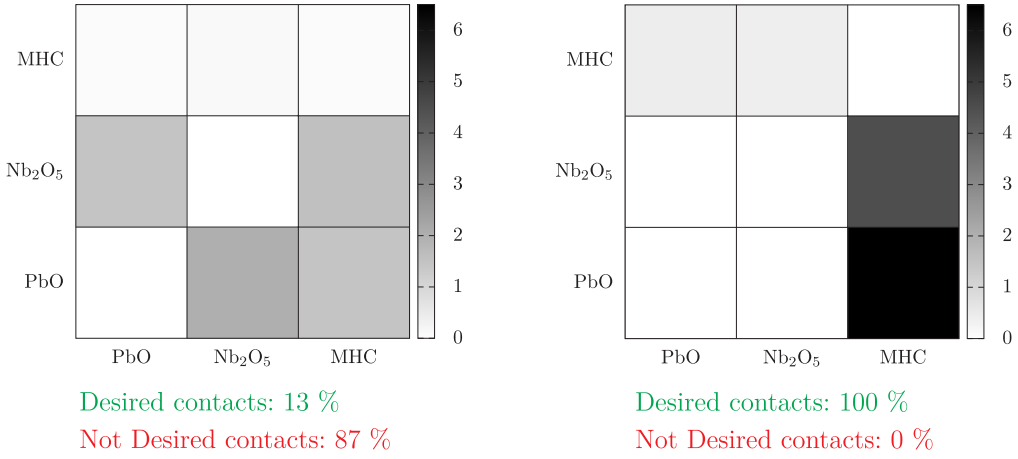

(a) Contacts pH = 11.4

(b) Contacts pH = 12.5

Figure 36: *Matrices of contacts for reagent particles - bigger MHC particles.* Number of contacts per particle between the reagent particles is in our system calculated from the equilibrated distributions of particles. The color of the matrix cell represents the number of contacts between the particles in rows and columns normalized per number of particles in the columns. The results for the pH11.4 sample are presented on the left and for the pH12.5 sample on the right.

4.4 Summary

Within the MC simulations we have investigated the formation of clusters of charged colloidal particles of the reagent powders lead oxide, magnesium hydroxy carbonate (MHC), and niobium oxide in aqueous suspensions with the conditions corresponding to the experimental conditions used for the $Pb(Mg_{1/3}Nb_{2/3})O_3$ powder synthesis. Our focus has been to investigate the spatial distributions of the reagent particles that arise through the agglomeration in the aqueous suspension, which is relevant in view of the subsequent solid-state reactions for the PMN synthesis.

In close relation with the experimental parameters, in particular the zeta-potentials and volume fractions of the reagent particles, our numerical simulations have revealed that different types of clusters are energetically favored at different pHs of the suspensions. Specifically, at pH = 11.4 a large population of the precursor clusters in which close contacts between the PbO and Nb_2O_5 is achieved. Thus the formation of the undesirable pyrochlore phase can be enhanced in the subsequent solid-state reaction between these particles. In contrast, at higher pH = 12.5, the zeta-potentials of the reagent particles change such that the nature of the attraction-repulsion potentials between these pairs of particles is altered. The resulting equilibrium clusters contain the reagent particles PbO and Nb_2O_5, effectively separated by the MHC particles. The situations of an equal size of all reagent particles and the numerically investigated situation with smaller MHC particles are particularly favorable for this type of clusters, from which then the pure perovskite phase can be formed.

For the purpose of this work we kept the parameters of the model as close to the possible experimental conditions and investigated the cluster formation of the precursor

particles, which is relevant for the experiment. The parameters stemming from the pH values of the suspension and the particle sizes have been varied in the simulations. The results from the simulations are a good basis for the further experimental validation of the proposed hypothesis.

Within the model and the MC methods, the values of the other parameters can also be varied. For instance, the volume fraction of different reagent particles can be varied in a much wider range, which can be relevant for the analysis of the cluster-cluster agglomeration processes. However, for the present study we have limited our simulations only to the experimental parameters that should, in our opinion, have the strongest influence on the agglomeration process, *e.g.*, pH.

In summary, we have shown how the computer simulations, based on suitable models and realistic parameters, can help to unravel the processes that occur at the particle level in the synthesis of the PMN ceramics. With such information at hand, it is possible to apply such experimental parameters that enable the production of high-quality materials.

5

Synthesis of PMN from Aqueous Suspensions

Controlled Agglomeration for PMN Synthesis

Equipped with knowledge about cluster formation in suspensions for PMN synthesis from the previous Chapter, we present here the experimental validation of our hypothesis. First, we explore the properties of the dried reagent powder mixtures under different pH conditions. Next, the phase evolution of these mixtures upon heating and the morphology of the as-calcined powders are addressed. Finally we prepare the ceramics from the calcined powders and study their properties in correlation with different pH conditions used in suspensions of the reagent powder mixtures.

5.1 Introduction

Perovskite relaxor ferroelectric materials with the general formula $Pb(B1,B2)O_3$, where B1 and B2 are usually a low-valence cation (*e.g.*, Mg^{2+}, Zn^{2+}, Fe^{3+}, Ni^{2+}, Sc^{3+}) and a high-valence cation (*e.g.*, W^{6+}, Nb^{5+}, Ta^{5+}), respectively, are known for their large dielectric permittivity ($\varepsilon_r \sim 20000$) and large electrostrictive response (strain ~ 0.1 %). The most studied materials from this family are $Pb(Mg_{1/3}Nb_{2/3})O_3$ (PMN) and $Pb(Mg_{1/3}Nb_{2/3})O_3$-$PbTiO_3$ (PMN-PT). PMN-based relaxor ferroelectrics are used as high-strain electrostrictive actuators and high-dielectric-permittivity capacitors [8, 12, 13, 14].

In this Chapter we will focus on the synthesis of PMN. We have already explained the problems connected with the synthesis of PMN-based materials in the Introduction and Aims and Hypothesis, here we will just briefly repeat it. In the reaction mixture for PMN solid-state synthesis PbO and Nb_2O_5 preferentially react to form the Pb-Nb pyrochlore phase. Due to the high stability of the pyrochlores the reaction between PbO, Nb_2O_5 and MgO is not complete and in addition to the desired perovskite PMN, unwanted pyrochlore phases are also left in the final product. To avoid the formation of the pyrochlore Swartz and Shrout proposed a two-step synthesis, known as the *columbite* method [18]. In the first step they synthesized the columbite, $MgNb_2O_6$, and in the second step PbO and $MgNb_2O_6$ reacted to form the perovskite PMN. With the first reaction they tried to avoid the formation of Pb-Nb pyrochlore phases. Later, other approaches have been developed, usually with the aim of avoiding the additional calcination step and trying to prepare pure perovskite PMN in a single-calcination step

synthesis, for details see Introduction.

Our idea to prepare pure perovskite PMN in a solid-state synthesis using only one calcination step is based on the design of the contacts between the reagent particles, see Aims and Hypothesis. This would simplify the synthesis in comparison to the two-step columbite method. Computer simulations show that when mixing reagent particles at pH = 11.4 agglomerates with PbO-Nb_2O_5 contacts predominantly form; on the other hand, at pH = 12.5 the contacts between lead and niobium oxide are in most cases blocked by positively charged MHC particles. Therefore, the former conditions should enhance the reaction to unwanted pyrochlore phases, whereas the latter should be more suitable for the synthesis of pure perovskite PMN powder. We assume that the expected different arrangements of reagent particles in the powder mixtures should influence the phase composition of the powders also at intermediate heating temperatures. Our aim is to further explore the possibility of decreasing the sintering temperature of PMN ceramics. Although the often reported sintering temperatures of PMN ceramics from solid-state synthesized powders are about 1200 °C [103, 104, 105, 106, 107], lowering the sintering temperature would be beneficial from the point of view of keeping the stoichiometry, *i.e.*, avoiding or at least reducing the lead oxide volatilization and also in connection to integration issues, for example, in thick-film processing or in multilayer capacitors [13, 108, 109, 110].

5.2 Formation of Agglomerates for PMN Synthesis

Having in mind all that we have discussed about PMN synthesis, the following conditions need to be considered for obtaining single-phase perovskite by a single-step, solid-state reaction:

1. Contacts between the lead oxide and niobium oxide particles should be avoided to prevent the formation of parasitic pyrochlore phases.
2. The magnesium species should be homogeneously distributed between the lead and niobium oxide particles. Note that the weight fraction of Mg-species in the powder mixture is by far the least.

Our approach is to tune the interactions between the colloidal particles of the starting powders in the suspension to obtain colloidal agglomerates that would satisfy the two conditions discussed above. To achieve this, the electrostatic surface charge of the constituent particles is adjusted with the pH of the suspension.

5.2.1 Electrokinetic Properties of the Starting Powders

The zeta-potential (ζ) is measured as a function of the suspension pH (Figure 37a). The ζ of PbO is +50 mV at pH 10 and it decreases rapidly with increasing pH, reaching −50 mV at pH 12.5. The isoelectric point (IEP) is at 11.8. Below the IEP, the surface charge is due to the presence of Pb^{2+}(aq) and $Pb(OH)^{+}$(aq), and above the IEP, to $[Pb(OH)_3]^{-}$(aq) and $[Pb(OH)_4]^{2-}$(aq) ions [111].

Nb_2O_5 is positively charged at very low pH, about +20 mV at pH 2 and the IEP is at pH 2.4. With increasing pH the surface charge decreases and it reaches −85 mV at pH 12. The species in the pH range above 2.4 are the $[H_xNb_6O_{19}]^{(8-x)-}$ ions with $x = 0 - 2$ [112].

The shape of the ζ vs. pH curve for hydromagnesite is quite different from the former two. Its IEP is at pH 10.8 and with increasing pH the surface charge increases, reaching almost +20 mV at pH 12.5. The charged species above the IEP are Mg^{2+}(aq) and $Mg(OH)^{+}$(aq) [113]. Below pH 10 the powder starts to dissolve. With a ionic strength

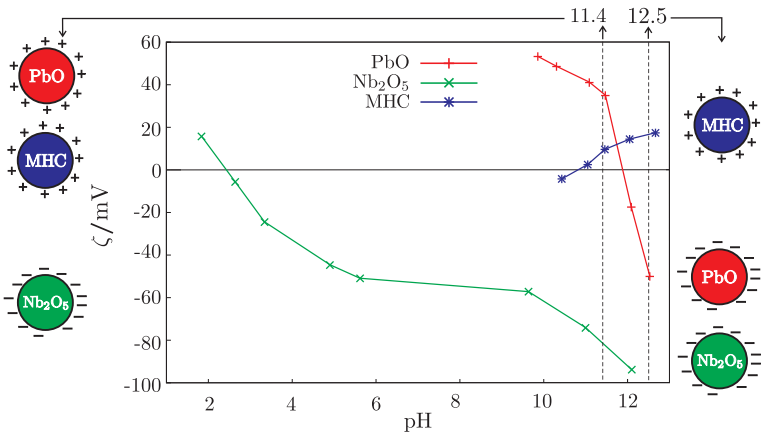

(a) Zeta-potential vs pH

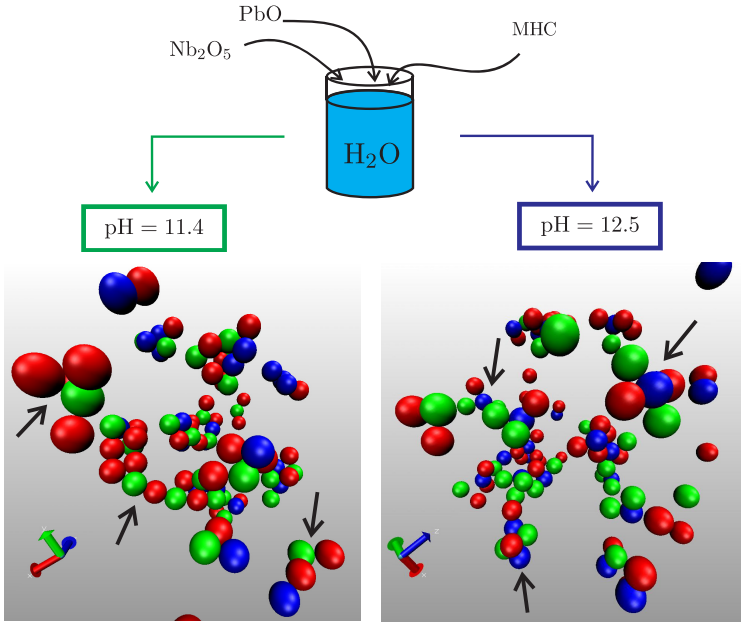

(b) Simulated agglomerate formation

Figure 37: *Agglomeration in the suspensions of the reagent powder mixture.* (a) Zeta-potential of the as-received PbO, MHC and Nb_2O_5 particles measured in deionized water as a function of the suspension pH. (b) Presentation of the simulated colloidal agglomerates formed in the suspensions at pH = 11.4 and pH = 12.5.

and a constant surface composition of the particles the zeta-potential should decrease with increasing pH, which is usually the case for oxide powders, also for PbO and Nb_2O_5. However our results show the opposite trend for the hydromagnesite particles. This behavior has already been observed experimentally [42, 113]. The lower zeta-potential values at lower pH could be explained by the higher solubility of Mg^{2+} (aq), which increases the ionic strength, compresses the double-layer and thus the zeta-potential is decreased. However this behavior is not studied in detail here, and for our proposed mechanism it is only important that the hydromagnesite particles exhibit a positive zeta-potential at high pH values.

Based on the results of the MC simulations we decided to homogenize the reagent powder mixtures at the inherent pH = 11.4, and pH = 12.5. Experiments using an

aqueous suspension with pH = 10.0 and a suspension where acetone is used as the dispersing medium are also conducted. The three chosen pH conditions are:

- pH 10, where PbO and Nb_2O_5 have opposite surface charges, +50 mV and −60 mV, respectively, and are therefore attracted, while for hydromagnesite $\zeta \approx 0$,
- inherent pH 11.4, where PbO and Nb_2O_5 still have opposite charges, while hydromagnesite is positively charged,
- and 12.5, where hydromagnesite is positively charged, and the ζ of PbO and Nb_2O_5 are −50 mV and −95 mV, respectively, so we predict attraction between the MHC and the more negatively charged Nb_2O_5 and PbO particles, and repulsion between the PbO and Nb_2O_5 particles.

In Figure 37b the simulation results from the previous Chapter are presented. At pH = 11.4, which is the inherent pH of the suspension, the PbO and Nb_2O_5 are oppositely charged and the attraction between these particles leads to agglomerates with close contacts between the PbO and Nb_2O_5. In Figure 37b clusters with PbO-Nb_2O_5 contacts are marked with arrows. The formation of similar agglomerates is also expected at pH 10.0. In contrast, at pH 12.5 colloid-colloid interactions lead to colloidal assemblies without close contacts between the PbO and Nb_2O_5 particles, due to repulsion between these particles, and a homogeneous distribution of the hydromagnesite particles between the PbO and Nb_2O_5 as a consequence of the attraction between oppositely charged particles, see Figure 37b. It is important to stress here, that besides the repulsion between PbO and Nb_2O_5, the positive charge on the hydromagnesite particles is crucial for the formation of the desired agglomerates. It enables the formation of hetero-agglomerates, where positive magnesite particles coat the negative lead and niobium oxide particles and thus prevent the direct contacts between PbO and Nb_2O_5.

From all the data presented above we can conclude that the starting pH 12.5 should be more favorable for the direct formation of the perovskite phase after the drying and calcination in comparison to the conditions at pH 10.0 and 11.4.

For the suspensions in acetone we expect no or only minor amount of reactions on the surface of the particles. This means that the particles suspended in acetone are not charged or only weakly charged in comparison to the aqueous suspensions, which results in no special or only weak electrostatic interactions between particles, however van der Waals interactions are still present. The formation of the preferred type of agglomerates is thus not expected; the particles form agglomerates, which are randomly distributed. For that reason the suspensions are also prepared in acetone for comparison.

The mechanism where soluble magnesium species would coat Nb_2O_5 and/or PbO particles, similar to the one reported by Gu et al. [39, 40], could also be possible. Due to the higher solubility of Mg species at lower pH, the pH 10 and 11.4 should be more favorable for the formation of a pure perovskite phase in comparison to pH 12.5. However, as is shown in next sections, the pure perovskite powder is only formed at pH 12.5. Therefore, the first proposed mechanism for the formation of colloidal agglomerates is more probable.

5.2.2 Phase Composition of the Starting Powders After Milling

We first separately mill all the reagent powders to see the effect of milling on the starting components, *i.e.*, PbO, Nb_2O_5 and MHC.

The powders obtained by drying the lead oxide, which is attrition-milled in an aqueous medium at pH 10.0 and 12.5, are dark orange, similar to the as-received powder,

and covered with a white surface layer, which we observe immediately after milling. The XRD patterns of the as-received PbO and of the milled powders are shown in Figure 38. The as-received powder is a mixture of orthorhombic PbO (massicot, PDF 77-1971)

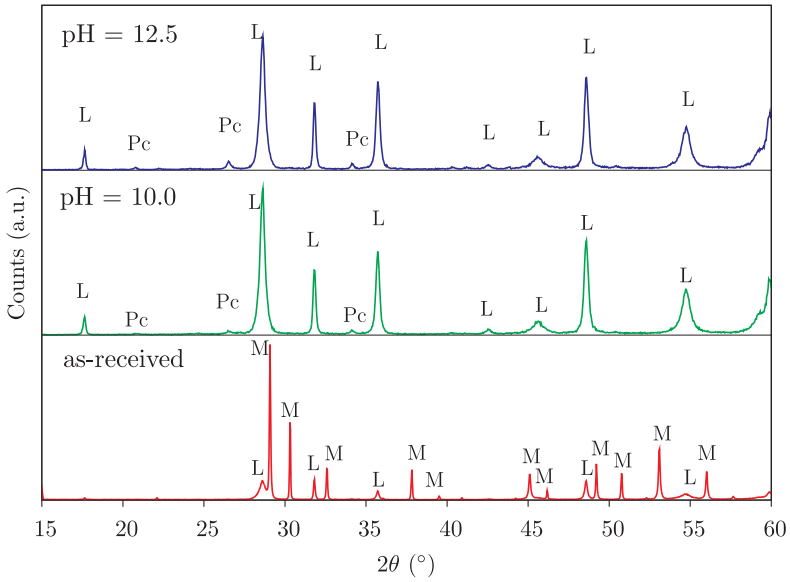

Figure 38: *PbO milling.* XRD patterns of the as-received PbO and of PbO after attrition-milling at pH 10.0 and 12.5. M - orthorhombic PbO (massicot), L - tetragonal PbO (litharge), Pc - $PbO \cdot 6PbCO_3 \cdot 3Pb(OH)_2$.

with a small amount of tetragonal PbO (litharge, PDF 85-1739). In contrast, the as-milled powders consist predominantly of tetragonal PbO and traces of a phase which is indexed by $PbO \cdot 6PbCO_3 \cdot 3Pb(OH)_2$ (hexagonal lead oxide carbonate hydroxide, PDF 19-680). The transformation of metastable orthorhombic PbO to the stable, low-temperature, tetragonal form upon mechanochemical activation has been frequently reported [34, 35, 36]. Senna et al. observed that the massicot-litharge transformation occurred even upon isothermal ball-milling in hexane [114]. We assume that a minor amount of white-colored lead oxide carbonate hydroxide forms as a consequence of the partial dissolution of PbO in the alkaline medium, which was observed also by Ziemniak et al. [115], and the further reaction of the soluble lead species with carbonate ions, stemming from the dissolved atmospheric CO_2.

The phase composition of the as-received hydromagnesite and niobium oxide powders is not influenced by the attrition-milling with the pH set at 10.0 and 12.5. The intensities and the positions of the diffraction peaks are in all cases indexed as monoclinic $(MgCO_3) \cdot 4Mg(OH)_2 \cdot 4H_2O$ (PDF 70-361) and orthorhombic Nb_2O_5 (PDF 30-873), respectively (Figure 39).

5.2.3 Phase Composition of the Dried Reagent Powder Mixtures

The PbO, MHC, and Nb_2O_5 powders are homogenized in water and acetone in a molar ratio corresponding to the stoichiometry of $Pb(Mg_{1/3}Nb_{2/3})O_3$. The pH of the aqueous suspensions is set TO 10.0 by formic acid, inherent pH 11.4, and 12.5 by NH_3(aq). After milling the suspensions are dried. The samples are further denoted as pH10.0, pH11.4, pH12.5, and acetone sample.

The XRD patterns of the dried powder mixtures are shown in Figure 40. In all three samples obtained from the aqueous suspensions, the presence of the reflections

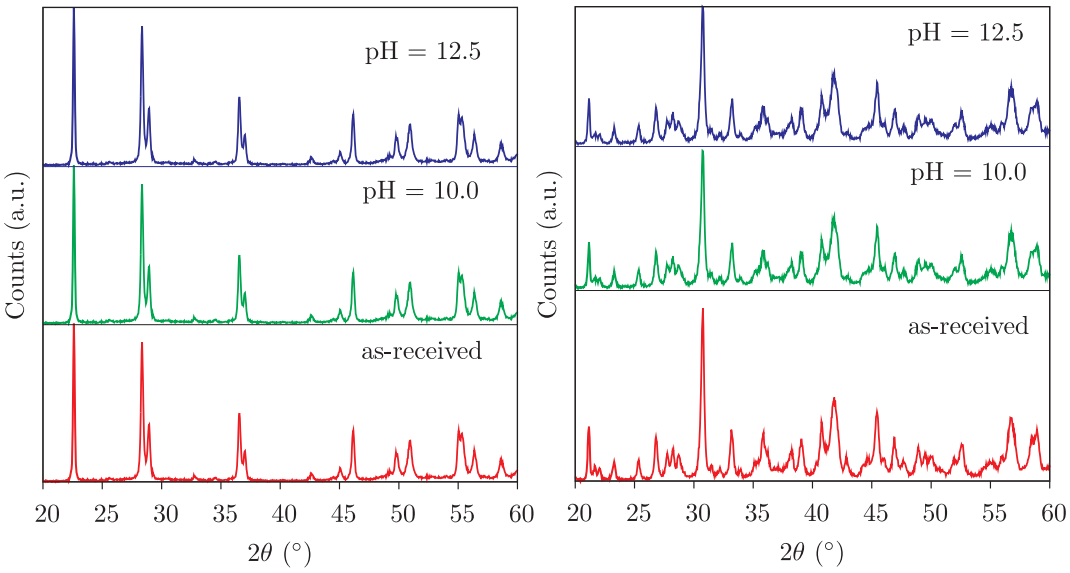

(a) XRD Nb_2O_5 (b) XRD MHC

Figure 39: *Milling of Nb_2O_5 and MHC.* (a) XRD patterns of the as-received Nb_2O_5 and of MHC after attrition-milling at pH 10.0 and 12.5, all the peaks belong to the orthorhombic Nb_2O_5. (b) XRD patterns of the as-received MHC and of MHC after attrition-milling at pH 10.0 and 12.5, all the peaks belong to monoclinic $(MgCO_3)_4{\cdot}Mg(OH)_2{\cdot}4H_2O$.

that correspond to hexagonal $PbO \cdot 6PbCO_3 \cdot 3Pb(OH)_2$ (PDF 19-680), tetragonal PbO (litharge, PDF 85-1739), orthorhombic Nb_2O_5 (PDF 30-873), and $Mg(OH)_2$ (brucite, PDF 82-2454) is determined. We could observe no diffraction peaks of the orthorhombic PbO or $(MgCO_3)_4{\cdot}Mg(OH)_2{\cdot}4H_2O$, which are the main constituents of the as-received powders, in any sample. All the XRD patterns exhibit a high background; therefore, we conclude that the samples contain a substantial amount of amorphous phase.

In the sample obtained from the suspension in acetone the orthorhombic and tetragonal PbO phases as well as $PbO \cdot 6PbCO_3 \cdot 3Pb(OH)_2$ are present. We could not determine any magnesium-containing compound, which can be due to the low mass fraction of magnesium compound in the PMN powder mixture.

The presence of $Mg(OH)_2$ in the dried mixture can be explained by the dissolution of the starting $(MgCO_3)_4{\cdot}Mg(OH)_2{\cdot}4H_2O$ upon milling, yielding Mg^{2+}, $Mg(OH)^+$ and CO_3^{2-} ions. It is possible that the CO_3^{2-} ions, originating from the $(MgCO_3)_4{\cdot}Mg(OH)_2{\cdot}4H_2O$, react with the soluble lead species $(Pb(OH)^+$, $Pb(OH)_2$ (aq) and $Pb(OH)_3^-)$ [115], yielding $PbO \cdot 6(PbCO_3) \cdot 3(Pb(OH)_2)$.

According to the XRD measurements all three dried samples have almost the same phase composition, regardless the starting pH of the suspension. The only difference is in the different PbO-to-$PbO \cdot 6(PbCO_3) \cdot 3(Pb(OH)_2)$ ratios for the samples with different starting pH.

The acetone sample still contains some orthorhombic PbO (massicot) with a preferred orientation $\{00\ell\}$, which we could not detect in the water-derived samples. Therefore, in acetone, the full massicot-to-litharge transformation does not occur. The amount of the $PbO \cdot 6(PbCO_3) \cdot 3(Pb(OH)_2)$ is lower in the acetone sample than in the samples prepared in water.

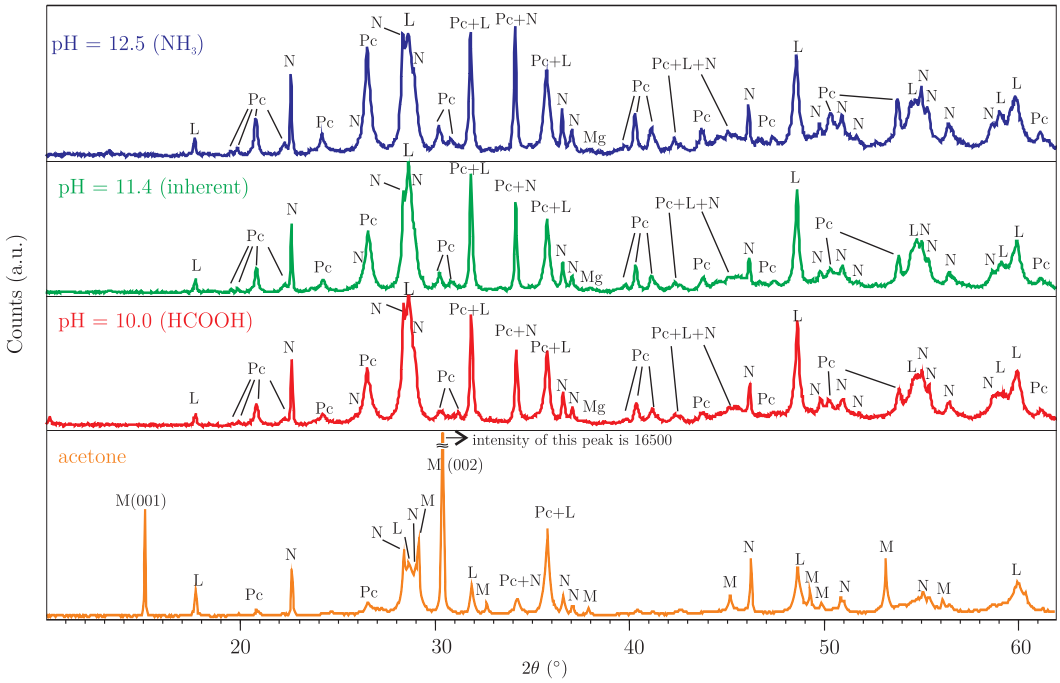

Figure 40: *Milling of the reagent powder mixtures.* XRD patterns of the powder mixtures of PbO, MHC and Nb_2O_5 with the stoichiometry corresponding to $Pb(Mg_{1/3}Nb_{2/3})O_3$ after attrition-milling in acetone and in aqueous medium with pH set at 10.0, 11.4, and 12.5. Mg - $Mg(OH)_2$, L - tetragonal PbO (litharge), M - orthorhombic PbO (massicot), N - Nb_2O_5, Pc - $PbO \cdot 6(PbCO_3) \cdot 3(Pb(OH)_2)$.

5.2.4 Morphology of the Dried Reagent Powder Mixtures

The particle size distributions of the dried powder mixtures determined by light scattering are narrow, with the average sizes equal to 0.37 μm, 0.42 μm and 0.40 μm for pH 10.0, 11.4, and 12.5, respectively, and the largest particles not exceeding 2 μm. The average size of the particles homogenized in acetone is 0.52 μm, with the largest particles being about 10 μm. The particle size is effectively decreased by attrition milling and the effect is more pronounced in water suspensions. For a comparison with the particle sizes of the starting powders see Table 2. Figure 41 shows the FE-SEM micrographs of the dried powders for pH 10.0, pH 11.4, pH 12.5, and acetone samples. All three water-derived samples consist of sub-micrometer particles. The acetone sample contains in addition to sub-micrometer particles, particles larger than 1 μm. This is consistent with the results obtained by light scattering, where the largest average particle size is measured in the acetone sample. The morphology and the size of the particles are similar in all three samples prepared in water, whereas the acetone sample differs from the others.

5.2.5 Thermal Decomposition of the Dried Reagent Powder Mixtures

To confirm and to further explain the influence of the suspension pH as well as the influence of the milling media on the composition of the samples we use thermal analysis. Thermogravimetric (TG) curves of the dried samples, prepared at pH 10.0, 11.4, 12.5, and the acetone samples, are presented in Figure 42. The detailed data of mass changes for all the samples are given in Table 6. All the samples prepared in water lose their

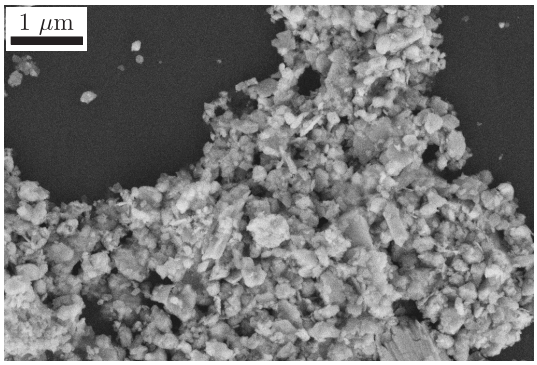

(a) FE-SEM pH = 10.0

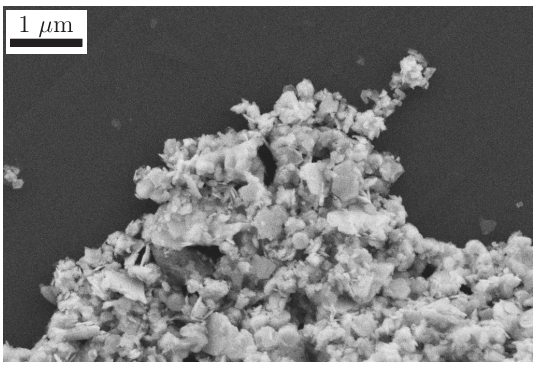

(b) FE-SEM pH = 11.4

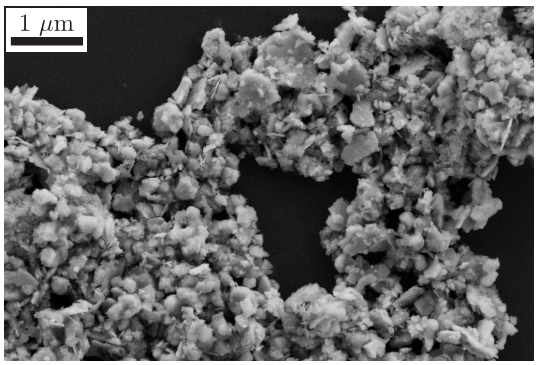

(c) FE-SEM pH = 12.5

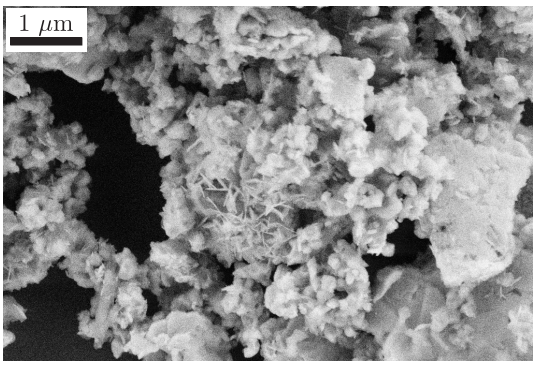

(d) FE-SEM acetone

Figure 41: *Micrographs of the dried reagent powder mixtures.* (a) pH = 10.0, (b) pH = 11.4, (c) pH = 12.5, and (d) acetone samples.

Table 6: *Mass changes of the dried reagent powder mixtures upon heating in air.*

Temp. range	pH 10.0	pH 11.4	pH 12.5	acetone
RT*-270 °C	−1.26%	−1.25 %	−1.24 %	−1.49 %
270-395 °C	−5.16 %	−4.57 %	−4.88 %	−2.61 %
395-475 °C	+0.62 %	+0.77 %	+0.79 %	−1.51 %
475-600 °C	−0.89 %	−1.07 %	−1.07 %	−0.45 %
600-750°C, 5h	−0.15 %	−0.19 %	−0.30 %	+0.00 %
total	−6.84 %	−6.31 %	−6.70 %	−6.06 %

*RT stands for room temperature.

mass in two steps between RT and 400 °C. The acetone sample behaves differently: it loses mass gradually between RT and 440 °C. We attribute these mass losses to the decomposition of the carbonate and hydroxide groups and adsorbed or incorporated water. The decomposition temperatures of the lead basic/hydrous carbonates and magnesium hydroxide are below 400 °C [116]. The presence of hydrous carbonates and hydroxides has been determined in the as-dried PMN samples by XRD analysis, see Figure 40.

Between 400 and 500 °C the samples from aqueous suspensions gain approximately 1 % of mass and then the same mass loss is observed to about 600 °C. A mass gain is not observed in the acetone sample, which loses mass upon heating to 600 °C.

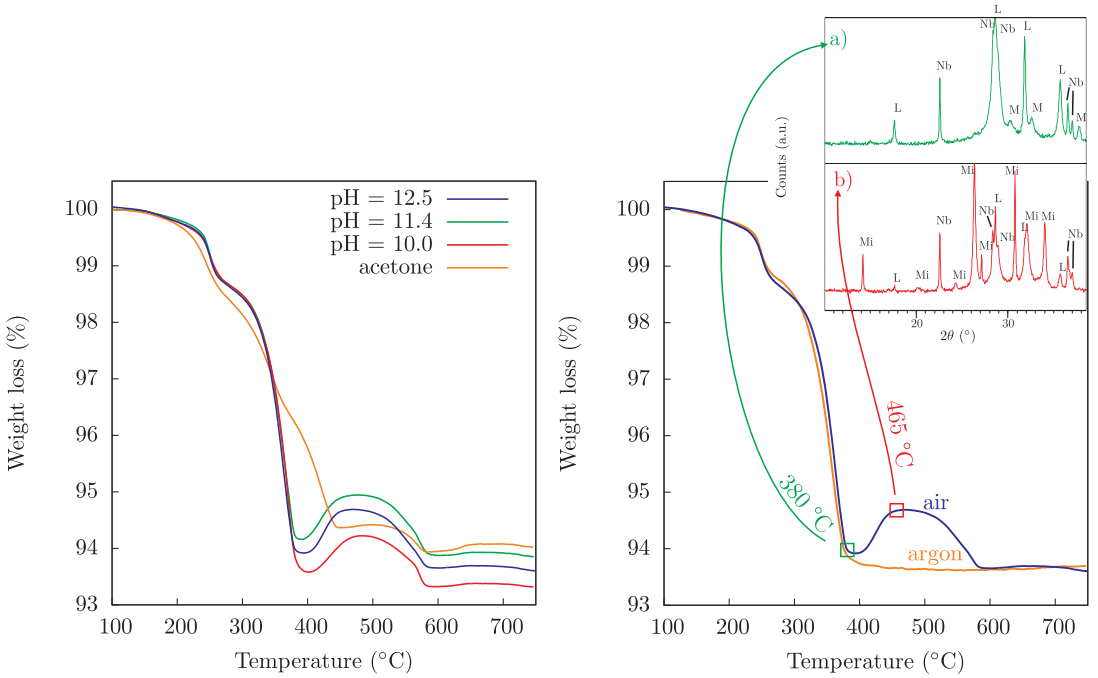

(a) TGA in air (b) TGA in air and argon

Figure 42: *Thermogravimetric analysis of the dried reagent powder mixtures.* (a) Thermal decomposition of the pH10.0, pH11.4, pH12.5, and acetone samples in air. (b) Thermal decomposition of the pH12.5 sample in air and argon. The inset shows the XRD patterns of the pH12.5 sample quenched at 365 °C and 480 °C in air. All the samples are heated in air with 2 K/min.

Similar thermal decompositions of all three samples from aqueous suspensions again confirm only minor differences in the phase composition of the dried samples determined by XRD. The phase composition of the acetone sample is different, which also results in a different thermal decomposition.

The pH 12.5 and pH 10.0 samples have slightly higher mass losses than the inherent pH (11.4) sample and the acetone sample. We attribute this difference to the reaction of the powders with the ammonia solution and the formic acid, which are used to adjust the pH, forming hydroxyl and formate groups. However, formate is not found in the XRD patterns, probably due to its very low quantity in the sample.

The mass gain between 390 °C and approx. 450 °C followed by an almost equal mass loss within a further 100 °C is observed in all water-derived samples. In order to explain this effect, which is obviously connected to oxidation/reduction, we quench the pH 12.5 sample at 380 °C and at 465 °C. The XRD spectra of the samples are included in Figure 42b. The sample heated at a lower temperature contains Nb_2O_5 and PbO (litharge and massicot) on the amorphous background. The sample heated at 465 °C contains Nb_2O_5, tetragonal PbO (litharge) and Pb_3O_4 (minium, PDF 08-0019). Clearly, lead (II) oxide partially oxidized to Pb_3O_4. According to the Pb-O equilibrium [117], lead(II) oxide is partially oxidized upon heating in air to lead (II, IV) oxide and at about 600 °C reduced again to lead(II) oxide. By performing the TG analysis of the pH12.5 sample in argon, the mass gain due to the the partial oxidation of PbO is avoided (Figure 42b).

5.3 Synthesis of PMN

5.3.1 Phase Evolution of the Reagent Powder Mixtures Upon Heating

We heat the reagent powder mixtures, prepared in water at pH 10.0, 11.4, and 12.5, and in acetone with a heating rate of 2 K/min at 500–900 °C for 5 h in air. The phase composition of the pH10.0, pH11.4 and acetone samples as determined by XRD is very similar; therefore, only the results for the pH11.4 and pH12.5 samples are presented here. The XRD patterns of the powders prepared at pH = 11.4 are collected in Figure 43. After heating at 500 °C, the pyrochlore (indexed as $Pb_{1.83}Nb_{1.71}Mg_{0.29}O_{6.39}$, PDF 37-

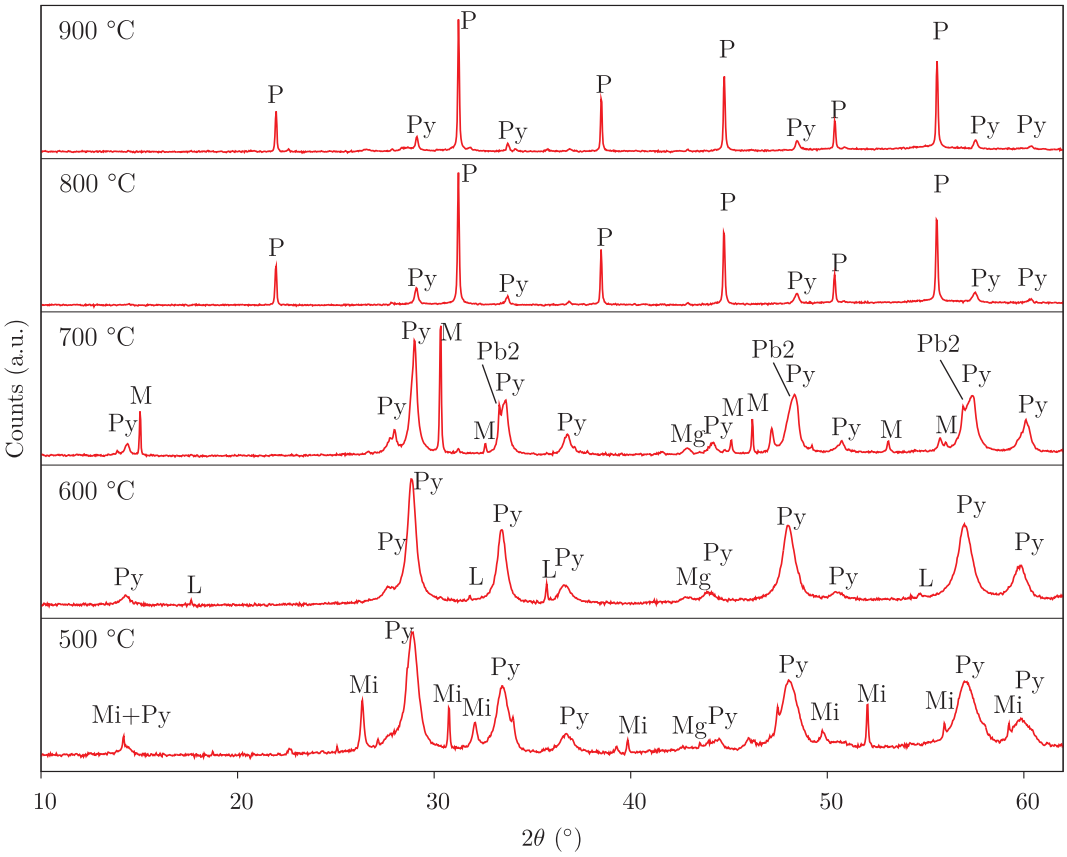

Figure 43: *Phase evolution of the pH11.4 sample.* XRD patterns of the reagent powder mixtures with inherent pH (11.4) of the suspension heated at 500 °C, 600 °C, 700 °C, 800 °C, 900 °C for 5h. Notice that square root intensity scale is used. Mi - minium Pb_3O_4, M - orthorhombic PbO (massicot), L - tetragonal PbO (litharge), Pb2 - cubic PbO_2, P - perovskite $Pb(Mg_{1/3}Nb_{2/3})O_3$, Mg - MgO, Nb - Nb_2O_5, Py - pyrochlore $Pb_{1.83}Nb_{1.71}Mg_{0.29}O_{6.39}$.

0071), Pb_3O_4 (minium, PDF 08-0019), and MgO (PDF 04-0829) are present. The XRD pattern of the powder heated at 600 °C contains pyrochlore, MgO, and a minor amount of tetragonal PbO phase. The powder heated at 700 °C contains pyrochlore, MgO, orthorhombic PbO, and a phase that matches the reflections of the cubic PbO_2 (PDF 22-0389). Haines et al. reported that cubic PbO_2 is stable only at pressures above 7 GPa [118]; therefore, we conclude that another phase with a similar structure is present in our sample. Upon further heating at 800 °C the powder contains the perovskite phase (PDF 01-081-0861) and also a small amount of the pyrochlore phase (PDF 37-0071).

At 900 °C the pyrochlore phase is still present.

Figure 44 shows the XRD patterns of the powders prepared at pH 12.5. In the pow-

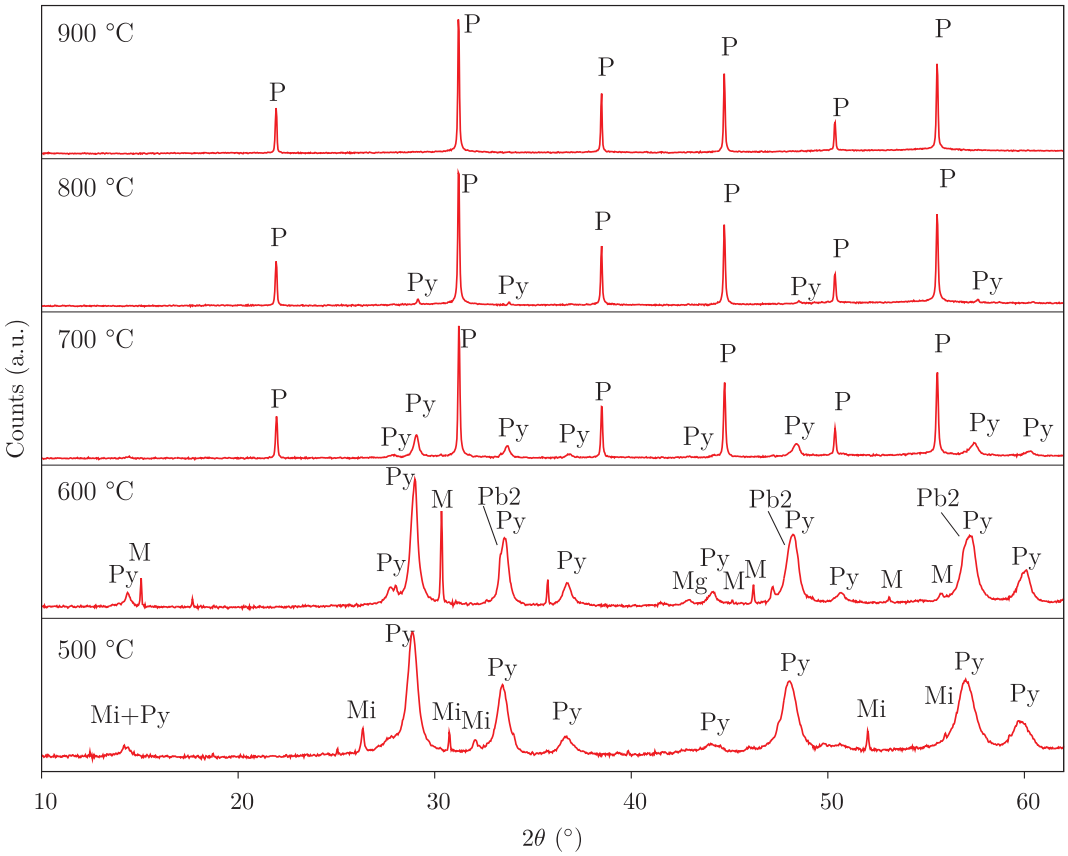

Figure 44: *Phase evolution of the pH12.5 sample.* XRD patterns of the reagent powder mixtures with inherent pH (11.4) of the suspension heated at 500 °C, 600 °C, 700 °C, 800 °C, 900 °C for 5h. Notice that square root intensity scale is used. Mi - minium Pb_3O_4, M - orthorhombic PbO (massicot), L - tetragonal PbO (litharge), Pb2 - cubic PbO_2, P - perovskite $Pb(Mg_{1/3}Nb_{2/3})O_3$, Mg - MgO, Nb - Nb_2O_5, Py - pyrochlore $Pb_{1.83}Nb_{1.71}Mg_{0.29}O_{6.39}$.

der heated at 500 °C, pyrochlore, and Pb_3O_4 (minium) phases are present. The pattern of the powder heated at 600 °C contains reflections of pyrochlore, MgO, orthorhombic PbO and peaks indexed as cubic PbO_2. The perovskite phase is first detected in the powder heated at 700 °C, together with a small amount of pyrochlore phase. With increasing the annealing temperature, the amount of the pyrochlore phase decreases and the powder heated at 900 °C contains a pure perovskite phase.

The phase compositions of the two samples upon heating at 500 °C are very similar; both samples contain pyrochlore and Pb_3O_4 (minium). The transient presence of minium in the powder mixtures can be explained as a partial oxidation of lead (II) oxide to lead (II, IV) oxide at about 475 °C and its subsequent reduction to lead (II) oxide at about 600 °C, as confirmed by thermogravimetric analysis. It has been reported in [119] that with the use of minium as a lead source pyrochlore-free PMN ceramics can be synthesized. However, probably due to a small amount of transient minium in our samples (Figures 43 and 44) this is not the case. The pH 11.4 sample, although containing minium at 500 °C, still contains pyrochlore after heating at 900 °C.

A noticeable difference between the two samples is observed at 700 °C, where the

pH12.5 sample already contains perovskite, with only a small amount of the pyrochlore phase, whereas in the pH 11.4 sample the main constituent is still the pyrochlore phase and no perovskite is detected. At 900 °C the unwanted pyrochlore phase is totally eliminated in the pH12.5 sample, whereas it is still present in the pH11.4 sample.

The of XRD patterns of pH12.5, pH11.4, pH10.0 and the acetone samples calcined at 900 °C are collected in Figure 45. In the pH12 sample only reflections of the perovskite

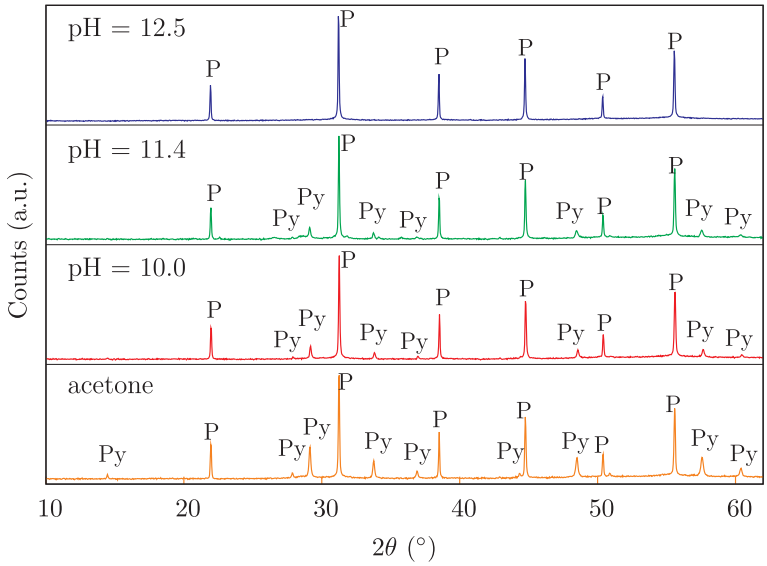

Figure 45: *XRD patterns of the pH12.5, pH11.4, pH10.0 and acetone samples calcined at 900 °C.* P - perovskite $Pb(Mg_{1/3}Nb_{2/3})O_3$, Py - pyrochlore $Pb_{1.83}Nb_{1.71}Mg_{0.29}O_{6.39}$. Note that square root intensity scale is used.

$Pb(Mg_{1/3}Nb_{2/3})O_3$ phase (PDF 01-081-0861) are observed. In contrast in the other three samples in addition to the perovskite also the pyrochlore phase (PDF 37-0071) is present. The mass fractions of the pyrochlore and perovskite phases in all samples heated at 900 °C are calculated using the Rietveld method. The pH12.5 sample contains only the perovskite phase. The amount of pyrochlore in the pH10.0 and pH11.4 samples is approx. 5 mass %, whereas the acetone sample contains 17 mass % of pyrochlore.

The cell parameters of the pyrochlore and perovskite phases in the pH11.4 and pH12.5 powder mixtures heated between 600 °C and 900 °C are calculated. The results are collected in Table 7. The cell parameter of the pyrochlore phase in the pH11.4 powder

Table 7: *Cell parameters of the pyrochlore and perovskite phases in the powders prepared at pH = 11.4 and pH = 12.5 after heating between 600 °C and 900 °C for 5 h.*

	$a_{pyrochlore}$ (nm)		$a_{perovskite}$ (nm)	
T (°C)	pH 11.4	pH 12.5	pH 11.4	pH 12.5
600	1.070(5)	1.066(1)	no perovskite	no perovskite
700	1.065(8)	1.063(8)	no perovskite	0.4049(1)
800	1.062(4)	1.060(5)	0.4048(1)	0.4048(2)
900	1.061(9)	no pyrochlore	0.4047(4)	0.4047(0)

heated at 600 °C is equal to 1.070(5) nm and with increasing temperature it decreases, reaching the value of 1.061(9) nm at 900 °C. The cell parameters of the pyrochlore phase in the pH12.5 sample in the studied temperature range are systematically smaller than those in the pH11.4 powder. We conclude that the pyrochlore phases in the two samples have different compositions, and further, that the chemical composition of the pyrochlore phases changes with temperature. A similar effect was observed by Kuščer et al. in a study of the mechanochemical synthesis of PMN [36], where the pyrochlore phase cell parameter decreased with increasing milling time. In contrast, the perovskite phase is cell parameter has almost the same value in both pH11.4 and pH12.5 samples at individual temperatures. A slight decrease of the unit-cell parameter with increasing temperature is observed, from 0.4048 nm to 0.4047 nm for 800 °C and 900 °C, respectively. We conclude that the chemical composition of the perovskite phase in the two samples is identical.

5.3.2 Morphology of the Calcined Powders

Figure 46 shows the FE-SEM micrographs of the pH10.0, pH11.4, pH12.5, and acetone powders heated at 900 °C. The morphology of the powders strongly depends on the

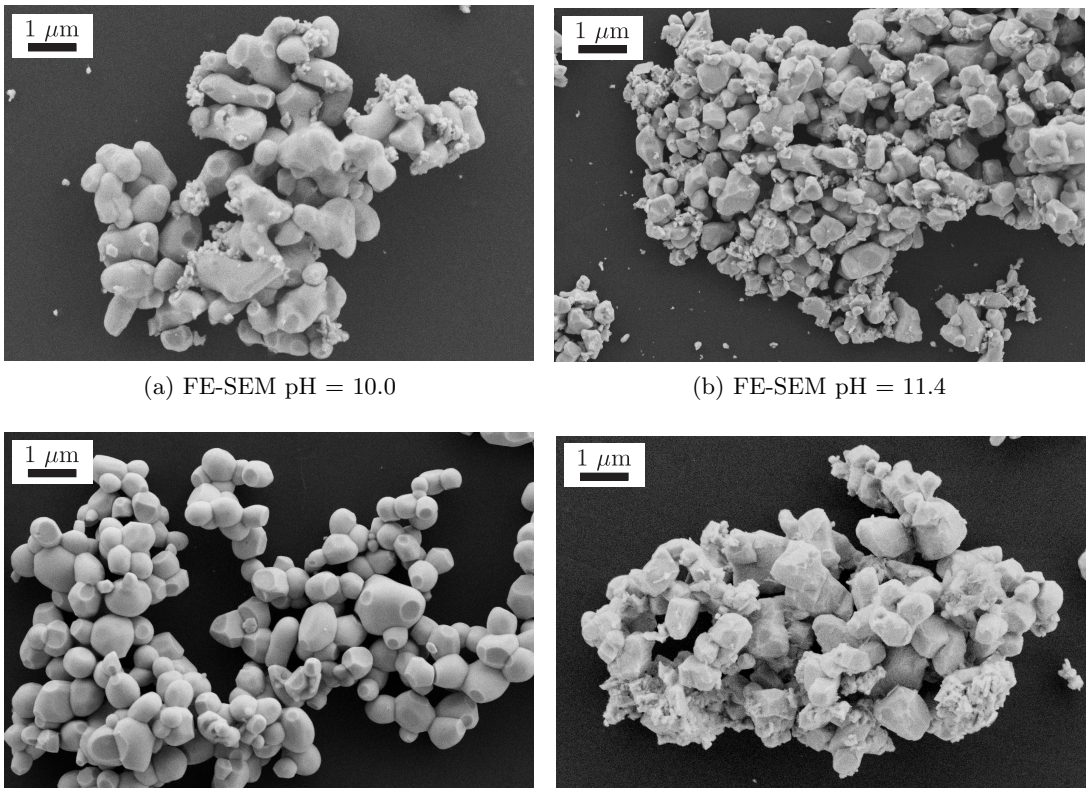

(a) FE-SEM pH = 10.0

(b) FE-SEM pH = 11.4

(c) FE-SEM pH = 12.5

(d) FE-SEM acetone

Figure 46: *Micrographs of the powders calcined at 900 °C.* (a) pH = 10.0, (b) pH = 11.4, (c) pH = 12.5, and (d) acetone samples.

suspension pH, and on the milling media, see Figure 46. The particles in the pH12.5 powder are uniform in size, about 1 μm, and in shape, also smaller particles of a few hundred nanometers are present in the sample, but they have the same spherical shape as the larger the particles. In contrast, the pH10.0, pH11.4, and acetone powders contain

in addition to micron-sized particles, smaller particles with sizes from 100 nm to few hundred nanometers with a different morphology. The largest amount of smaller particles with a different morphology is observed in the acetone sample, which also contains the largest amount of pyrochlore phase according to the XRD. Thus the presence of these particles could be connected to the pyrochlore phase. This is further investigated with transmission electron microscopy. In Figure 47, TEM micrographs of the pH11.4 sample heated at 900 °C for 5 h are presented. The TEM micrograph reveals the parti-

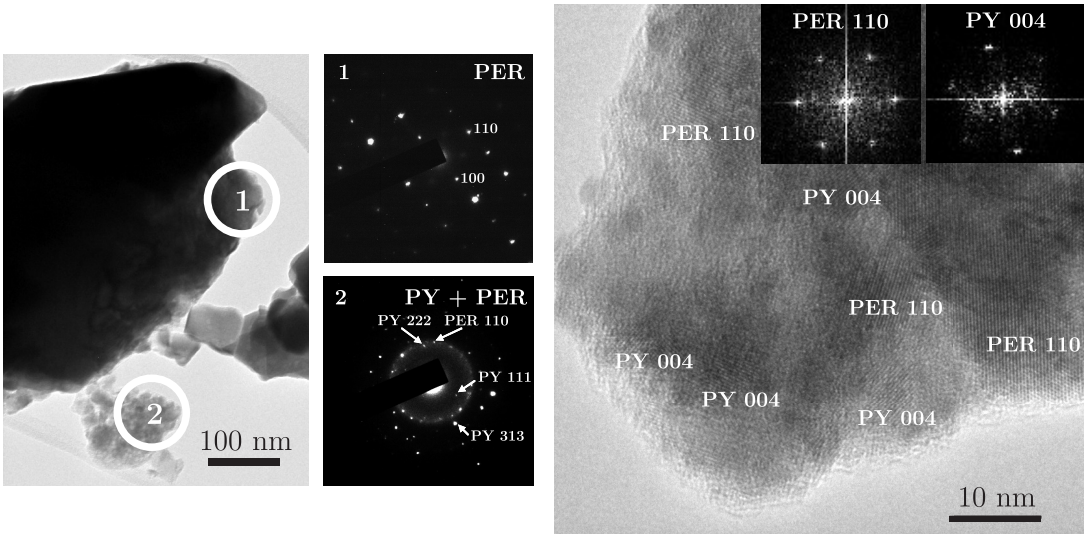

(a) TEM (b) HR-TEM

Figure 47: *TEM analysis of the pH11.4 sample calcined at 900 °C.* (a) TEM micrograph of the pH 11.4 powder heated at 900 °C for 5 h (left). Electron diffraction patterns of the area 1 and 2 (right). (b) HR-TEM image of the smaller agglomerate particle in the pH11.4 sample heated at 900 °C for 5 h.

cles with a diameter of a few nm and much larger particles. The electron diffraction is performed at the edge of the larger particle (area 1) and also on the agglomerate of the smaller particles (area 2). The larger particle has the perovskite structure, while the agglomerate contains both perovskite and pyrochlore phases. To get a further insight into the structural details of the smaller agglomerate, a high-resolution TEM (HR-TEM) is used. The HR-TEM image in Figure 47b reveals that the pyrochlore and perovskite phases are finely distributed in the agglomerate on the scale of a few nm.

5.4 Properties of the Ceramics

5.4.1 Phase Composition and Density of the Ceramics

The powders prepared at pH = 10.0, pH = 11.4, pH = 12.5, and the powder prepared in acetone and annealed at 900 °C for 5 h are pressed into pellets *without any milling* and sintered at 1000 °C and 1050 °C for 2 h. The pH 12.5 sample is also sintered at 950 °C. Note that the choice to use the as-calcined powders is intentional: we wanted to distinguish the difference between the powders. The densities of the sintered ceramics are presented in Table 8 together with the mass fractions of the pyrochlore and perovskite phases determined from the Rietveld refinement of the XRD patterns. The

Table 8: *Mass fraction of the pyrochlore and perovskite phase and relative density of the pellets sintered at 950 °C, 1000 °C, and 1050 °C for 2 h.*

	Sample			
Temperature	pH 10.0	pH 11.4	pH 12.5	acetone
950 °C	/	/	100 % Per 0 % Py $\rho_r = 95$ %	/
1000 °C	> 99 % Per 1 % Py $\rho_r = 90$ %	>99 % Per 1 % Py $\rho_r = 85$ %	100 % Per 0 % Py $\rho_r = 95$ %	93 % Per 9 % Py $\rho_r = 90$ %
1050 °C	> 99 % Per <1 % Py $\rho_r = 94$ %	>99 % Per <1 % Py $\rho_r = 89$ %	100 % Per 0 % Py $\rho_r = 95$ %	93 % Per 7 % Py $\rho_r = 92$ %

Per – Perovskite
Py – Pyrochlore

PMN ceramics prepared from the pH 12.5 powder reach 95 % of theoretical density (TD) at as low as 950 °C, and with increasing the temperature to 1050 °C we observe no further increase in density. The ceramics consist in all cases of a single perovskite phase. Note that in most literature reports the sintering temperature of about 1200 °C is used to reach 95 % of TD for the PMN ceramics [103, 104, 105, 106, 107].

The PMN ceramics prepared from the pH10.0, pH11.4 and acetone powders and sintered at 1000 °C reach between 85 % and 90 % of TD. They all consist of a mixture of perovskite and pyrochlore phases and the amount of the latter in the acetone sample is as high as 9 % .

Upon heating at 1050 °C the ceramics reach densities between 89 % and 94 % of TD. All the samples still contain a pyrochlore phase, which is in traces in the pH10.0 and pH11.4 samples and in the amount of 7 % in the acetone sample.

5.4.2 Microstructure of the Ceramics

The fracture surface of the PMN ceramics prepared from the pH12.5 powder, sintered at 950 °C, is shown in Figure 48. It reveals a homogeneous microstructure of equiaxed grains with a predominant intergranular fracture mode. The grain size is estimated to be between 2 μm and 8 μm.

The polished surfaces of the PMN ceramics, prepared from all the powders, and sintered at 1050 °C, are collected in Figure 49. The pH10.0 and pH12.5 samples exhibit a uniform distribution of fine pores, corresponding to the achieved high relative densities of 94 % and 95 % . The amount of porosity in the pH11.4 and the acetone samples is higher, in agreement with the about 90 % TDs of the two samples. The distribution of porosity is in both cases non-homogeneous and explained as a consequence of the presence of agglomerates in the powders.

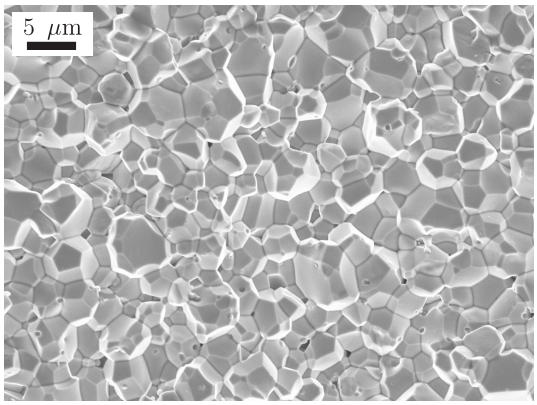

Figure 48: *FE-SEM micrograph of the fracture surface of the pH12.5 sample sintered at 950 °C.*

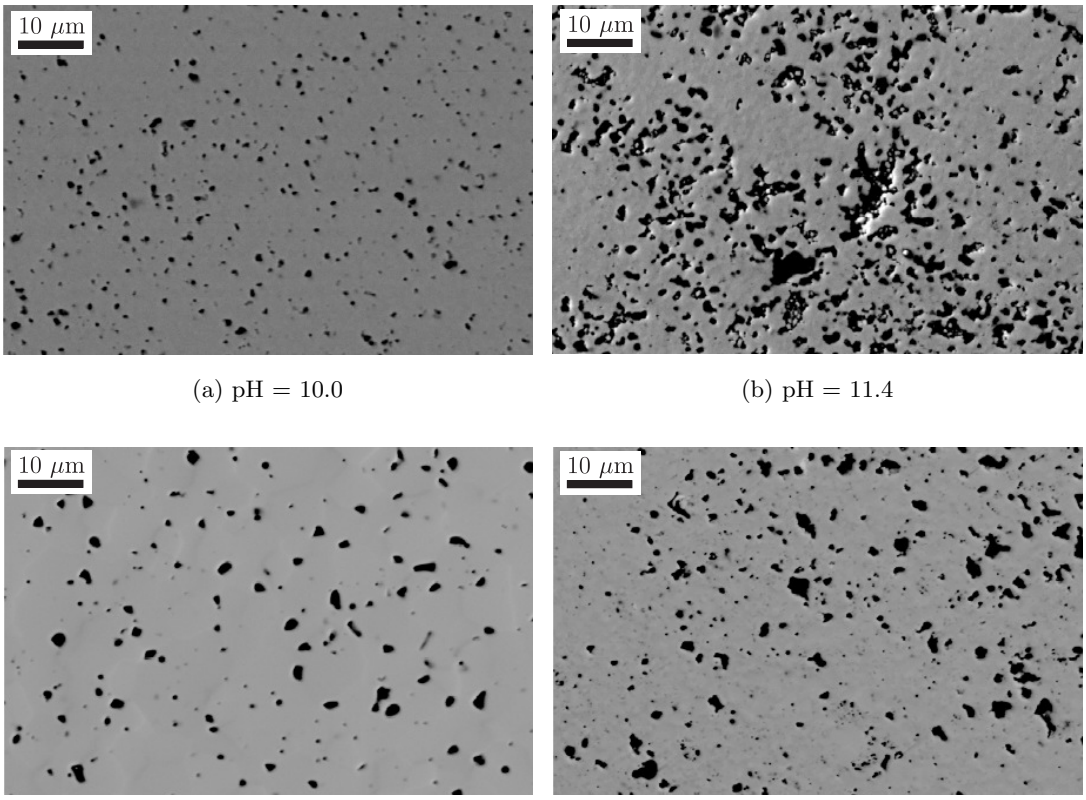

(a) pH = 10.0 (b) pH = 11.4

(c) pH = 12.5 (d) acetone

Figure 49: *SEM micrographs of the polished surfaces of the PMN ceramics sintered at 1050 °C for 2 h.* (a) pH = 10.0, (b) pH = 11.4, (c) pH = 12.5, and (d) acetone samples.

5.4.3 Dielectric and Electrostrictive Properties of the Ceramics

Dielectric permittivity and dielectric loss factor of the sintered samples as a function of temperature and frequency in the 1–100 kHz range are measured. As all the samples contain the perovskite PMN phase, they all exhibit a typical relaxor behavior, see Figure 50.

The peak dielectric permittivities of the ceramics sintered between 950 °C and

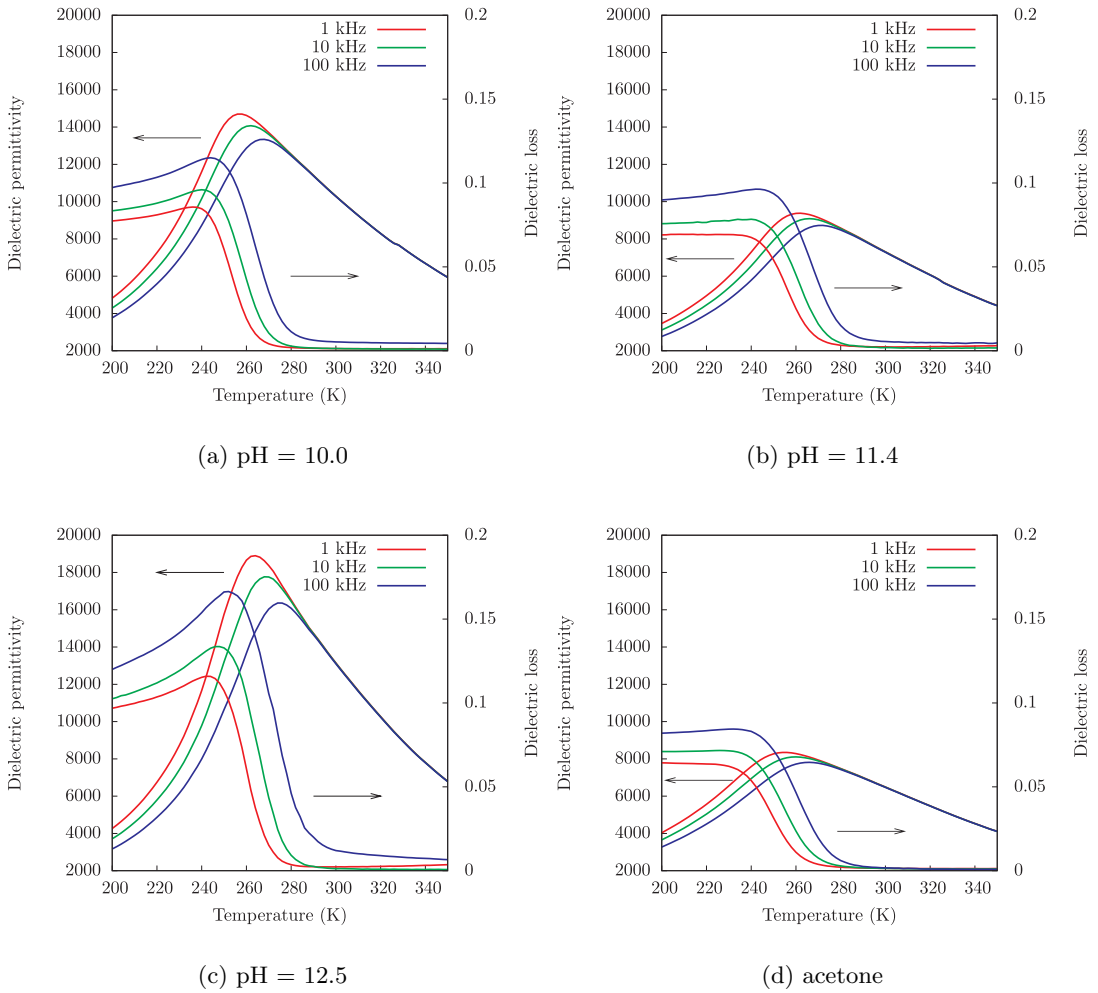

(a) pH = 10.0 (b) pH = 11.4

(c) pH = 12.5 (d) acetone

Figure 50: *Dielectric permittivity and loss as a function of temperature of the PMN ceramics sintered at 1050 °C for 2 h.* (a) pH = 10.0, (b) pH = 11.4, (c) pH = 12.5, and (d) acetone samples.

1050 °C are collected in Table 9. The densities of the samples and the amount of

Table 9: *Peak and room temperature dielectric permittivity (ε_r) at 1 kHz of the ceramics sintered at 950 °C, 1000 °C, and 1050 °C for 2 h.*

	Sample			
$T_{sintering}$	pH 10.0	pH 11.4	pH 12.5	acetone
950 °C	–	–	**19100/13900**	–
1000 °C	10900/8600	8500/6800	**18400/13400**	8300/6800
1050 °C	14500/10900	9000/6900	**19100/13600**	8200/6800

Peak/RT dielectric permittivities are given in the table.

the pyrochlore phase in the samples (Table 8) can be correlated to their electrical properties (Table 9). The acetone samples sintered at 1000 °C and 1050 °C contain the

largest amount of pyrochlore phase. Thus, the peak dielectric permittivities of these two samples are lower in comparison to the others. Similarly, the peak permittivities of the pH10.0 and pH11.4 ceramics are lower than the value obtained for the pH12.5 ceramics. The pH12.5 PMN ceramics sintered at 950–1050 °C exhibit the peak dielectric permittivity, exceeding 18 000 at 1 kHz, whereas the peak permittivities of all the other samples are always lower than 15 000 at 1 kHz.

The peak dielectric permittivitiy of the pH12.5 ceramics is at the high end of the values reported in the literature for ceramics produced by different methods (Table 10). Note that our material is sintered an at least 250 K lower temperature than the ceramics

Table 10: *Peak dielectric and room temperature permittivities (ε_r) at 1 kHz and densities of the PMN ceramics prepared by different methods reported in the literature.*

Authors	Method	Sintering	ρ_{rel}	ε_r @ 1 kHz
Wang et al. [104]	Columbite MgO excess	1200 °C	98 %	18400/11800
Swartz et al. [103]	Columbite	1270 °C	93 %	16400/11000
Lu et al. [119]	Reactive sintering Pb_3O_4 – lead source	950 °C	96 %	15400/11500
Lu et al. [119]	Reactive sintering PbO – lead source	950 °C	95 %	10300/8000
Gu et al. [40]	Coating method, reactive sintering	1000 °C	95 %	15600/11700*
This work	Controlled agglomeration (pH 12.5)	950 °C	95 %	19100/13900

*Measurement frequency is not given. Peak/RT dielectric permittivities are given in the Table.

reported in the first two rows of Table 10 and it still maintains a high dielectric permittivity. In the cases where a comparable sintering temperature was used the achieved permittivity was lower than for our pH12.5 ceramics.

To further evaluate the properties of the ceramics prepared under different conditions, the electrostrictive properties of the samples are measured. It is well-known that the PMN material exhibits a large electrostrictive response, and can be used for actuator applications. The strain is measured as a function of the applied electric field on the pH10.0, pH11.4, pH12.5 and acetone samples. The results are collected in Figure 51. All the samples show a quadratic relation between the strain and the electric field, which is in accordance with the following equation

$$s_{33} = M_{33} E_3^2 \,, \tag{5.1}$$

where s is the strain, M is the electrostriction coefficient, and E is the applied electric field. The data shown in Figure 51 are fitted to a quadratic function and from the fit

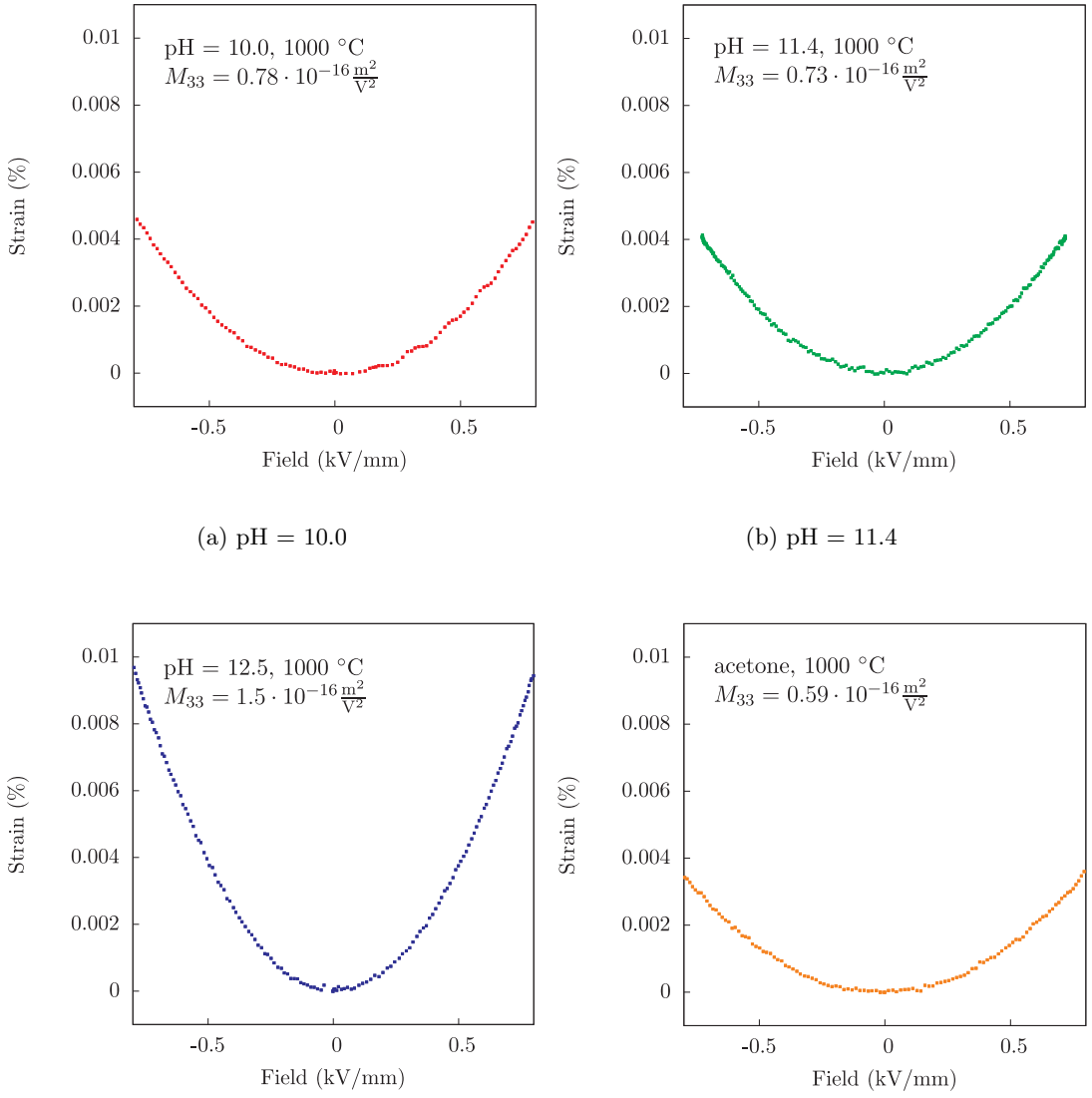

(a) pH = 10.0

(b) pH = 11.4

(c) pH = 12.5

(d) acetone

Figure 51: *Strain as a function of the applied electric field for the samples sintered at 1000 °C for 2 h.* (a) pH = 10.0, (b) pH = 11.4, (c) pH = 12.5, and (d) acetone samples.

the M_{33} values are calculated (Table 11). The highest response is observed in the pH 12.5 sample; hence this sample also has the largest M_{33} coefficient. The M_{33} coefficient

Table 11: *Electrostrictive properties of PMN samples prepared at different conditions.* M_{33} coefficient in $10^{-16} \frac{m^2}{V^2}$ measured at RT and 100 Hz of sine input signal.

	Sample			
	pH 10.0	pH 11.4	pH 12.5	acetone
950 °C	/	/	1.4 ± 0.1	/
1000 °C	0.78 ± 0.04	0.73 ± 0.06	1.5 ± 0.1	0.59 ± 0.03

for the pH12.5 samples sintered at 950 °C and 1000 °C are $1.4 \cdot 10^{-16} \frac{\mathrm{m}^2}{\mathrm{V}^2}$ and $1.5 \cdot 10^{-16} \frac{\mathrm{m}^2}{\mathrm{V}^2}$, respectively. These values are comparable to the literature, *i.e.*, the highest electrostrictive coefficient for PMN ceramics is reported to be $M_{33} = 1.5 \cdot 10^{-16} \frac{\mathrm{m}^2}{\mathrm{V}^2}$ [120]. Similar to the dielectric, the electrostrictive properties of the pH 12.5 sample are superior in comparison to the other samples. The electrostrive coefficients of the pH10.0, pH11.4, and acetone samples are at least half lower than the M_{33} values obtained for the pH12.5 sample. This can be explained by the presence of the pyrochlore phase and the lower densities of the samples prepared at lower pH and in acetone.

5.5 Summary

We have synthesized a pyrochlore-free PMN powder from an aqueous suspension containing PbO, Nb_2O_5 and $(MgCO_3)_4 \cdot Mg(OH)_2 \cdot 4H_2O$ powders, in a single annealing step. The zeta-potential measurements showed that at pH = 12.5, PbO and Nb_2O_5 are both negatively charged and thus repelled, whereas the hydromagnesite is positively charged. This enables the formation of hetero-agglomerates, as shown with computer simulations, where the hydromagnesite particles prevent direct contacts between the lead and niobium oxide particles. Simulations show that there are fewer PbO-Nb_2O_5 contacts in the dried suspension with pH = 12.5 than in the case where PbO and Nb_2O_5 particles have opposite surface charges and are thus attracted, *i.e.*, at pH = 10.0 and pH = 11.4. The arrangement of the particles in the pH12.5 sample is more favorable for the perovskite formation due to the separation of the PbO and Nb_2O_5 particles and a more homogeneous distribution of hydromagnesite particles. A single calcination step at 900 °C is therefore sufficient for the synthesis of the pyrochlore-free PMN powder. On the other hand, the powders prepared from the pH10.0, pH11.4 and acetone suspensions contain the pyrochlore phase.

We have produced dense $Pb(Mg_{1/3}Nb_{2/3})O_3$ ceramics from the pH12.5 powders calcined at 900 °C by sintering at 950 °C with dielectric properties comparable to the values obtained in ceramics sintered at about 250 K higher temperatures.

In summary, by applying the controlled agglomeration method the phase-pure $Pb(Mg_{1/3}Nb_{2/3})O_3$ powders and dense ceramics were prepared from simple materials in only one milling, one calcination and one sintering step. We believe that the presented synthesis approach is general, and it could be implemented for the synthesis of other complex perovskite materials.

6

Synthesis of PMN–PT from Aqueous Suspensions

Controlled Agglomeration for PMN–PT Synthesis

In this Chapter we further extend our method of the controlled agglomeration of reagent particles to the synthesis of PMN-PT. The idea is the same as the one presented for the PMN synthesis. By controlling the pH we try to control the formation of the agglomerates in the suspensions of reagent particles and consequently influence the solid-state reactions. We chose the same pH conditions as in the case of PMN and we propose the structure of the agglomerates based on the zeta-potential measurements. Then we calcine the dried reagent powder mixtures obtained from suspensions with two different pH values. Finally, we prepare the ceramics from the two samples and compare their material and electrical properties.

6.1 Introduction

The $(1-x)$Pb$(Mg_{1/3}Nb_{2/3})O_3$–xPbTiO$_3$ ($(1-x)$PMN-xPT) relaxor-ferroelectric materials are known to exhibit excellent piezoelectric and dielectric properties and are used as high-strain actuators or high-permittivity capacitors [8, 12, 13, 14]. Recently, a large electro-optic effect has been measured in 0.75PMN-0.25PT, which makes this material a possible alternative to the conventionally used (Pb,La)(Zr,Ti)O$_3$ (9/65/35) for electro-optic applications [11]. The morphotropic phase boundary (MPB) in the $(1-x)$PMN-xPT system is located near $x \approx 0.35$ [6]. Extremely high piezoelectric d_{33} coefficients of around 1200 pC/N and 700 pC/N have been measured in 0.65PMN-0.35PT single crystals [10] and ceramics [6, 7], respectively.

The PMN-PT ceramics should be single phase to achieve the desired properties. However, like in the PMN case, the conventional solid-state synthesis using the simultaneous mixing of constituent oxides usually yields, in addition to the perovskite, the pyrochlore phases. The latter deteriorate the dielectric, ferroelectric and piezoelectric properties of the perovskite PMN-PT. In the case of PMN synthesis Swartz and Shrout prepared pyrochlore-free powder by introducing the *columbite* method [18], as already explained in the previous chapters. This method has also been successfully modified for the $(1-x)$PMN-xPT synthesis [6, 19, 20]. Here, in the second step both PbO and TiO$_2$ are added to the $MgNb_2O_6$ to form the reaction mixture. Although the columbite method is the most widely used for the synthesis of PMN-based materials, also other

approaches have been developed, usually with the aim of avoiding the additional calcination step, see the Introduction Chapter.

In the previous Chapter we introduced a new approach to the synthesis of $Pb(Mg_{1/3}Nb_{2/3})O_3$ by the controlled agglomeration of the reagent particles. As is shown with the MC simulations the pH has a great influence on the agglomeration process of the reagent particles. Experimentally we find that the pH of the suspension containing reagent particles also influences the solid-state reactions and consequently the properties of the PMN ceramics. We adopt the same approach for the synthesis of the $0.65Pb(Mg_{1/3}Nb_{2/3})O_3$–$0.35PbTiO_3$ material. The idea is to tune the interactions between the particles so that colloidal agglomerates are formed without contacts between the PbO and Nb_2O_5, which should minimize the reaction to the binary Pb-Nb pyrochlore formed at lower temperature. Furthermore, the homogeneous distribution of Mg- and Ti-species should be achieved for effective solid-state reactions.

6.2 Interactions between the Particles

The zeta-potentials are measured for four starting compounds, *i.e.*, PbO, Nb_2O_5, TiO_2, and $(MgCO_3)_4{\cdot}Mg(OH)_2{\cdot}4H_2O$ (MHC), as a function of pH. The results are collected in Figure 52. Both Nb_2O_5 and TiO_2 particles exhibit positive zeta-potentials at low

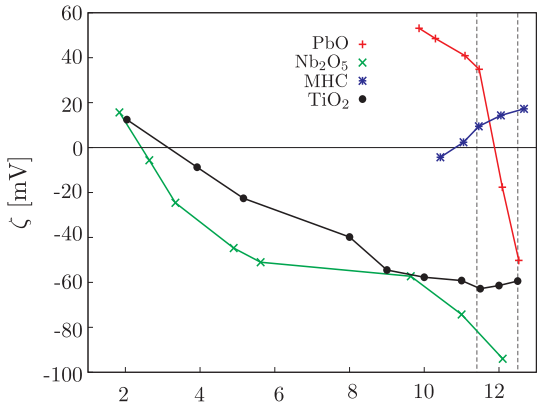

Figure 52: *Zeta-potential of the as-received constituent powders for the PMN-PT synthesis in dependence on the suspension pH.*

pH values and the zeta-potential is decreasing with increasing pH in both cases. The isoelectric points (IEP) for Nb_2O_5 and TiO_2 are at pH = 2.4 and 3.2, respectively. At high pH values both powders are negatively charged: the zeta-potential of Nb_2O_5 at pH = 12 equals −85 mV, while the zeta-potential of TiO_2 is −60 mV.

The zeta-potential of PbO can be measured only above pH = 10, due to its high solubility at lower pH. The zeta-potential of PbO particles also decreases with increasing pH. Its IEP is considerably higher in comparison to Nb_2O_5 and TiO_2, and it is at pH 11.8. At pH = 10 and 12.5 the values for the PbO are +40 mV and −50 mV, respectively. The results are in agreement with the literature [42, 111].

In contrast to all the other starting compounds the zeta-potential of MHC is increasing with increasing pH, reaching +20 mV at pH = 12.5. This behavior is explained in the previous Chapter.

From these measurements it is possible to estimate the electrostatic interactions between the pairs of particles in the suspension and consequently propose the structure of the agglomerates, which should form under certain pH conditions. We consider two

experimental conditions at which the particles are differently charged, *i.e.*, pH = 11.4 and pH = 12.5. At pH = 11.4, Nb_2O_5 and TiO_2 are negatively charged, whereas PbO and MHC are positively charged. Due to the opposite charges of the PbO and Nb_2O_5, and the PbO and TiO_2 particles we expect the formation of agglomerates with the PbO-Nb_2O_5 and PbO-TiO_2 contacts. Such a configuration of particles is favorable for the binary Pb-Nb pyrochlore and $PbTiO_3$ intermediate phases formation before the single perovskite PMN-PT phase is formed. In contrast, at pH = 12.5, PbO, Nb_2O_5 and TiO_2 are negatively charged, while the MHC surface is still positive. Here we expect repulsion between the PbO, Nb_2O_5 and TiO_2, consequently the agglomerates where MHC separates PbO and Nb_2O_5, and PbO and TiO_2 particles, respectively, should form. The pH = 12.5 conditions should therefore retard the formation of intermediate phases and thus be more favorable for the formation of the pure perovskite phase formation in comparison to the pH = 11.4 conditions.

The pH conditions chosen for the experiments are the same as in the synthesis of $Pb(Mg_{1/3}Nb_{2/3})O_3$, because we expect a similar mechanism of agglomerate formation also in the $0.65Pb(Mg_{1/3}Nb_{2/3})O_3$–$0.35PbTiO_3$ example. At lower pH, *i.e.*, pH 11.4, the clusters with undesired PbO-Nb_2O_5 contacts should form, whereas at pH = 12.5 the PbO and Nb_2O_5 particles should be separated by positively charged MHC particles in both PMN and PMN-PT cases.

6.3 Synthesis of PMN-PT

6.3.1 Phase Evolution of the Reagent Powder Mixtures upon Heating

Two sets of suspensions of reagent particles, *i.e.*, PbO, Nb_2O_5, MHC and TiO_2, the first one with pH = 11.4 and the second one with pH = 12.5 are prepared. The XRD patterns of the as-dried pH11.4 and pH12.5 powders and their phase evolution upon heating are presented in Figures 53 and 54, respectively. After milling and drying of the starting powder mixtures both pH11.4 and pH12.5 samples contain tetragonal PbO (PDF 85-1739), Nb_2O_5 (PDF 30-873), TiO_2 (PDF 01-078-1509), and $PbO{\cdot}6(PbCO_3){\cdot}3(Pb(OH)_2)$ (PDF 19-680). We could not determine any Mg-compound in the diffraction patterns, probably due to its low mass fraction. Furthermore, the relatively high background of the XRD patterns implies that an amorphous phase is present in the samples and the magnesium could be a part of the amorphous phase. The presence of the $PbO \cdot 6(PbCO_3) \cdot 3(Pb(OH)_2)$ is due the to partial dissolution of the PbO in the alkaline medium and the reaction of soluble lead species with OH^- and carbonate (CO_3^{2-}) ions, stemming either from dissolved atmospheric CO_2 and/or the dissolution of $(MgCO_3)_4{\cdot}Mg(OH)_2{\cdot}4H_2O$, as explained in the previous Chapter. We can conclude that the pH has no influence on the phase composition of the starting powders after milling and drying.

After heating at 500 °C in air the two samples contain Pb_3O_4 (minium, PDF 08-0019), TiO_2, the pyrochlore phase indexed as $Pb_5Nb_4O_{15}$ (PDF 46-637), and a small amount of $PbTiO_3$ phase (PDF-1-78-299). The minium forms upon the partial oxidation of PbO, as confirmed by the thermogravimetric analysis in the case of the PMN synthesis. At 800 °C the presence of a ternary pyrochlore indexed as $Pb_{1.83}Nb_{1.71}Mg_{0.29}O_{6.39}$ (PDF 37-0071), the perovskite PMN-PT, and a small amount of $PbTiO_3$ phases are observed in both cases. We must stress here that the proposed compositions of the two pyrochlores are the best match between the experimental spectrum and the reference patterns and no compositional analysis is preformed.

The pH11.4 powder heated at 850 °C contains the ternary pyrochlore, $PbTiO_3$,

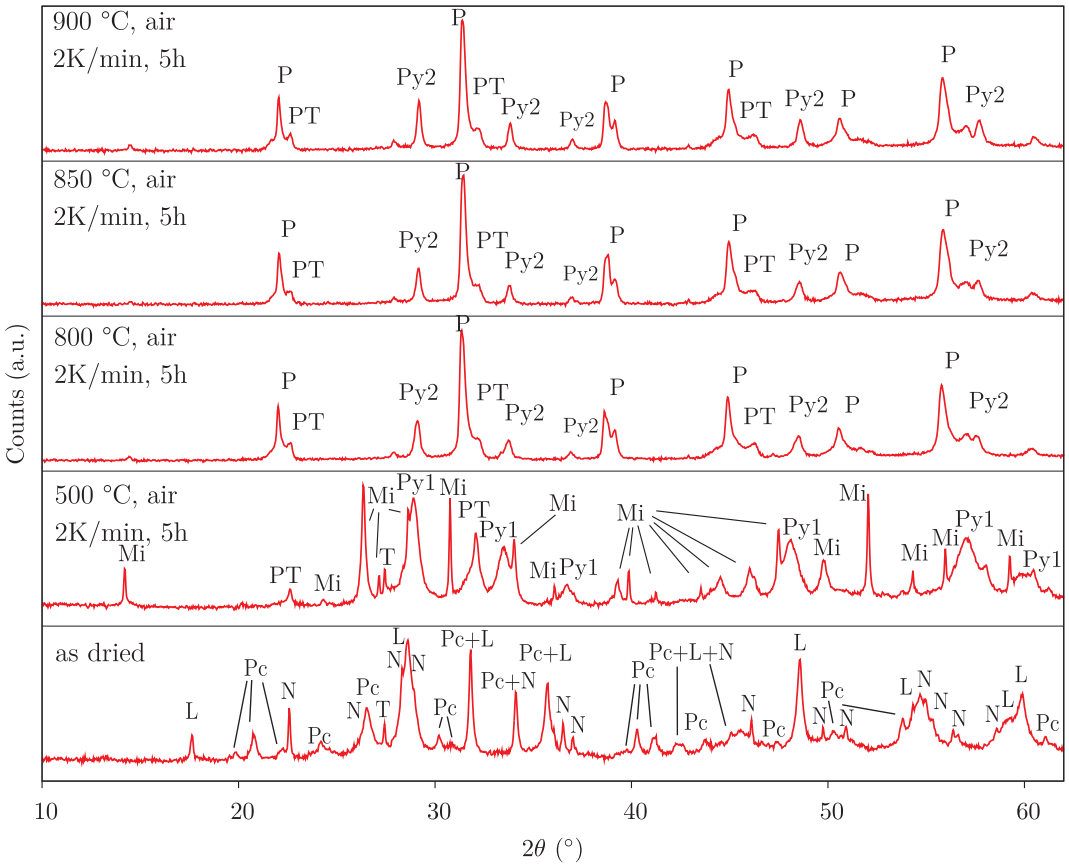

Figure 53: *XRD patterns of the starting powder mixture from the pH = 11.4 suspension, as dried, and heated at 500 °C, 800 °C, 850 °C, and 900 °C.* L - tetragonal PbO (litharge), N - Nb_2O_5, Pc - $PbO \cdot 6(PbCO_3) \cdot 3(Pb(OH)_2)$, T - TiO_2, Mi - minium Pb_3O_4, PT - $PbTiO_3$, P - perovskite, Py1 - pyrochlore $Pb_5Nb_4O_{15}$, Py2 - pyrochlore $Pb_{1.83}Nb_{1.71}Mg_{0.29}O_{6.39}$.

and PMN-PT phases, whereas the pH12.5 sample heated at the same temperature contains only the PMN-PT phase. The samples heated at 900 °C exhibit the same phase composition as the samples heated at a 50 °C lower temperature.

Both samples exhibit qualitatively the same phase composition when dried and heated at 500 °C and 800 °C. At a lower temperature, *i.e.*, 500 °C, the binary lead-niobium pyrochlore is formed, which reacts with the Mg species at higher temperatures to form the ternary Pb-Nb-Mg pyrochlore phase. Similarly, Chaput et al. [25] observed the reaction of MgO with the B-site-deficient pyrochlore, yielding the ternary Pb-Mg-Nb pyrochlore, and upon further heating the perovskite PMN.

The $PbTiO_3$ is the first perovskite phase detected in both samples, it is formed at as low as 500 °C. It is reported to be the easiest to prepare within the group of lead-based perovskites [13]. Furthermore, it was also detected in a PMN-PT powder mixture heated at 600 °C [121]. At higher temperatures the $PbTiO_3$ forms a solid solution with PMN, yielding PMN-PT. However, in the pH11.4 case a small amount of $PbTiO_3$ is still present after calcination at 900 °C.

At 850 °C the pure perovskite PMN-PT phase is formed only in the pH12.5 sample, while the pH11.4 sample also contains the ternary pyrochlore phase and a small amount of $PbTiO_3$. Obviously, the total conversion to the PMN-PT perovskite could not be achieved in the lower pH case. The appearance of the low-temperature intermediate

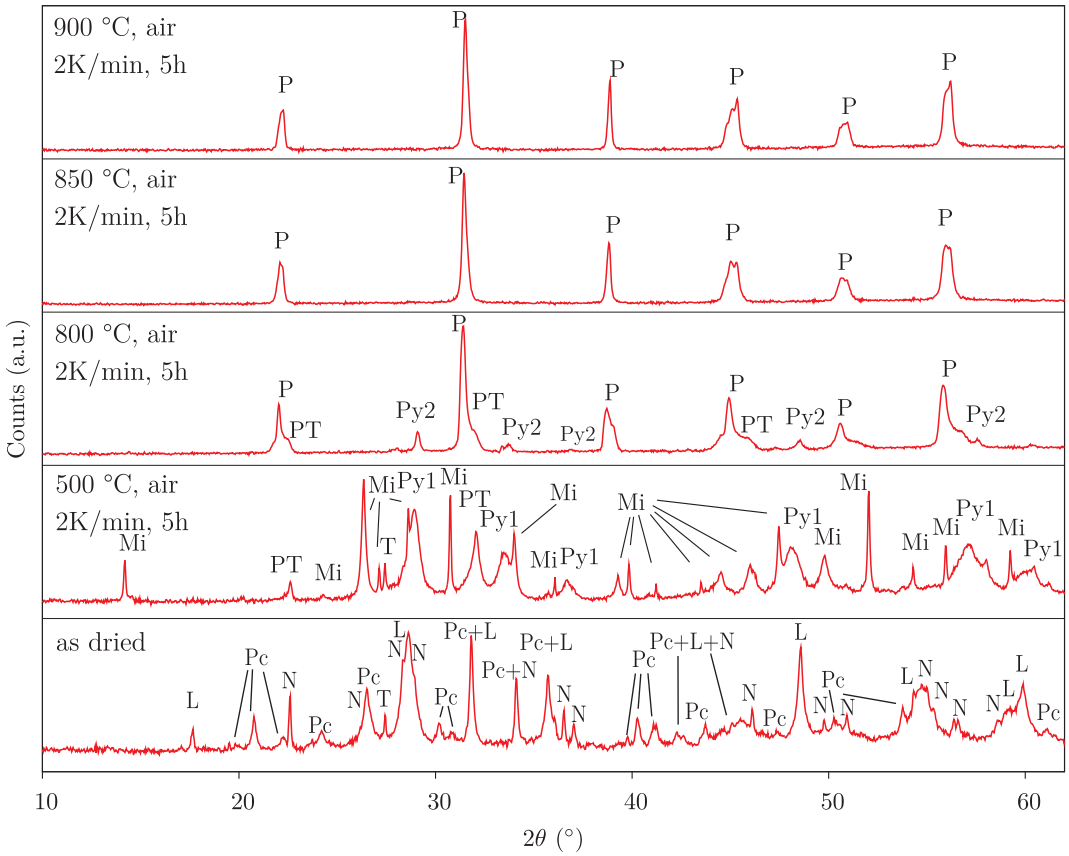

Figure 54: *XRD patterns of the starting powder mixture from the pH = 11.4 suspension, as dried, and heated at 500 °C, 800 °C, 850 °C, and 900 °C.* L - tetragonal PbO (litharge), N - Nb_2O_5, Pc - $PbO \cdot 6(PbCO_3) \cdot 3(Pb(OH)_2)$, T - TiO_2, Mi - minium Pb_3O_4, PT - $PbTiO_3$, P - perovskite, Py1 - pyrochlore $Pb_5Nb_4O_{15}$, Py2 - pyrochlore $Pb_{1.83}Nb_{1.71}Mg_{0.29}O_{6.39}$.

$PbTiO_3$ and ternary Pb-Mg-Nb pyrochlore phases in the pH11.4 samples and their absence in the pH12.5 samples confirms how important the structure of the colloidal agglomerates of the starting particles is. The latter enables the desired contacts, leading to the desired reactions.

A closer inspection of the XRD patterns of the pH12.5 sample calcined at 850 °C and 950 °C also reveals that the structure of the perovskite phase is changing with different processing temperatures. For this reason the perovskite reflection between 44–46° for the pH12.5 sample calcined at 850 °C and 900 °C, and sintered at 950 °C is shown in Figure 55. The shape of the peak is different at the three different temperatures. We have preformed a full-pattern Rietveld analysis for these three samples and calculated the structural composition of the perovskite phase, see Table 12. The processing temperature is influencing the structural composition of the perovskite phase. With increasing temperature the amount of monoclinic phase is decreasing, while the amount of tetragonal phase is increasing. The crystal structure could have an influence on the electrical properties of the material; however, we do not study this effect in detail here. Our main concern is the comparison of the pH11.4 and pH12.5 samples prepared under the same conditions, *i.e.*, calcined at 850 °C and sintered at 950 °C.

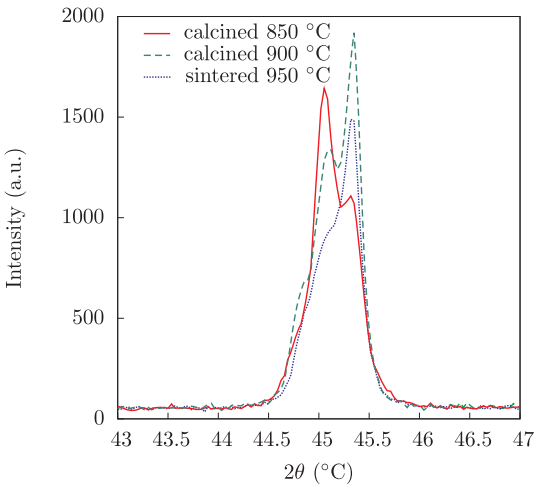

Figure 55: *Comparison of the XRD reflections of the perovskite phase between* 44–46° *for the pH12.5 samples calcined at 850 °C and 950 °C, and sintered at 950 °C.*

Table 12: *Results of the Rietveld analysis of the pH12.5 samples calcined at 850 °C and 900 °C and sintered at 950 °C.*

Sample	Structural composition
pH12.5, calcined @ 850 °C	66 % Pm monoclinic + 34 % P4mm tetragonal
pH12.5, calcined @ 900 °C	60 % Pm monoclinic + 40 % P4mm tetragonal
pH12.5, calcined @ 850 °C + sintered @ 950 °C	55 % Pm monoclinic + 45 % P4mm tetragonal

6.3.2 Morphology of the Calcined Powders

The particle size distribution (PSD) and the morphology of the powders calcined at 850 °C are analyzed. The results are collected in Figure 56. The average particle sizes of the pH11.4 and pH12.5 powders are equal to 0.45 μm and 0.42 μm, respectively. In both powders the particle sizes are found in the range 0.1–5 μm, but with different PSD functions. The FE-SEM micrograph of the pH11.4 sample is presented in Figure 56b. The primary particle size is about 0.2–0.5 μm, as seen from the inset. The largest size of the particles measured by the static light scattering is 5 μm, which indicates that the primary particles form large agglomerates. The size of the primary particles in the pH12.5 sample is up to 2 μm and is therefore much larger than in the pH11.4 sample, see Figure 56d. Both FE-SEM and PSD results confirm the presence of agglomerates up to 5 μm.

The main difference between the pH11.4 and pH12.5 sample is in the size of the primary particles, which are considerably smaller in the former case, although the average particle sizes, as measured by static light scattering, are similar in both cases. This suggests that the degree of agglomeration is much higher in the pH11.4 sample. Obviously, the starting pH of the suspensions significantly influences the morphology.

6.4 Sintering and Properties of the Ceramics

The samples calcined at 850 °C for 5 h are isostatically pressed into pellets at 300 MPa and sintered at 950 °C for 2 h, without any prior milling. The XRD patterns

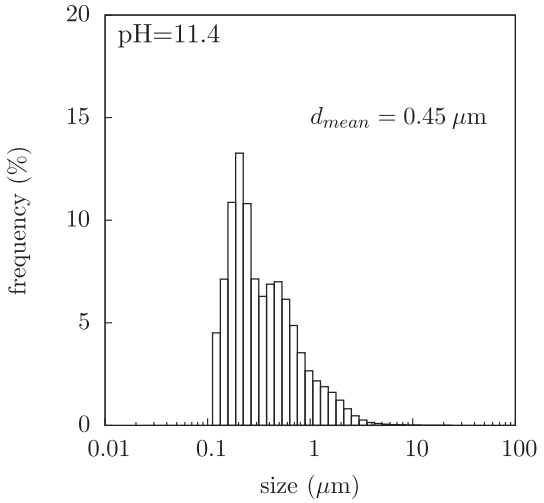

(a) PSD, pH = 11.4

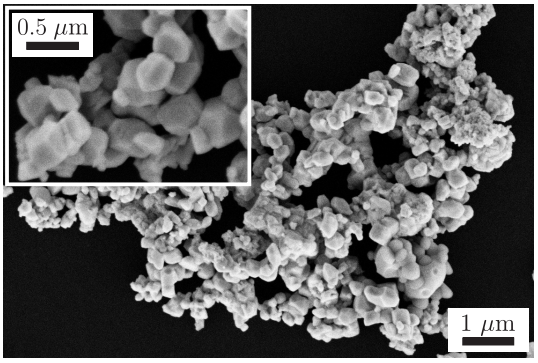

(b) FE-SEM, pH = 11.4

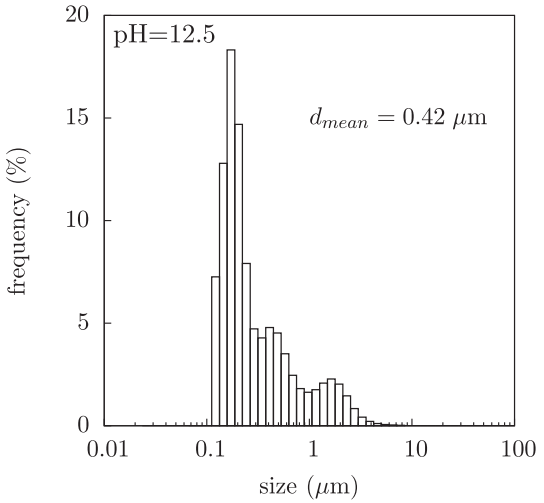

(c) PSD, pH = 12.5

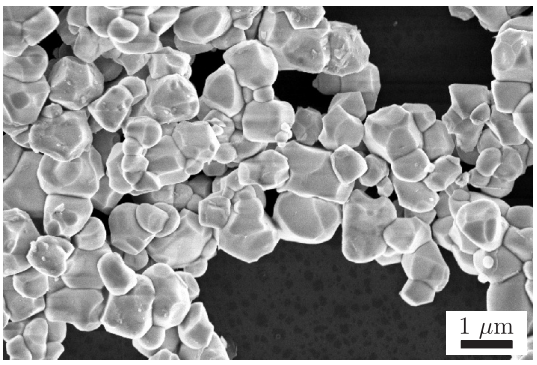

(d) FE-SEM, pH = 12.5

Figure 56: *Particle size distribution and FE-SEM micrographs of the sample calcined at 850 °C.* (a) Particle size distribution and (b) FE-SEM micrograph for the pH11.4 sample. (c) Particle size distribution and (d) FE-SEM micrograph for the pH12.5 sample.

of the sintered pH11.4 and pH12.5 samples are presented in Figure 57. The pH11.4 sample contains both perovskite and pyrochlore phases. Obviously, the pyrochlore is not converted to the perovskite during the sintering. On the other hand, the pH12.5 sample is pyrochlore-free, according to XRD.

In Figure 58 we present photographs of the pH11.4 and pH12.5 samples sintered at 950 °C. The pH11.4 sample is highly heterogeneous on the millimeter scale. One can clearly observe white regions within an orange matrix. In contrast the pH12.5 sample is homogeneous. The two samples also differ in density, the pH11.4 sample reaches only 81 % of the theoretical density (TD), whereas the pH12.5 sample is sintered to 96 % of TD. We assume that in the pH12.5 sample the agglomerates in the powder,

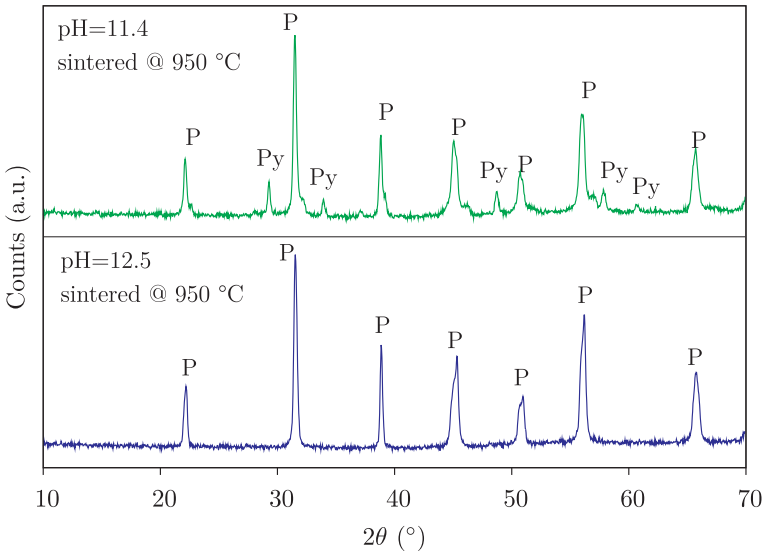

Figure 57: *XRD patterns of the samples sintered at 950 °C for 2 h.* Py – Pyrochlore, P – perovskite.

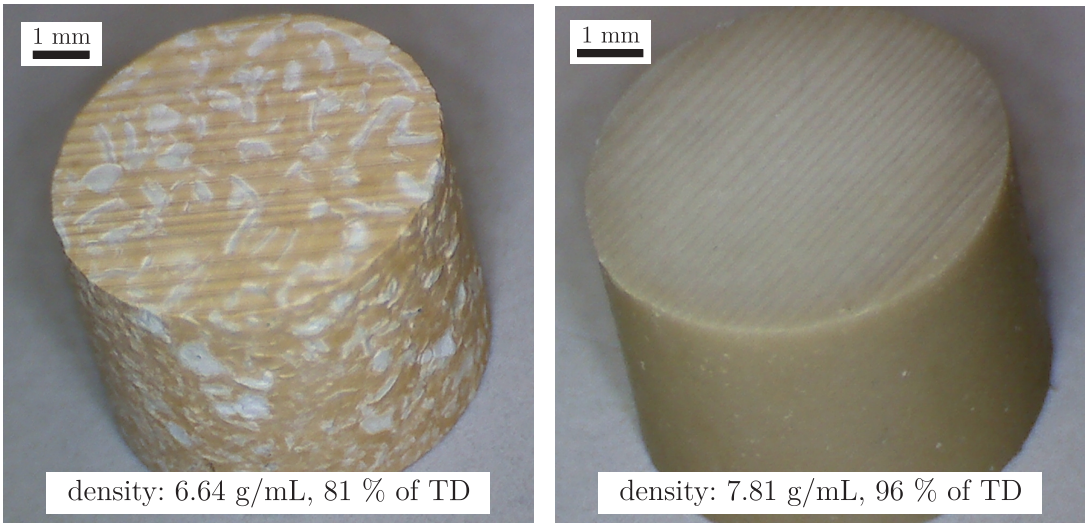

(a) pH = 11.4 (b) pH = 12.5

Figure 58: *Photographs of the pH11.4 and pH12.5 samples sintered at 950 °C for 2 h.* (a) pH11.4 sample and (b) pH12.5 sample.

which are observed in the FE-SEM and PSD (Figure 56c, 56d), are broken during the compaction and therefore the ceramics can be sintered to high density. Note that the sintering temperature used in this work is low in comparison to the literature, where the PMN-PT ceramics are typically sintered above 1000 °C to reach densities exceeding 90 % of TD [6, 7, 38].

The FE-SEM images of the polished and thermally etched ceramics sintered at 950 °C are presented in Figure 59. The microstructure of the pH11.4 sample is not homogeneous, it consists of regions with smaller submicron grains and larger grains of about 1–3 μm. The inset of Figure 59a is a lower-magnification image, where such het-

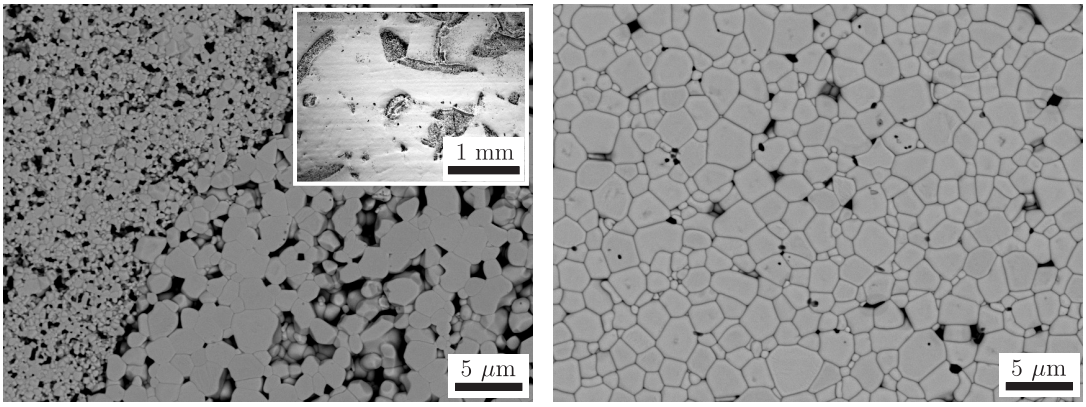

(a) pH = 11.4 (b) pH = 12.5

Figure 59: *Microstructures of the pH11.4 and pH12.5 samples sintered at 950 °C for 2 h.* (a) pH11.4 sample and (b) pH12.5 sample.

erogeneities are clearly seen; they are also seen in the macroscopic image, in Figure 58a. The ceramics are composed of a fine-grained matrix with inclusions of larger grains. A high fraction of porosity is observed in the pH11.4 sample, which is in agreement with a density of only 81 % of TD. In contrast, the pH12.5 sample sintered at 950 °C exhibits a homogeneous microstructure with a small amount of porosity and a grain-size of 0.5–3 μm. The average grain-size is 1.5 μm, as determined by the lineal intercept method. The difference in the microstructures of the pH11.4 and pH12.5 samples is explained on the basis of the different morphologies and sizes of the starting powders as well as of the presence of the pyrochlore phase in the pH11.4 sample.

For a further comparison the dielectric, ferroelectric and piezoelectric properties are measured for both samples sintered at 950 °C. The results are collected in Figure 60. The dielectric constant and dielectric losses as a function of temperature are collected in Figures 60a and 60b, for the pH11.4 and pH12.5 samples, respectively. The Curie temperature (T_C) is in both samples at 173 °C, which corresponds to the value reported for the 0.65PMN-0.35PT composition [7, 20]. The relative permittivity, ε_r, of the pH12.5 sample is considerably higher than the value obtained for the pH11.4 sample. At T_C, the ε_r for the case of pH12.5 sample is almost 18 000, which is approximately five times higher than in the case of the pH11.4 sample.

The hysteresis loops for the pH11.4 and pH12.5 samples are shown in Figures 60c and 60d. The remnant polarization, P_r, for the pH12.5 sample reaches 21 μC/cm^2, whereas the P_r is only 7 μC/cm^2 for the pH11.4 sample. Again, a deterioration of the properties is observed for the sample prepared at the lower pH.

In parallel with the polarization measurements the strain (S) vs. electric field (E) is also measured. The $S - E$ loops for the pH11.4 and pH12.5 samples are presented in Figures 60e and 60f. The measured peak-to-peak strains, S_{pp}, are markedly different in the two cases. The pH11.4 sample reaches an S_{pp} of only 0.03 % at the maximum electric field of 2 kV/mm, whereas the pH12.5 sample reaches an about 10 times higher value of $S_{pp} = 0.29$ % at the same field.

The d_{33} is also measured for both samples. The values for the pH11.4 and pH12.5 samples are 130 ± 20 pC/V and 460 ± 15 pC/V, respectively.

From these measurements we can conclude that the electrical properties are heavily deteriorated in the pH11.4 sample in comparison to the pH12.5 sample. We at-

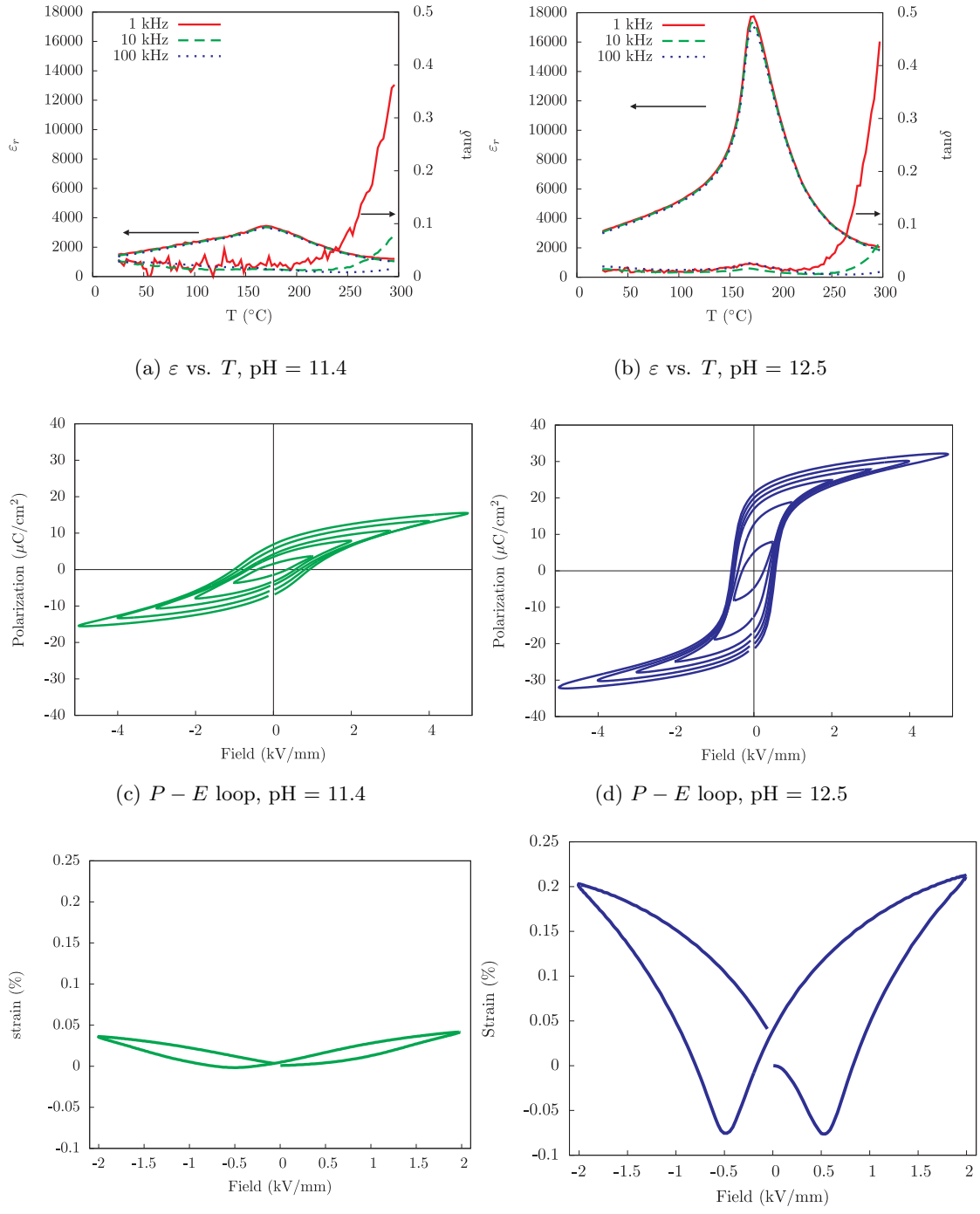

(a) ε vs. T, pH = 11.4

(b) ε vs. T, pH = 12.5

(c) $P - E$ loop, pH = 11.4

(d) $P - E$ loop, pH = 12.5

(e) $S - E$ loop, pH = 11.4

(f) $S - E$ loop, pH = 12.5

Figure 60: *Dielectric properties of the ceramics (a) pH11.4 and (b) pH12.5 sample. Polarization – Electric field ($P - E$) loops for (c) pH11.4 and (d) pH12.5 sample. Strain – Electric field ($P - E$) loops for (e) pH11.4 and (f) pH12.5 sample.*

tribute these differences to the presence of the pyrochlore phase, low density, and a non-homogeneous microstructure of the pH11.4 sample as compared to the pH12.5 sample. In conclusion, high-quality PMN-PT ceramics with good electrical properties can be produced using only the pH12.5 powder.

The influence of the sintering temperature on the properties of the pH12.5 ceramics is further evaluated. The results for the samples sintered at 950–1150 °C are collected in Table 13. The density of the sample sintered at 950 °C is 96 % of TD, and no

Table 13: *Properties of ceramics sintered at 950 °C, 1050 °C, and 1150 °C prepared from pH12.5 powder.*

T [°C]	ρ % of TD	ε_r @ RT	$\tan\delta$ @ RT	ε_r @ max	$\tan\delta$ @ max	P_r $[\frac{\mu C}{cm^2}]$	E_c $[\frac{kV}{mm}]$	d_{33} $[\frac{pC}{N}]$
950	96	3170	0.015	18000	0.025	21	0.56	460
1050	97	3780	0.013	32300	0.025	30	0.60	520
1150	96	3840	0.011	32700	0.023	30	0.60	510

Dielectric properties measured at 1 kHz are compared in the table.
RT – room temperature, which is 25 °C.
max – maximal value of dielectric constant.
The error of the density measurements is ±1 %.
The error of the measurement of ε_r is ± 100.
The error of the measurement of d_{33} is ± 20 pC/N.

considerable increase in density is observed at higher sintering temperatures. The values of the dielectric permittivity, P_r and the d_{33} of the ceramics sintered at 1050 °C are 3780 (at RT) and 32300 (at the peak temperature), 30 μC/cm^2 and 520 pC/N, showing a major improvement as compared to the ceramics sintered at 950 °C. No improvement of the measured properties could be obtained upon sintering at 1150 °C.

Table 14: *Properties of ceramics prepared from pH12.5 powder compared to literature values.*

Authors	Method	$T_{sintering}$ [°C]	ρ % of TD	ε_r @ RT	ε_r @ max	P_r $[\frac{\mu C}{cm^2}]$	E_c $[\frac{kV}{mm}]$
Kelly et al. [6]	Columbite	1250	> 94	3600	36000	/	/
Leite et al. [20]	Columbite[a]	950	~ 100	~ 2600	8160	12.3	0.33
Leite et al. [20]	Columbite[b]	950	~ 100	~ 3300	41720	33.1	0.43
Yu et al. [38]	PEG	1000	/	3440	16220	14	0.82
This work	CA[c]	950	96 %	3170	18000	21	0.56
This work	CA[c]	1050	97 %	3780	32300	30	0.60

[a] The ceramics is prepared with hot-pressing @ 950 °C.
[b] The ceramics is prepared with hot-pressing @ 950 °C and post-annealed @ 1150 °C for 10 h.
[c] The ceramics is prepared with controlled agglomeration of reagent particles.
All dielectric constants are measured @ 1 kHz.

The electrical properties are enhanced after sintering at 1050 °C. Leite et al. observed the enhancement of properties in the hot-pressed PMN-PT ceramics after post-annealing at 1150 °C for 5 and 10 h and explained it with the improved chemical homogeneity of the B-site cations in the post-annealed samples [20]. The same mechanism could explain

our results. At higher sintering temperatures the diffusion processes are enhanced, contributing to a more homogeneous distribution of atoms in the lattice.

To evaluate the effectiveness of our synthesis method in relation to other methods reported in the literature the properties of the ceramics prepared from the pH12.5 powder are compared with the properties of the ceramics reported in the literature, see Table 14. The properties of the ceramics prepared by the controlled agglomeration of reagent particles are comparable to the properties of the ceramics prepared by the columbite method; however, the sintering temperature in the latter case is 200 K higher [6]. In our case dense ceramics can be prepared at as low as 950 °C using conventional sintering, while in the case of the columbite-derived powder, hot pressing is usually needed to achieve high densities at low sintering temperatures [20]. Furthermore, Leite et al. [20] showed that post-annealing at 1150 °C for 10 h is needed to improve the properties, as explained above.

6.5 Summary

The synthesis of PMN-PT in an aqueous suspension is performed using the approach that was originally introduced for the synthesis of PMN, see previous Chapter. The pure perovskite $0.65Pb(Mg_{1/3}Nb_{2/3})O_3$–$0.35PbTiO_3$ powder is synthesized in a single calcination step at 850 °C from the suspension with the pH = 12.5. In contrast, when the suspension pH equals 11.4, the powder contains mixed phases after the calcination. In the suspension of the starting powders at lower pH the charges on the PbO and Nb_2O_5 particles are opposite, which leads to agglomerates with PbO-Nb_2O_5 contacts and consequently to the formation of the pyrochlore phase. At pH = 12.5 the positively charged $(MgCO_3)_4{\cdot}Mg(OH)_2{\cdot}4H_2O$ particles prevent the contacts between equally charged PbO and Nb_2O_5 and hence hinder the reaction to from the pyrochlore. After sintering at only 950 °C the pH12.5 sample reaches 96 % of theoretical density, while the density of the pH11.4 sample is only 81 % of TD. The microstructure of the pH11.4 sample is porous with regions of smaller and larger grains, while the pH12.5 ceramics exhibit dense and homogeneous microstructures with an average grain size of 1.5 μm. The dielectric permittivity at RT in the latter case equals to $\sim$ 3200, P_r = 15 μC/cm^2, E_c = 0.5 kV/mm, and S_{pp} = 0.3 % at a driving field of 2 kV/mm, while d_{33} = 460 pC/N. The dielectric, ferroelectric, and piezoelectric properties are largely deteriorated in the case of the pH11.4 sample.

The functional properties of the pH12.5 ceramic could be further improved by sintering at 1050 °C, which is attributed to a higher chemical homogeneity as compared to the ceramic sintered at 950 °C. The synthesis by controlled agglomeration of the reagent particles enabled lower sintering temperatures in comparison to the traditionally used columbite method, while having comparable properties. In conclusion, the synthesis by controlled agglomeration of the reagent particles was successfully implemented to form $0.65Pb(Mg_{1/3}Nb_{2/3})O_3$–$0.35PbTiO_3$.

7

Summary, General Conclusions and Outlook

In this Thesis we have introduced a new approach to solid-state synthesis, where with the design of the spatial distribution of reagent particles we control the solid-state reactions. First, we have numerically studied the agglomeration of the reagent particles for $Pb(Mg_{1/3}Nb_{2/3})O_3$ synthesis. The experimental conditions were chosen on the basis of the simulation results and our approach was first tested on the synthesis of $Pb(Mg_{1/3}Nb_{2/3})O_3$. The method was further extended to the synthesis of $0.65Pb(Mg_{1/3}Nb_{2/3})O_3$–$0.35PbTiO_3$. In both cases we have been able to synthesize materials in a pure perovskite phase using only one calcination step. Furthermore, the desired properties of our ceramics were achieved at sintering temperatures which are ~ 200 K lower than the conventionally used processing temperature.

Solid-state reactions are usually diffusion controlled; therefore, the contact surface between two solid particles is crucial for the reactions. In the case of the synthesis of $Pb(Mg_{1/3}Nb_{2/3})O_3$-based materials, all the reactions are not desired. To get quality ceramic materials the reactions between PbO and Nb_2O_5 need to be suppressed. Our idea to do this was to avoid the PbO-Nb_2O_5 contacts by the controlled agglomeration of reagent particles in the suspension.

In the first part of the Thesis we have used numerical simulations to study the mechanism of the agglomerate formation in the suspensions for $Pb(Mg_{1/3}Nb_{2/3})O_3$ synthesis. We have employed a Monte Carlo method for the simulations of the three-component system of charged particles representing the PbO, Nb_2O_5, and $(MgCO_3)_4{\cdot}Mg(OH)_2{\cdot}4H_2O$ (MHC) reagent particles in the suspension. There are two reasons for employing the simulations for the study of the agglomeration: first, agglomeration of colloidal particles is hard to investigate experimentally, and, second, simulations give the possibility to study a wide range of parameters that can be unreachable by experiments. A realistic model with experimentally measured parameters was used to describe the interactions between the particles to closely mimic the experimental conditions. Two sets of simulations were made corresponding to two suspensions with different pH values, *i.e.*, pH = 11.4 and pH = 12.5, where we have expected markedly different structures of the agglomerates. This was the main focus of our investigations. Additionally, we studied the particle size effects. In all cases the results from simulations have shown that at pH = 11.4 a large population of clusters with PbO-Nb_2O_5 contacts are formed, which enhance the reaction to the non-desired pyrochlore phases. In contrast, at pH = 12.5 agglomerates form where the MHC particles effectively separate the PbO and Nb_2O_5 particles; therefore, these conditions are more favorable for the synthesis of the pure perovskite phase. The second part of simulations addressing the size effects has shown

that the steric hindrance caused by the MHC particles is more effective in the cases where these particles are smaller. We can conclude that such a numerical approach is appropriate as well as effective for studying the agglomeration process in colloidal suspensions. In our example the simulations were used as a complementary tool to our experimental work and therefore all the studied conditions were closely related to our experiments. To our knowledge there is a lack of reports in the literature about agglomeration in three-component colloidal systems. This work opens up the opportunity for further investigations of these system in a more general way. In such a case one should consider changing a wider range of parameters, *e.g.*, concentrations, particle number ratios, particle size ratios, and particle charges. And in addition to the analysis of the inner structure of the agglomerates and the contact analysis, one should also consider the structure of the agglomerates on a larger scale, *e.g.*, fractal dimension analysis of clusters should be employed. Another possibility is to investigate the dynamics of the formation of colloidal agglomerates on a larger scale, this could be done by employing Brownian Dynamics (BD). In contrast to Monte Carlo simulations, which explore the phase space of a system, Brownian Dynamics simulations are carried out in real space, which gives a possibility of tracking real dynamics of the cluster formation. Furthermore the hydrodynamic interactions, which are especially important in concentrated system, could be implemented in the BD simulations to get more realistic results. All of this is left for future work where the results presented in this Thesis make a good starting point.

We have applied the knowledge obtained by numerical simulations to our experimental work, *i.e.*, the synthesis of $Pb(Mg_{1/3}Nb_{2/3})O_3$ in only one calcination step. We have prepared suspensions of the reagent particles, *i.e.*, PbO, Nb_2O_5, and MHC at different pH conditions. Aqueous suspensions with pH = 10.0, pH = 11.4 and pH = 12.5 were prepared, for comparison also a suspension in acetone was prepared. After homogenization we have dried the suspensions of reactant mixtures and heated them at 900 °C where the solid-state reaction took place. In agreement with what we have predicted by simulations, only the powder prepared form the suspension with pH = 12.5 reacted to form the pure perovskite phase. All three other samples yielded, in addition to perovskite, the undesirable pyrochlore phase after heat treatment at 900 °C. As expected the ceramics prepared from the pH12.5 powder exhibited the best properties, *i.e.*, the largest density, largest dielectric permittivity, and largest electrostrictive response, among all four samples. Furthermore the density of 95 % of TD was achieved for this sample with a sintering temperature of only 950 °C and the ceramics exhibited comparable or better properties than the ceramics prepared with other methods using $\sim$ 200 K higher sintering temperatures. *From these results we can conclude that the structure of the agglomerates, which is different at different pH conditions as shown with simulations, has a major influence on the solid-state reactions that occur at elevated temperatures.* The proposed contacts within the agglomerates are in good agreement with the experimental results. At pH = 11.4, where we saw PbO-Nb_2O_5 contacts, the pyrochlore phase is present in the samples after the solid-state reaction, while at pH = 12.5 where PbO-Nb_2O_5 contacts are blocked by MHC particles, no pyrochlore phase is present after the calcination. Good properties of the pH12.5 ceramics sintered at only 950 °C imply that the PMN powder prepared with controlled agglomeration of the reactant powders is highly homogeneous. Therefore, it could be employed for thick-film preparation where low processing temperatures are beneficial. One further step would be the use of this powder for the preparation of suspensions for ink-jet printing. This technique enables the direct patterning of active or passive structures on a substrate in a layer-by-layer deposition process.

In the last part, our method with the controlled agglomeration of reagent particles was extended to the synthesis of $0.65Pb(Mg_{1/3}Nb_{2/3})O_3$–$0.35PbTiO_3$. Here, one more component is added to the mixture of reagent particles, *i.e.*, TiO_2. Again, two sets of experiments were conducted: one with suspension pH = 11.4 and other with pH = 12.5. The structure of the agglomerates was expected to be similar to the case of PMN. At lower pH the PbO-Nb_2O_5 and PbO-TiO_2 contacts were formed, while at higher pH these contacts were suppressed by MHC particles. Similarly as in the case of PMN, only the pH12.5 sample was phase pure after the calcination at 850 °C. The ceramics prepared from the pH12.5 sample were sintered to 96 % of theoretical density at just 950 °C. The functional properties were further improved by sintering at 1050 °C, which is attributed to the higher chemical homogeneity achieved at higher sintering temperatures. In comparison to the literature, again lower sintering temperatures were needed to achieve comparable properties. One of the possible improvements of this method used for the synthesis of PMN-PT would be further manipulation of the interactions. At pH = 12.5 the TiO_2 particles are negatively charged and therefore they probably also adsorb on MHC particles. Therefore, some of the MHC surface is occupied by TiO_2 and the ability of MHC to prevent PbO-Nb_2O_5 contacts is reduced. If TiO_2 was positively charged like MHC, they would not adsorb on the MHC, but they would also block the PbO-Nb_2O_5 contacts. Furthermore, this would probably improve the homogenization of the B sites (Mg, Nb, Ti) in the sample.

The idea of controlling the agglomerate formation by control of the interactions between reagent particles used for the new approach to solid-state synthesis presented in this Thesis is general. In this work the interactions were only mediated by changing the zeta-potentials of the reagent powders via pH control. Such pH conditions were found where the electrokinetic properties of the reagent powders for PMN synthesis were appropriate to get the desired agglomerate structure. However, in general, this might not be the case, maybe appropriate pH conditions could not be found. In such situations, one should use other approaches to change the surface charge and consequently the interactions between the reagent particles in a desired way. One of the possibilities is to change the interactions by the adsorption of appropriately charged molecules on the particle surfaces. With such modifications the generality of our proposed method would be further extended and the method could be used for the synthesis of other complex materials.

Acknowledgements

I would like to thank my supervisor and head of the lab Prof. Marija Kosec: firstly for giving me the opportunity to work at K5; and secondly for her guidance, support and advice. I have learned immense number of new things in these four years and, especially, I had the privilege to work in an environment where high-class scientific research is done.

Next, I have to thank the people with whom I did the majority of the work presented in this Thesis. Barbara Malič, Andrej Degen, Janez Holc, Bosiljka Tadić and Danjela Kuščer are acknowledged for their support, discussions, analysis, and great ideas.

A lot more people helped me to get the results that are included in this Thesis, and these are: Brigita Kužnik, Elena Ion, Elena Tchernychova, Andreja Benčan, and Jenny Tellier. You all know what you have done; if you have forgotten, just go through the figures and you will remember. So, thank you all.

There are two persons who would fit into the category above, but I think that they deserve a special place. These are my "roommates" Hana Uršič and Sebastjan Glinšek. Thank you for your help with the XRD analysis and the microscopy and all the other stuff. It is cool to work with people with who you can laugh at jokes in one minute and in the next minute you are analyzing scientific data together.

Special thanks go to Silvo Drnovšek and Jena Cilenšek, without them our life at K5 would be much harder. I think that every sample done at K5 goes through their hands at least once.

Tadej Rojac is the person with whom I really enjoy to work, because it is fun and in most cases fruitful. When we are together new ideas are just popping up.

I also need to thank all other people who work at the Electronic Ceramics Department for providing a positive and working atmosphere. I enjoy coming to K5 every morning.

I would like to thank dr. Paul Bowen for inviting me to his lab @ EPFL, where I have learned some of the basics of Brownian Dynamics simulations. I am also grateful to Sandra Galmarini, who worked with me during my stay in Lausanne.

The Slovenian Research Agency and the Center of Excellence NAMASTE are gratefully acknowledge for financially supporting my work.

I think it is fair to repeat the words of my colleague Andrej Lajovic at this point and thank all the people that will probably never read this, but anyway. I would like to say thanks to all the people who believe in *free* and *open* programming and are developing this software day by day. I cannot imagine my scientific work without the GNU/Linux operating system and software packages like TEX, gnuplot and octave.

Finally, I need to say thanks to my wife Polona for her support, encouragement and understanding during my work and especially during the writing of this Thesis.

References

[1] Kolar, D. *Tehnična Keramika I & II* (Zavod Republike Slovenije za šolstvo in šport, Ljubljana, 1993).

[2] Reed, J. S. *Principles of Ceramics Processing* (John Wiley & Sons, Inc., New York, 1995).

[3] Rao, C. N. R.; Gopalakrishnan, J. *New Directions in Solid State Chemistry* (Cambridge University Press, Cambridge, 1997).

[4] Damjanovic, D. Ferroelectric, dielectric and piezoelectric properties of ferroelectric thin films and ceramics. *Rep. Prog. Phys.* **61**, 1267–1324 (1998).

[5] Bottom, V. Measurement of the Piezoelectric Coefficient of Quartz Using the Fabry-Perot Dilatometer. *J. Appl. Phys.* **41**, 3941–3944 (1970).

[6] Kelly, J.; Leonard, M.; Tantigate, C.; Safari, A. Effects of Composition on the Electromechanical Properties of (1-x)$Pb(Mg_{1/3}Nb_{2/3})O_3$-x$PbTiO_3$ Ceramics. *J. Am. Ceram. Soc.* **80**, 957–964 (1997).

[7] Uršič, H.; Tellier, J.; Hrovat, M.; Holc, J.; Drnovšek, S.; Bobnar, V.; Alguero, M.; Kosec, M. The Effect of Poling on the Properties of 0.65$Pb(Mg_{1/3}Nb_{2/3})O_3$–0.35$PbTiO_3$ Ceramics. *Jpn. J. Appl. Phys.* **50**, 035801 (2011).

[8] Setter, N. ABC of Piezoelectricity and Piezoelectric Materials. In: Setter, N. (ed.) *Pezoelectric Materials in Devices.* 67–81 (Ceramics Laboratory, EPFL Swiss Federal Institute of Technology, Lausanne, 2002).

[9] Bokov, A. A.; Ye, Z.-G. Recent progress in relaxor ferroelectrics with perovskite structure. *J. Mater. Sci.* **41**, 31–52 (2006).

[10] Park, S.-E.; Shrout, T. R. Ultrahigh strain and piezoelectric behavior in relaxor based ferroelectric single crystals. *J. Appl. Phys.* **82**, 1804–1811 (1997).

[11] Ruan, W.; Li, G.; Zeng, J.; Bian, J.; Kamzina, L.; Zeng, H.; Zheng, L.; Ding, A. Large Electro-Optic Effect in La-Doped 0.75$Pb(Mg_{1/3}Nb_{2/3})O3$ – 0.25$PbTiO_3$ Transparent Ceramic by Two-Stage Sintering. *J. Am. Ceram. Soc.* **93**, 2128–2131 (2010).

[12] Heartling, G. H. Feroelectric Ceramics: "History and Technology". *J. Am. Ceram. Soc.* **82**, 2341–2359 (1999).

[13] Shrout, T. R.; Halliyal, A. Preparation of Lead–Based Ferroelectric Relaxors for Capacitors. *Am. Ceram. Soc. Bull.* **66**, 704–711 (1987).

[14] Uršič, H.; Hrovat, M.; Holc, J.; Zarnik, M. S.; Drnovšek, S.; Maček, S.; Kosec, M. A large–displacement $65Pb(Mg_{1/3}Nb_{2/3})O_3$–$35PbTiO_3$/Pt bimorph actuator prepared by screen printing. *Sens. Actuators, B.* **133**, 699–704 (2008).

[15] Alguero, M. Perovskite, relaxor-based MPB ceramic materials structured at different (levels and) scales. *Seminar at JSI* (2008).

[16] Inada, M. Analysis of the Formation Process of the Piezoelectric PCM Ceramics. *Jpn. Natl. Tech. Rep.* **27**, 95–102 (1977).

[17] Lejeune, M.; Boilot, J. Formation mechanism and ceramic process of the ferroelectric perovskites: $Pb(Mg_{1/3}Nb_{2/3})O_3$ and $Pb(Fe_{1/2}Nb_{1/2})O_3$. *Ceram. Int.* **8**, 99–103 (1982).

[18] Swartz, S. L.; Shrout, T. R. Fabrication of perovskite lead magnesium niobate. *Mat. Res. Bull.* **17**, 1245–1250 (1982).

[19] Kwon, S.; Sabolsky, E.; Messing, G. Low-Temperature Reactive Sintering of 0.65 PMN·0.35 PT. *J. Am. Ceram. Soc.* **84**, 648–650 (2001).

[20] Leite, E.; Scotch, A.; Khan, A.; Li, T.; Chan, H.; Harmer, M.; Liu, S.; Park, S. Chemical heterogeneity in PMN-35PT ceramics and effects on dielectric and piezoelectric properties. *J. Am. Ceram. Soc.* **85**, 3018–3024 (2002).

[21] Villegas, M.; Caballero, A. C.; Kosec, M.; Moure, C.; Duraán, P.; Fernández, J. F. Effects of PbO excess in $Pb(Mg_{1/3}Nb_{2/3})O_3$–$PbTiO_3$ ceramics: Part I. Sintering and dielectric properties. *J. Mater. Res.* **14**, 891–897 (1999).

[22] Zhao, S.; Li, Q.; Feng, Y.; Nan, C. Microstructure and dielectric properties of PMN-PT ceramics prepared by the molten salts method. *J. Phys. Chem. Solids* **70**, 639–644 (2009).

[23] Ghasemifard, M.; Hosseini, S.; Khorrami, G. Synthesis and structure of PMN-PT ceramic nanopowder free from pyrochlore phase. *Ceram. Int.* **35**, 2899–2905 (2009).

[24] Chen, X.; Fan, H.; Fu, Y.; Liu, L.; Chen, J. Low-temperature fabrication and crystallization behavior of $Pb(Mg_{1/3}Nb_{2/3})O_3$ crystallites by a hydrothermal process. *J. Alloys Compd.* **469**, 322–326 (2009).

[25] Chaput, F.; Boilot, J.; Lejeune, M.; Papiernik, R.; Hubert-Pfalzgraf, L. Low-Temperature Route to Lead Magnesium Niobate. *J. Am. Ceram. Soc.* **72**, 1355–1357 (1989).

[26] Ravindranathan, P.; Komarneni, S.; Bhalla, A. S.; Roy, R. Dielectric properties of sol-gel derived lead magnesium niobate ceramics. *Ferroelectr., Lett. Sect.* **11**, 137–144 (1990).

[27] Beltran, H.; Cordoncillo, E.; Escribano, P.; Careda, J. B.; Coats, A.; West, A. R. Sol–Gel Synthesis and Characterization of $Pb(Mg_{1/3}Nb_{2/3})O_3$ (PMN) Ferroelectric Perovskite. *Chem. Mater.* **12**, 400–405 (2000).

[28] Jiwei, Z.; Bo, S.; Liangying, Z.; Xi, Y. Preparation and dielectric properties by sol-gel derived PMN-PT powder and ceramic. *Mater. Chem. Phys.* **64**, 1–4 (2000).

[29] Watanabe, A.; Haneda, H.; Moriyoshi, Y.; Shirasaki, S.; Kuramoto, S.; Yamamura, H. Preparation of lead magnesium niobate by a coprecipitation method. *J. Mater. Sci.* **27**, 1245–1249 (1992).

[30] Carvalho, J. C.; Paiva-Santos, C. O.; Zeghete, M. A.; Oliveira, C. F.; Varela, J. A. Phase Analysis of Seeded and Doped $Pb(Mg_{1/3}Nb_{2/3})O_3$ Prepared by Organic Solution of Citrates. *J. Mater. Res.* **11**, 1795–1799 (1996).

[31] Choy, J. H.; Han, Y. S.; Song, S. W.; Chang, S. H. Preparation of Single-phase $Pb(Mg_{1/3}Nb_{2/3})O_3$ Samples Utilizing Information from Solubility Relationships in the Pb–Mg–Nb–citric acid–H_2O System. *J. Mat. Chem.* **4**, 1271–1274 (1994).

[32] Han, K. R.; Kim, S. New preparation method of low-temperature sinterable $Pb(Mg_{1/3}Nb_{2/3})O_3$ powder ant its dielectric properties. *J. Mater. Sci.* **35**, 2055–2059 (2000).

[33] Zhai, H.; Tang, R.; Li, A.; Guo, H.; Xia, Y.; Wu, D. Preparation and Characterization of Relaxor Ferroelectric $0.65Pb(Mg_{1/3}Nb_{2/3})O_3$–$0.35PbTiO_3$ by a Polymerizable Complex Method. *J. Am. Ceram. Soc.* **92**, 1256–1261 (2009).

[34] Wang, J.; Junmin, X.; Dongmei, W.; Beng, N. W. Mechanochemically synthesized lead magnesium niobate. *J. Am. Ceram. Soc.* **82**, 1358–1360 (1999).

[35] Wang, J.; Dongmei, W.; Junmin, X.; Beng, N. W. Mechanochemical synthesis of 0.9 $Pb(Mg_{1/3}Nb_{2/3})O_3$ – 0.1 $PbTiO_3$ from mixed oxides. *Adv. Mater.* **11**, 210–213 (1999).

[36] Kuščer, D.; Meden, A.; Holc, J.; Kosec, M. Mechano–synthesis of lead–magnesium–niobate ceramics. *J. Am. Ceram. Soc.* **89**, 3081–3088 (2006).

[37] Kuščer, D.; Holc, J.; Kosec, M. Formation of 0.65 $Pb(Mg_{1/3}Nb_{2/3})O_3$ – 0.35 $PbTiO_3$ Using a High-Energy Milling Process. *J. Am. Ceram. Soc.* **90**, 29–35 (2007).

[38] Yu, S.; Huang, H.; Zhou, L.; Ye, Y. A Polyethylene Glycol-Modified Solid-State Reaction Route to Synthesize Relaxor Ferroelectric $Pb(Mg_{1/3}Nb_{2/3})O_3$–$PbTiO_3$ (PMN-PT). *J. Am. Ceram. Soc.* **91**, 1057–1064 (2008).

[39] Gu, H.; Shih, W. Y.; Shih, W.-H. Single-Calcination Synthesis of Pyrochlore-Free 0.9 $Pb(Mg_{1/3}Nb_{2/3})O_3$ – 0.1 $PbTiO_3$ and $Pb(Mg_{1/3}Nb_{2/3})O_3$ Ceramics Using a Coating Method. *J. Am. Ceram. Soc.* **86**, 217–221 (2003).

[40] Gu, H.; Shih, W. Y.; Shih, W.-H. Low temperature, single step, reactive sintering of lead magnesium niobate using $Mg(OH)_2$ – coated Nb_2O_5 powders. *J. Am. Ceram. Soc.* **88**, 1435–1443 (2005).

[41] Xu, Z.; Chu, R.; Hao, J.; Zhang, Y.; Li, G.; Yin, Q.; Ding, A. Single-Calcination Synthesis of Pyrochlore Free $Pb(Mg_{1/3}Nb_{2/3})O_3$ Powders Using Particle-Coating Method. *J. Am. Ceram. Soc.* **93**, 18–21 (2010).

[42] Vallar, S.; Houviet, D.; Fallah, J. E.; Kervadec, D.; Haussonne, J.-M. Oxide slurries stability and powder dispersion: Optimization with zeta potential and rheological measurements. *J. Euro. Ceram. Soc.* **19**, 1017–1021 (1999).

[43] Definition and Classification of Colloids. *http://old.iupac.org/reports/2001/colloid_2001/manual_of_s_and_t/node33.html* (accessed October 2011).

[44] Hunter, R. J. *Foundations of Colloid Science* (Oxford University Press, New York, 2001).

[45] Lewis, J. A. Colloidal Procesing of Ceramics. *J. Am. Ceram. Soc.* **83**, 2341–2359 (2000).

[46] Pettersson, A.; Marino, G.; Pursiheimo, A.; Rosenholm, J. Electrosteric stabilization of Al_2O_3, ZrO_2, and 3Y-ZrO_2 suspensions: effect of dissociation and type of polyelectrolyte. *J. Colloid Interface Sci.* **228**, 73–81 (2000).

[47] Fritz, G.; Schädler, V.; Willenbacher, N.; Wagner, N. Electrosteric stabilization of colloidal dispersions. *Langmuir* **18**, 6381–6390 (2002).

[48] Likos, C. N.; Vaynberg, K. A.; Löwen, H.; Wagner, N. J. Colloidal stabilization by adsorbed gelatin. *Langmuir* **16**, 4100–4108 (2000).

[49] Tuinier, R.; Vliegenthart, G.; Lekkerkerker, H. Depletion interaction between spheres immersed in a solution of ideal polymer chains. *J. Chem. Phys.* **113**, 10768–10775 (2000).

[50] Dzubiella, J.; Likos, C. N.; Löwen, H. Star-polymers as depleting agents of colloidal hard spheres. *Europhys. Lett.* **58**, 133 (2002).

[51] Israelachvili, J. Solvation forces and liquid structure, as probed by direct force measurements. *Acc. Chem. Res.* **20**, 415–421 (1987).

[52] Lajovic, A.; Jamnik, A. Soft-Core Attractive Model Fluid: Structure, Thermodynamics and Inter-colloidal Solvation Force. *Acta Chim. Slov.* **54**, 476–483 (2007).

[53] Lajovic, A.; Tomšič, M.; Jamnik, A. Depletion effects in a mixture of hard and attractive colloids. *J. Chem. Phys.* **130**, 104101 (2009).

[54] Elimelech, M.; Gregory, J.; Jia, X.; Williams, R. A. *Particle deposition and aggregation* (Butterworth-Heinemann, Woburn, 1998).

[55] Lifshitz, E. M. The theory of molecular attractive forces between solids. *Soviet Phys. JETP* **2**, 73–83 (1956).

[56] Hamaker, H. C. The London–van der Waals attraction between spherical particles. *Physica* **4**, 1058–1072 (1937).

[57] Cerbelaud, M.; Videcoq, A.; Abélard, P.; Pagnoux, C.; Rossignol, F.; Ferrando, R. Heteroaggregation between Al_2O_3 Submicrometer Particles and SiO_2 Nanoparticles: Experiment and Simulation. *Langmuir* **24**, 3001–3008 (2008).

[58] Cerbelaud, M.; Videcoq, A.; Abélard, P.; Pagnoux, C.; Rossignol, F.; Ferrando, R. Self-assembly of oppositely charged particles in dilute ceramic suspensions: predictive role of simulations. *Soft Matter* **6**, 370–382 (2010).

[59] in't Veld, P. J.; Plimpton, S. J.; Grest, G. S. Accurate and efficient methods for modeling colloidal mixtures in an explicit solvent using molecular dynamics. *Comput. Phys. Commun.* **179**, 320–329 (2008).

[60] M. Hütter. Coagulation rates in concentrated colloidal suspensions studied by Brownian dynamics simulation. *Phys. Chem. Chem. Phys.* **1**, 4429–4436 (1999).

[61] Kim, S.; Lee, K.-S.; Zachariah, M. R.; Lee, D. Three-dimensional off-lattice Monte Carlo simulations on a direct relation between experimental process parameters and fractal dimension of colloidal aggregates. *J. Colloid Interface Sci.* **344**, 353–361 (2010).

[62] Cordelair, J.; Greil, P. Flocculation and coagulation kinetics of Al_2O_3 suspensions. *J. Eur. Ceram. Soc.* **24**, 2717–2722 (2004).

[63] Aschauer, U.; Burgos-Montes, O.; Moreno, R.; Bowen, P. Hamaker 2: A Toolkit for the Calculation of Particle Interactions and Suspension Stability and its Application to Mullite Synthesis by Colloidal Methods. *J. Dispersion Sci. Technol.* **32**, 470–479 (2011).

[64] Behrens, S.; Christl, D.; Emmerzael, R.; Schurtenberger, P.; Borkovec, M. Charging and aggregation properties of carboxyl latex particles: Experiments versus DLVO theory. *Langmuir* **16**, 2566–2575 (2000).

[65] Diebold, U.; Li, S.; Schmid, M. Oxide surface science. *Annu. Rev. Phys. Chem.* **61**, 129 (2010).

[66] Guhl, H.; Miller, W.; Reuter, K. Water adsorption and dissociation on $SrTiO_3$ (001) revisited: A density functional theory study. *Phys. Rev. B* **81**, 155455 (2010).

[67] Degen, A.; Kosec, M. Effect of pH and impurities on the surface charge of zinc oxide in aqueous solution. *J. Eur. Ceram. Soc.* **20**, 667–673 (2000).

[68] Liang, Y.; Hilal, N.; Langston, P.; Starov, V. Interaction forces between colloidal particles in liquid: Theory and experiment. *Adv. Colloid Interface Sci.* **134**, 151–166 (2007).

[69] Delgado, A. V.; Gonzales-Caballero, F.; Hunter, R. J.; Koopal, L. K.; Lyklema, J. Measurement and interpretation of electrokinetic phenomena. *Pure Appl. Chem.* **77**, 1753–1805 (2005).

[70] Löwen, H.; Kramposthuber, G. Optimal effective pair potential for charged colloids. *Europhys. Lett.* **23**, 673–678 (1993).

[71] Hogg, R.; Healy, T. W.; Fürstenau, D. W. Mutual coagulation of colloidal dispersions. *Trans. Faraday Soc.* **62**, 1638–1651 (1966).

[72] Liu, J.; Luijten, E. Stabilization of colloidal suspensions by means of highly charged nanoparticles. *Phys. Rev. Lett.* **93**, 247802 (2004).

[73] Derjaguin, B. V.; Landau, L. D. Theory of the stability of strongly charged lyophobic sols and the adhesion of strongly charged particles in solutions of electrolytes. *Acta Physicochim. USSR* **14**, 633–662 (1941).

[74] Verwey, E. J. W.; Overbeek, J. T. G. *Theory of the stability of lyophobic colloids: the interaction of sol particles having an electric double layer* (Elsevier Publishing Company, Amsterdam, 1948).

[75] Ducker, W. A.; Senden, T. J.; Pashley, R. M. Direct measurement of colloidal forces using an atomic force microscope. *Nature* **353**, 239–241 (1991).

[76] Hartley, P. G.; Larson, I.; Scales, P. J. Electrokinetic and direct force measurements between silica and mica surfaces in dilute electrolyte solutions. *Langmuir* **13**, 2207–2214 (1997).

[77] Frenkel, D.; Smit, B. *Understanding Molecular Simulation: From Algorithms to Applications* (Academic Press, San Diego, 2002).

[78] Schmidt, M. Simulations of Systems with Colloidal Particles. In: Borówko, M. (ed.) *Computational methods in surface and colloid science*. 745–773 (Marcel Dekker, New York, 2000).

[79] Dijkstra, M. Computer simulations of charge and steric stabilised colloidal suspensions. *Curr. Opin. Colloid Interface Sci.* **6**, 372–382 (2001).

[80] Chen, J. C.; Kim, A. S. Brownian Dynamics, Molecular Dynamics, and Monte Carlo modeling of colloidal systems. *Adv. Colloid Interface Sci.* **112**, 159–173 (2004).

[81] Allen, M. P.; Tildesley, D. J. *Computer Simulation of Liquids* (Clarendon Press, Oxford, 1987).

[82] Spohr, E. Water and Soluions at Interface: Computer Simulations on the Molecular Level. In: Borówko, M. (ed.) *Computational methods in surface and colloid science*. 347–386 (Marcel Dekker, New York, 2000).

[83] Andrienko, D.; Germano, G.; Allen, M. P. Computer simulation of topological defects around a colloidal particle or droplet dispersed in a nematic host. *Phys. Rev. E* **63**, 041701 (2001).

[84] Russel, W. B.; Saville, D. A.; Schowalter, W. R. *Colloidal Dispersions* (Cambridge University Press, Cambridge, 1991).

[85] Hill, T. L. *An introduction to statistical thermodynamics* (Dover Publications, New York, 1986).

[86] Metropolis, N.; Rosenbluth, A. W.; Rosenbluth, M. N.; Teller, A. H.; Teller, E. Equation of State Calculations by Fast Computing Machines. *J. Chem. Phys.* **21**, 1087–1092 (1953).

[87] Osterman, N.; Babič, D.; Poberaj, I.; Dobnikar, J.; Ziherl, P. Observation of Condensed Phases of Quasiplanar Core-Softened Colloids. *Phys. Rev. Lett.* **99**, 248301 (2007).

[88] Hong, L.; Cacciuto, A.; Luijten, E.; Granick, S. Clusters of Amphiphilic Colloidal Spheres. *Langmuir* **24**, 621–625 (2008).

[89] Hansen, J. P.; McDonald, I. R. *Theory of simple liquids* (Academic Press, London, 2006).

[90] Le Roux, S.; Petkov, V. The radial distribution functions: definitions. *http://isaacs.sourceforge.net/phys/rdfs.html* (accessed November 2011).

[91] Lajovic, A.; Tomšič, M.; Jamnik, A. The complemented system approach: A novel method for calculating the x-ray scattering from computer simulations. *J. Chem. Phys.* **133**, 174123 (2010).

[92] Perko, S.; Dakskobler, A.; Kosmač, T. High-Performance Porous Nanostructured Ceramics. *J. Am. Ceram. Soc.* **93**, 2499–2502 (2010).

[93] Lange, F. F. Powder processing science and technology for increased reliability. *J. Am. Ceram. Soc.* **72**, 3–15 (1989).

[94] Diez Orrite, S.; Stoll, S.; Schurtenberger, P. Off-lattice Monte Carlo simulations of irreversible and reversible aggregation processes. *Soft Matter* **1**, 364–371 (2005).

[95] Lopéz-Lopéz, J. M.; Schmitt, A.; Moncho-Jordá, A.; Hidalgo-Álvarez, R. Stability of binary colloids: kinetic and structutal aspects of heteroaggregation processes. *Soft Matter* **2**, 1025–1042 (2006).

[96] Bianchi, E.; Tartaglia, P.; Zaccarelli, E.; Sciortino, F. Theoretical and numerical study of the phase diagram of patchy colloids: Ordered and disordered patch arrangements. *J. Chem. Phys.* **128**, 144504 (2008).

[97] Bergstrom, L. Hamaker constants of inorganic materials. *Adv. Colloid Interface Sci.* **70**, 125–169 (1997).

[98] Heermann, D. W. *Computer simulation methods in theoretical physics* (Springer, New York, 1990).

[99] Humphrey, W.; Dalke, A.; Schulten, K. VMD: Visual Molecular Dynamics. *J. Molec. Graphics* **14**, 33–38 (1996).

[100] PDF–ICDD, PCPDFWin Version 2.2. *International Center for Diffraction Data* (2002).

[101] Petricek, V.; Dusek, M.; Palatinus, M. Jana2006. The crystallographic computing system. *Institute of Physics, Praha, Czech Republic* (2006).

[102] Blunt, M. O.; Stannard, A.; Pauliac-Vaujour, E.; Martin, C. P.; Vancea, I.; Šuvakov, M.; Thiele, U.; Tadić, B.; Moriarty, P. Patterns and Pathways in Nanoparticle Self-Organization. In: Narlikar, A. V.; Fu, Y. Y. (ed.) *The Oxford Handbook of Nanoscience and Technology.* 214–249 (Oxford University Press, Oxford, 2010).

[103] Swartz, S. L.; Shrout, T. R.; Schultze, W. A.; Cross, L. E. Dielectric Properties of Lead-Magnesium Niobate Ceramics. *J. Am. Ceram. Soc.* **67**, 311–314 (1984).

[104] Wang, C.-H.; Schultze, W. A. The Role of Excess Magnesium Oxide or Lead Oxide in Determining the Microstructure and Properties of Lead Magnesium Niobate. *J. Am. Ceram. Soc.* **73**, 825–832 (1990).

[105] Koyuncu, M.; Pilgrim, S. M. Effects of MgO Stoichiometry on the Dielectric and Mechanical Response of $Pb(Mg_{1/3}Nb_{2/3})O_3$. *J. Am. Ceram. Soc.* **82**, 3075–3079 (1999).

[106] Mitoseriu, L.; Ianculescu, A.; Carnasciali, M.; Brileanu, A.; Curecheriu, L. Properties of the $Pb(Mg_{1/3}Nb_{2/3})O_3$ Ceramics Prepared by Using Two Different Mg Precursors. *Ferroelectrics* **369**, 157–169 (2008).

[107] Ananta, S.; Thomas, N. W. Fabrication of PMN and PFN ceramics by a two-stage sintering technique. *J. Eur. Ceram. Soc.* **19**, 2917–2930 (1999).

[108] Uršič, H.; Škarabot, M.; Hrovat, M.; Holc, J.; Skalar, M.; Bobnar, V.; Kosec, M.; Muševič, I. The electrostrictive effect in ferroelectric $65Pb(Mg_{1/3}Nb_{2/3})O_3$–$35PbTiO_3$ thick films. *J. Appl. Phys.* **103**, 124101 (2008).

[109] Kosec, M.; Holc, J.; Kuščer, D.; Drnovšek, S. $Pb(Mg_{1/3}Nb_{2/3})O_3$–$PbTiO_3$ thick films from mechanochemically synthesized powder. *J. Eur. Ceram. Soc.* **27**, 3775–3778 (2007).

[110] Gentil, S.; Damjanovic, D.; Setter, N. $Pb(Mg_{1/3}Nb_{2/3})O_3$ ans $(1-x)Pb(Mg_{1/3}Nb_{2/3})O_3$–$xPbTiO_3$ Relaxor Ferroelectric Thick Films: Processing and Electrical Characterization. *J. Electroceram.* **12**, 151–161 (2004).

[111] Bišćan, J.; Kosec, M.; Kallay, N. The isoelectric conditions of the constituents of the complex oxide $Pb(Zr,Ti)O_3$. *Colloids Surf., A* **79**, 217–226 (1993).

[112] Cotton, A.; Wilkinson, G. *Advanced Inorganic Chemistry* (John Wiley & Sons, New York, 1972).

[113] Škvarla, J.; Kmet, S. Non-equilibrium electrokinetic properties of magnesite and dolomite determined by the laser-Doppler electrophoretic light scattering (ELS) technique. A solids concentration effect. *Colloids Surf., A* **111**, 153–157 (1996).

[114] Senna, M.; Kuno, H. Polymorphic Transformation of PbO by Isothermal Wet Ball-Milling. *J. Am. Ceram. Soc.* **54**, 259–262 (1971).

[115] Ziemniak, S. E.; Palmer, D. A.; Benezeth, P.; Anovitz, L. M. Solubility of litharge (α – PbO) in alkaline media at elevated temperatures. *J. Sol. Chem.* **34**, 1407–1428 (2005).

[116] Lide, D. R. (ed.) *CRC Handbook of Chemistry and Physics* (CRC Press, Boca Raton, 2005).

[117] White, W.; Dachille, F.; Roy, R. High-Pressure-High-Temperature Polymorphism of the Oxides of Lead. *J. Am. Ceram. Soc.* **44**, 170–174 (1961).

[118] Haines, J.; Léger, J. M.; Schulte, O. $Pa\bar{3}$ modified fluorite–type structures in metal dioxides at high pressure. *Science* **271**, 626–631 (1996).

[119] Lu, C.-H.; Chang, D.-P. Reaction sintering and characterization of lead magnesium niobate relaxor ferroelectric ceramics. *J. Mater. Sci.: Mater. Electron.* **11**, 363–367 (2000).

[120] Sundar, V.; Newnham, R. E. Electrostriction. In: Dorf, R. C. (ed.) *The Electrical Engineering Handbook*. 1193–1200 (CRC Press, Boca Raton, 1997).

[121] Bouquin, O.; Lejeune, M.; Boilot, J. Formation of the Perovskite Phase in the $Pb(Mg_{1/3}Nb_{2/3})O_3$–$PbTiO_3$ System. *J. Am. Ceram. Soc.* **74**, 1152–1156 (1991).

Index of Figures

Index of Tables

Index of Algorithms

List of Publications

Publications from the Dissertation

Scientific Articles

1. Trefalt, G.; Malič, B.; Kuščer, D.; Holc, J.; Kosec, M. Synthesis of $Pb(Mg_{1/3}Nb_{2/3})O_3$ by Self-Assembled Colloidal Aggregates. *J. Am. Ceram. Soc.* **94**, 2846–2856 (2011).

2. Trefalt, G.; Tadic, B.; Kosec, M. Formation of colloidal assemblies in suspensions for $Pb(Mg_{1/3}Nb_{2/3})O_3$ synthesis: Monte Carlo simulation study. *Soft Matter* **7**, 5566–5577 (2011).

3. Trefalt, G.; Malič, B.; Holc, J.; Kosec, M. Synthesis of $Pb(Mg_{1/3}Nb_{2/3})O_3$–$PbTiO_3$ by Controlled Agglomeration of Precursor Particles. *J. Am. Ceram. Soc.* **accepted**, X (201X)

Conference Proceedings

1. Tadić, B.; Šuvakov, M.; Trefalt, G. Modelling structure of collodal assemblies : Methodology & examples. In: *Proceedings of the 2011 International Conference on Computational and Mathematical Methods in Science and Engineering.* 1097–1103 (CMMSE, Benidorm, 2011).

2. Trefalt, G.; Malič, B.; Tadić, B.; Holc, J.; Kuščer, D.; Kosec, M. Innovative approach to synthesis of $Pb(Mg_{1/3}Nb_{2/3})O_3$ based materials using colloidal interactions. In: *3rd Jožef Stefan International Postgraduate School Students Conference.* 206–211 (Jožef Stefan International Postgraduate School, Ljubljana, 2011).

Other Publications

Scientific Articles

1. Trefalt, G.; Hribar-Lee, B. Adsorption of electrolyte mixtures in disordered porous media. A Monte Carlo study. *Acta Chim. Slov.* **54**, 503–508 (2007).

2. Lukšič, M.; Trefalt, G.; Hribar-Lee, B. Application of Replica Ornstein-Zernike equations in studies of the adsorption of electrolyte mixtures in disordered matrices of charged particles. *Condens. Matter Phys.* **12**, 717–724 (2009).

3. Tellier, J.; Malič, B.; Kuščer, D.; Trefalt, G.; Kosec, M. Ink-jet printing of In_2O_3/ZnO two-dimensional structures from solution. *J. Am. Ceram. Soc.* **94**, 2834–2840 (2011).

4. Kuščer, D.; Stavber, G.; Trefalt, G.; Kosec, M. Formulation of an Aqueous Titania Suspension and its Patterning with Ink-Jet Printing Technology. *J. Am. Ceram. Soc.* **in press**, doi: 10.1111/j.1551–2916.2011.04876.x (2011).

Conference Proceedings

1. Trefalt, G.; Kosec, M.; Kuščer, D.; Stavber, G.; Malič, B. Ink-jet printing of TiO_2 suspensions. In: *Proceedings, 2011 IMAPS/ACerS, 7th International Conference and Exhibition on Ceramic Interconnect and Ceramic Microsystems Technologies (CICMT)*. 47–53 (International Microelectronics and Packaging Society, San Diego, 2011).

Popular Article

1. Uršič, H.; Trefalt, G.; Glinšek, S. Obisk podiplomskih študentov z ameriške univerze Brown, Rhode Island. *Novice - IJS* **18**, 30–34 (2009).

Conferences and Workshops

Talks

1. Trefalt, G.; Degen, A.; Malič, B.; Kuščer, D.; Holc, J.; Kosec, M. *Nova metoda priprave keramike na osnovi $Pb(Mg_{1/3}Nb_{2/3})O_3$*. Slovenian Chemical Days, Maribor (2008).

2. Trefalt, G.; Hribar-Lee, B.; Kosec, M. *Adsorption of electrolyte mixtures in disordered porous media.* NanoMetro Workshop, Leysin (2008).

3. Kosec, M.; Malič, B.; Degen, A.; Trefalt, G. *Single step synthesis of $Pb(Mg_{1/3}Nb_{2/3})O_3$ from an aqueous suspension.* Electroceramics XI, Manchester (2008).

4. Trefalt, G.; Kosec, M.; Malič, B.; Kuščer, D. *Modeling of distribution of colloidal particles in suspensions.* 17^{th} Conference on Materials and Technology, Portorož (2009).

5. Lukšič, M.; Trefalt, G.; Hribar-Lee, B. *Adsorption of model electrolytes in disordered porous materials. Predictions of the replica integral equation theory.* 3^{rd} Conference Statistical Physics: Modern Trends and Applications, Lviv (2009).

6. Trefalt, G.; Tadić, B.; Kosec, M. *Študij aglomeracije delcev v suspenziji za sintezo $Pb(Mg_{1/3}Nb_{2/3})O_3$ simulacijami Monte Carlo.* Yung Researchers Day @ JSI, Ljubljana (2010).

7. Trefalt, G.; Tadić, B.; Kosec, M. *Monte Carlo simulation of aggregation of reagent particles in the suspensions for $Pb(Mg_{1/3}Nb_{2/3})O_3$.* Electroceramics XII, Trondheim (2010).

8. Trefalt, G.; Kuščer, D.; Stavber, G.; Kosec, M. *Ink-jet printing of TiO_2 suspensions.* 18^{th} Conference on Materials and Technology, Portorož (2010).

9. Kuščer, D.; Stavber, G.; Trefalt, G.; Kosec, M. *Vodne suspenzije keramičnih materialov primerne za oblikovanje struktur z brizgalnim tiskanjem.* Slovenian Chemical Days, Maribor (2010).

10. Trefalt, G.; Kuščer, D.; Stavber, G.; Kosec, M. *Ink-jet printing of aqueous suspensions containing TiO_2 nanoparticles.* SLONANO, Ljubljana (2010).

11. Trefalt, G.; Malič, B.; Holc, J.; Kosec, M. *$Pb(Mg_{1/3}Nb_{2/3})O_3$–$PbTiO_3$ ceramic prepared from aqueous suspensions.* ESR Meetig of the COST MP0904 action, Hasselt (2011).

12. Trefalt, G.; Kosec, M.; Kuščer, D.; Stavber, G.; Malič, B. *Ink-jet printing of TiO_2 suspensions.* 7^{th} International Conference and Exhibition on Ceramic Interconnect and Ceramic Microsystems Technologies (CICMT), San Diego (2011).

13. Holc, J.; Belavič, D.; Hrovat, M.; Uršič, H.; Trefalt, G.; Drnovšek, S.; Kosec, M. *An investigation of different piezoelectric thick films for application on low temperature co-fired ceramics.* 12^{th} Conference of the European Ceramic Society, Stockholm (2011).

14. Kosec, M.; Rojac, T.; Malič, B.; Trefalt, G.; Glinšek, S. *Towards extreme properties of functional ceramics by novel powder processing routes.* Invited talk. 12^{th} Conference of the European Ceramic Society, Stockholm (2011).

15. Kosec, M.; Malič, B.; Kuščer, D.; Trefalt, G.; Tellier, J. *How ceramic processing can contribute to progress in transparent electronics.* Invited talk. E-MRS Fall Meeting, Warsaw (2011).

16. Koruza, J.; Malič, B.; Trefalt, G.; Kosec, M. *Microstructure evolution during two-stage sintering of sodium niobate.* International Conference on Sintering 2011, Jeju (2011).

17. Koruza, J.; Malič, B.; Trefalt, G.; Kosec, M. *Microstructure development upon two-stage sintering of nano-sodium niobate.* 19^{th} Conference on Materials and Technology, Portorož (2011).

Posters

1. Trefalt, G.; Degen, A.; Malič, B.; Holc, J.; Kuščer, D.; Kosec, M. *Priprava keramike $Pb(Mg_{1/3}Nb_{2/3})O_3$ iz vodne suspenzije.* Yung Researchers Day @ JSI, Ljubljana (2008).

2. Trefalt, G.; Degen, A.; Malič, B.; Holc, J.; Kuščer, D.; Kosec, M. *Synthesis of $Pb(Mg_{1/3}Nb_{2/3})O_3$ in Alkaline Medium.* Hot nano topics, Portorož (2008).

3. Trefalt, G.; Degen, A.; Malič, B.; Kuščer, D.; Holc, J.; Kosec, M. *Synthesis of $Pb(Mg_{1/3}Nb_{2/3})O_3$ via aqueous suspension route.* European Colloid and Interface Society Conference, Kraków (2008).

4. Trefalt, G.; Hribar-Lee, B. *Distribution of Ions in Disordered Porous Media.* Workshop Networks, Complexity & Competition, Bled (2008).

5. Trefalt, G.; Hribar-Lee, B.; Kosec, M. *Preferential adsorption of ions in disordered porous medium.* Nanostructured materials and membrane modelling and simulation, Patras (2008).

6. Trefalt, G.; Kosec, M.; Malič, B.; Kuščer, D. *$Pb(Mg_{1/3}Nb_{2/3})O_3$ powders and ceramics prepared by a single-step synthesi route from aqueous suspensions.* IMF-ISAF-2009, Xi'an (2009).

7. Trefalt, G.; Kosec, M.; Malič, B.; Kuščer, D. *Simulations of aggregation of colloidal particles in the suspensins for $Pb(Mg_{1/3}Nb_{2/3})O_3$ synthesis.* SLONANO, Ljubljana (2009).

8. Trefalt, G. *Tiskanje funkcionalnih materialov z brizgalnim (ink-jet) tiskalnikom.* 1st Jožef Stefan International Postgraduate School Students Conference, Ljubljana (2009).

9. Trefalt, G.; Tadić, B.; Kosec, M. *Formation of clusters in the suspension containing three types of charged colloidal particles studied by Monte Carlo simulations.* European Colloid and Interface Society Conference, Prague (2010).

10. Trefalt, G.; Kosec, M.; Malič, B.; Kuščer, D. *Properties of $Pb(Mg_{1/3}Nb_{2/3})O_3$ powders and ceramics prepared suspensions stnthesis route.* Workshop on structural characterisation, Ljubljana (2010).

11. Kosec, M.; Trefalt, G.; Malič, B.; Holc, J. *Single step synthesis of $Pb(Mg_{1/3}Nb_{2/3})O_3$ from an aqueous suspension.* MRS Fall Meeting, Boston (2010).

12. Trefalt, G.; Malič, B.; Holc, J.; Kosec, M. *Enostopenjska sinteza $0.65Pb(Mg_{1/3}Nb_{2/3})O_3$–$0.35PbTiO_3$ iz vodnih suspenzij.* Yung Researchers Day @ JSI, Ljubljana (2011).

13. Trefalt, G.; Malič, B.; Holc, J.; Kosec, M. *Single-step synthesis of $0.65Pb(Mg_{1/3}Nb_{2/3})O_3$–$0.35PbTiO_3$.* Piezo: Electroceramics for end-users, Sestriere (2011).

14. Tellier, J.; Malič, B.; Kuščer, D.; Trefalt, G.; Kosec, M. *Patterning of In_2O_3-ZnO 2D structures using ink-jet technology.* Slovenian-Italian Conference on Materials and Technologies for Sustainable Growth, Ajdovščina (2011).

15. Trefalt, G.; Malič, B.; Tadić, B.; Holc, J.; Kuščer, D.; Kosec, M. *Innovative approach to synthesis of $Pb(Mg_{1/3}Nb_{2/3})O_3$ based materials using colloidal interactions.* 3rd Jožef Stefan International Postgraduate School Students Conference, Ljubljana (2011).

16. Trefalt, G.; Malič, B.; Holc, J.; Kosec, M. *Solid-state synthesis of functional oxide materials by designing contacts between reagent particles.* 12th Conference of the European Ceramic Society, Stockholm (2011).

17. Trefalt, G.; Kuščer, D.; Stavber, G.; Kosec, M. *Designing aqueous TiO_2 suspensions for the use in ink-jet printing technology.* European Colloid and Interface Society Conference, Berlin (2011).